PATTERN GENERATION OF STRAIN RATE SIMULATION FOR CROSS-WELL HYDRAULIC FRACTURE MONITORING IN UNCONVENTIONAL RESERVOIRS

A Dissertation

by

JIN TANG

Submitted to the Graduate and Professional School of
Texas A&M University
in partial fulfillment of the requirements for the degree of

DOCTOR OF PHILOSOPHY

Chair of Committee,	Ding Zhu
Committee Members,	A. Daniel Hill
	Jihoon Kim
	Luis San Andrés
Head of Department,	Jeff Spath

August 2021

Major Subject: Petroleum Engineering

ABSTRACT

In multistage hydraulic fracturing treatments, the combination of extreme large-scale pumping (high rate and volume) and the high heterogeneity of the formation (because of large contact area) normally results in complex fracture growth that cannot be simply modeled with conventional fracture models. Lack of understanding of the fracturing mechanism makes it difficult to design and optimize hydraulic fracturing treatments. Many monitoring, testing and diagnosis technologies have been applied in the field to describe hydraulic fracture development. Strain rate measured by distributed acoustic sensors (DAS) is one of the tools for fracture monitoring in complex completion scenarios. DAS measures far-field strain rate that can be of assistance for fracture characterization, cross-well fracture interference identification, and well stimulation efficiency evaluation. Many field cases have shown DAS responses on observation wells or surrounding producers when a well in the vicinity is fractured. Modeling and interpreting DAS strain rate responses can help quantitatively map fracture propagation. In this dissertation, a methodology is developed to generate the simulated strain rate patterns based on existing fractures. The patterns are then used to build a database for interpretation purpose.

Instead of using a complex fracture model to forward simulate fracture propagation, this work starts from a simple fracture propagation model to provide hypothetical fracture geometries in a relatively reasonable and acceptable range for both single fracture case and multiple fracture case. Displacement discontinuity method (DDM) is formulated to simulate rock deformation and fiber-optic measurement. At each time step, fracture propagation is first allowed, then stress, displacement and strain field are characterized as the fracture approaches to the observation well. Afterward, the strain rate is calculated as fracture growth to generate patterns of fracture approaching. Extended simulation is conducted to build the database for fracture propagation behavior. These patterns can be used to recognize fracture development.

Examples of strain rate responses in the pattern database for both single fracture and multiple fracture scenarios are presented in this dissertation to show the potential of using DAS measurements to diagnose multistage hydraulic fracturing treatments.

DEDICATION

To my beloved parents,

Yan Chai & Tingchuan Tang

ACKNOWLEDGEMENTS

I want to express my sincere gratitude to my committee chair and advisor Dr. Ding Zhu for her tremendous guidance, encouragement, and support throughout my study. Also, I would like to give Dr. A. Daniel Hill deep thanks for his valuable advice and insight into my research. I have learned a lot from them, not only the knowledge but also the wisdom and positive attitude towards life. In particular, the power of persistence that they show me in their work every day.

I want to thank Dr. Jihoon Kim and Dr. Luis San Andrés for their valuable discussion and suggestion for this work.

Thanks also go to my friends and colleagues for making my time in Aggieland a fantastic and unforgettable journey.

Special thanks to my dear colleague Smith Leggett and our brilliant visiting scholar Dr. Ming Chen. Without the help and inspiration from these two great gentlemen, I would not complete this work.

Finally, I would like to thank my parents for their continuous support and encouragement. It is their endless love to make me a better man every day.

CONTRIBUTORS AND FUNDING SOURCES

Contributors

This work was supervised by a Ph.D. dissertation committee consisting of Professor Ding Zhu [advisor], Professor A. Daniel Hill and Professor Jihoon Kim of the Harold Vance Department of Petroleum Engineering, and Professor Luis San Andrés of the J. Mike Walker '66 Department of Mechanical Engineering. All work for the dissertation was completed independently by the student.

Funding Sources

This work was made possible by the financial support of the Marathon Oil Corporation and the Harold Vance Department of Petroleum Engineering at Texas A&M University.

TABLE OF CONTENTS

Page

LIST OF FIGURES

Page

LIST OF TABLES

Page

1 INTRODUCTION

1.1 Background

Unconventional hydrocarbon resources are widespread throughout the United States, as shown in Fig. 1.1. Unconventional reservoirs restrain hydrocarbons that were formed within an ultra-tight source rock and never migrated. Unconventional reservoirs include reservoirs such as oil and gas shales, coalbed methane, gas hydrates, tar sands, and tight-gas sands. Compared with conventional reservoirs, these reservoirs require extraction solutions such as extensive stimulation treatments or exceptional recovery processes and techniques to be produced at economic flow rates and that produce economic volumes of hydrocarbons.

Unconventional oil and gas reservoirs play an essential role in providing energy to the society. With continuously witnessing the rapid decline in conventional oil and gas resources worldwide, the exploration and development of unconventional resources have become the priority to cover the shortage of energy demand. Despite growing attention to alternative energy sources in recent years, the world cannot ignore the compelling importance of oil and gas in ensuring energy security and turn out an affordable solution to the massive increasing energy demand in the future. Unconventional oil and gas reservoirs contain the future of the energy supply.

Nowadays, the oil and gas industry is facing significant challenges. Finding more economical and effective development methods has become one of the most concerning issues of the industry.

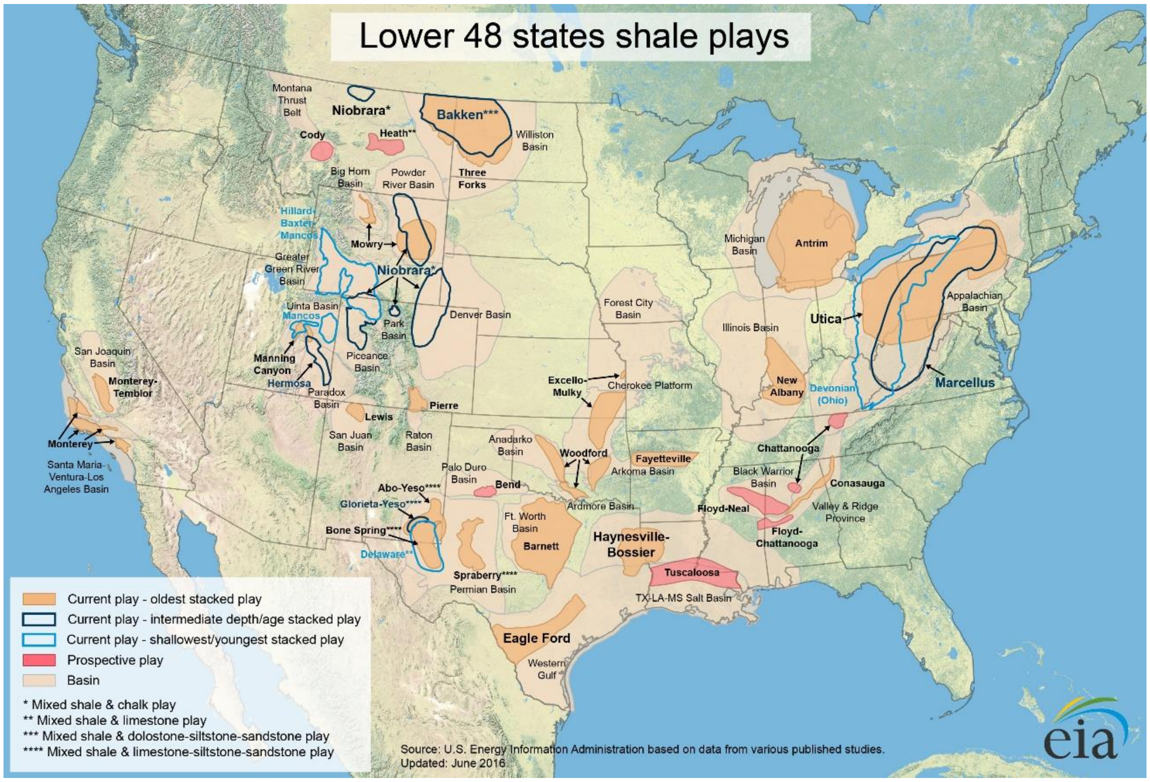

Source: U.S. Energy Information Administration based on data from various published studies.
Updated: June 2016

Fig. 1.1 Shale gas and oil plays, Lower 48 States (Reprinted from (EIA))

Multistage hydraulic fracturing of horizontal wells is a critical stimulation method to extract oil and gas from unconventional plays (Cipolla et al., 2009; Daneshy, 2011). Nowadays, to increase the contact area with reservoirs and enhance production, the hydraulic stimulation treatment is moving towards tightly spaced horizontal wells with small cluster spacing to create more complex fracture network (Marongiu-Porcu et al., 2015; Safari et al., 2017). Meanwhile, more infill wells are drilled between parent wells to further maximize production in many cases. All these stimulation strategies create more complex fracture networks in the shale reservoir, limiting our knowledge of hydraulic fracture geometry for conventional reservoir to be applied, and raising the difficulty of optimization of stimulation.

Therefore, there is a critical need to develop novel techniques that can better understand hydraulic fracturing stimulation. Recently, low-frequency DAS (Distributed Acoustic Sensing) is one of the techniques for fracture monitoring in complex fracture conditions (Jin and Roy, 2017; Ugueto et al., 2019; Li et al., 2020). Modeling DAS far-field strain rate responses can help quantitatively map fracture development. The overall objective of this study is to better understand hydraulic fracture geometry and cross-well communication.

1.2 Literature Review

1.2.1 Hydraulic Fracture Monitoring Techniques

Diagnosis of fracture has been a challenge for the industry for a long time. Since 1949, the first commercial hydraulic fracturing took place in Oklahoma, the industry has never stopped trying to better understand fractures and improve completion efficiency.

Hydraulic fracture monitoring techniques have been applied to investigate and diagnose the hydraulic stimulation, especially help us to determine important properties of fracture such as fracture width, fracture length, fracture height, and fracture conductivity. Hydraulic fracture monitoring techniques are divided into direct far-field techniques, direct near-wellbore techniques, and indirect fracture techniques (Cipolla and Wright, 2000).

Direct far-field techniques include tiltmeters, microseismic monitoring, and distributed acoustic sensing (DAS). These techniques are usually deployed in an offset well or on the surface. When a hydraulic fracture is created, the fracture propagation causes the rock deformation around the fracture. The associated deformation response can be detected from far-field. The largest limitation of these techniques is that although they can map the total fracture growth, they cannot provide the detail about the fracture geometry.

Tiltmeters, as shown in Fig. 1.2 (Cipolla and Wright, 2000), can be used to measure rock deformation and investigate fracture growth.

Surface tiltmeters are placed in shallow holes close to the surface (Wright et al., 1998; Wolhart et al., 2007). The surface tiltmeters measure fracture-induced tilts above the hydraulic fracture at the surface and then solve the geophysical inverse problem to determine the fracture parameters. The surface tiltmeters can measure fracture azimuth and dip. However, because of surface tiltmeters are usually very far away from the fracture location, they cannot estimate fracture geometry.

Downhole tiltmeters are placed in the offset wells near the hydraulic stimulation treatment zone (Warpinski et al., 1997; Wright et al., 1999). Because of the measurements of downhole tiltmeters are conducted near the fracture treatment, the downhole tiltmeter data are more sensitive to the stimulation and can be more accurately analyzed to determine the orientation and dimensions of the created fracture.

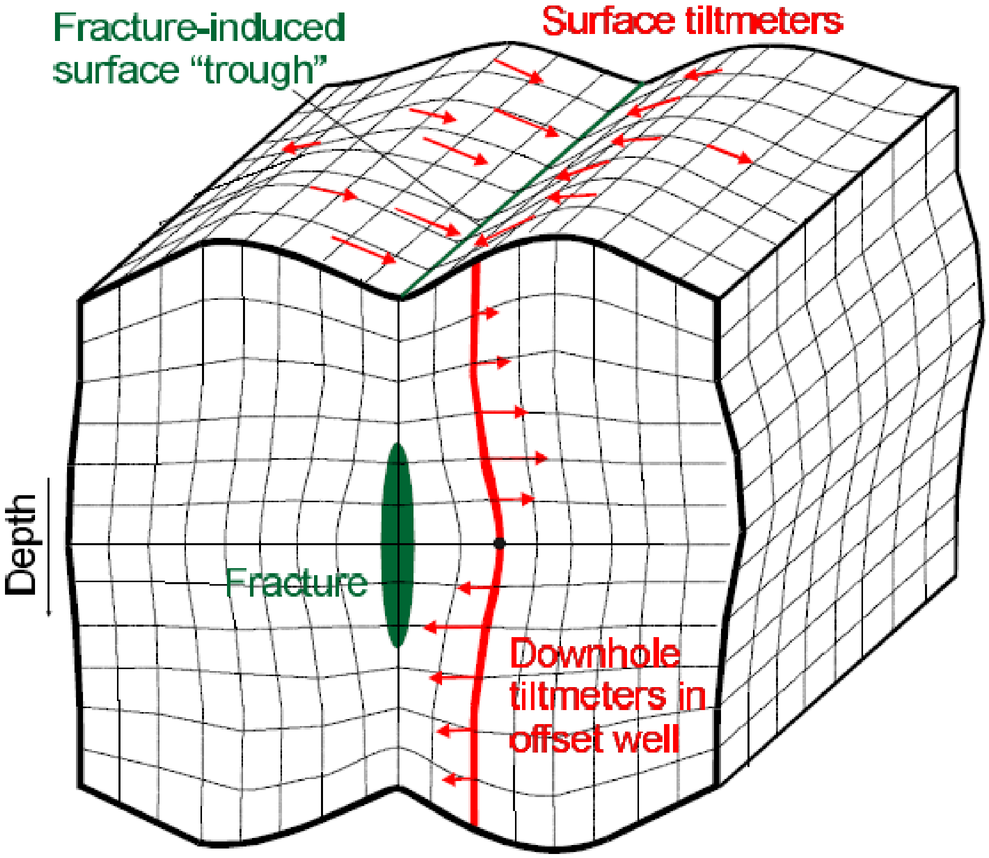

Fig. 1.2 Schematic of surface tiltmeters and downhole tiltmeters (Reprinted from (Cipolla and Wright, 2000))

Microseismic monitoring relies on downhole or/and surface receivers of accelerometers or geophones to locate microseisms/microearthquakes that are caused by fracture treatments (Cipolla et al., 2000; Fisher et al., 2004). Fig. 1.3 illustrates the principle of the microseismic monitoring.

Once hydraulic stimulation starts, the injection fluid squeezes the rock and causes shear slippage on bedding planes of the rock, resulting in microseismic events. These microseismic events will be recorded by geophone over time. The data are then processed with a surface data acquisition apparatus. The microseismic events are located and analyzed to provide information on fracture growth and geometry.

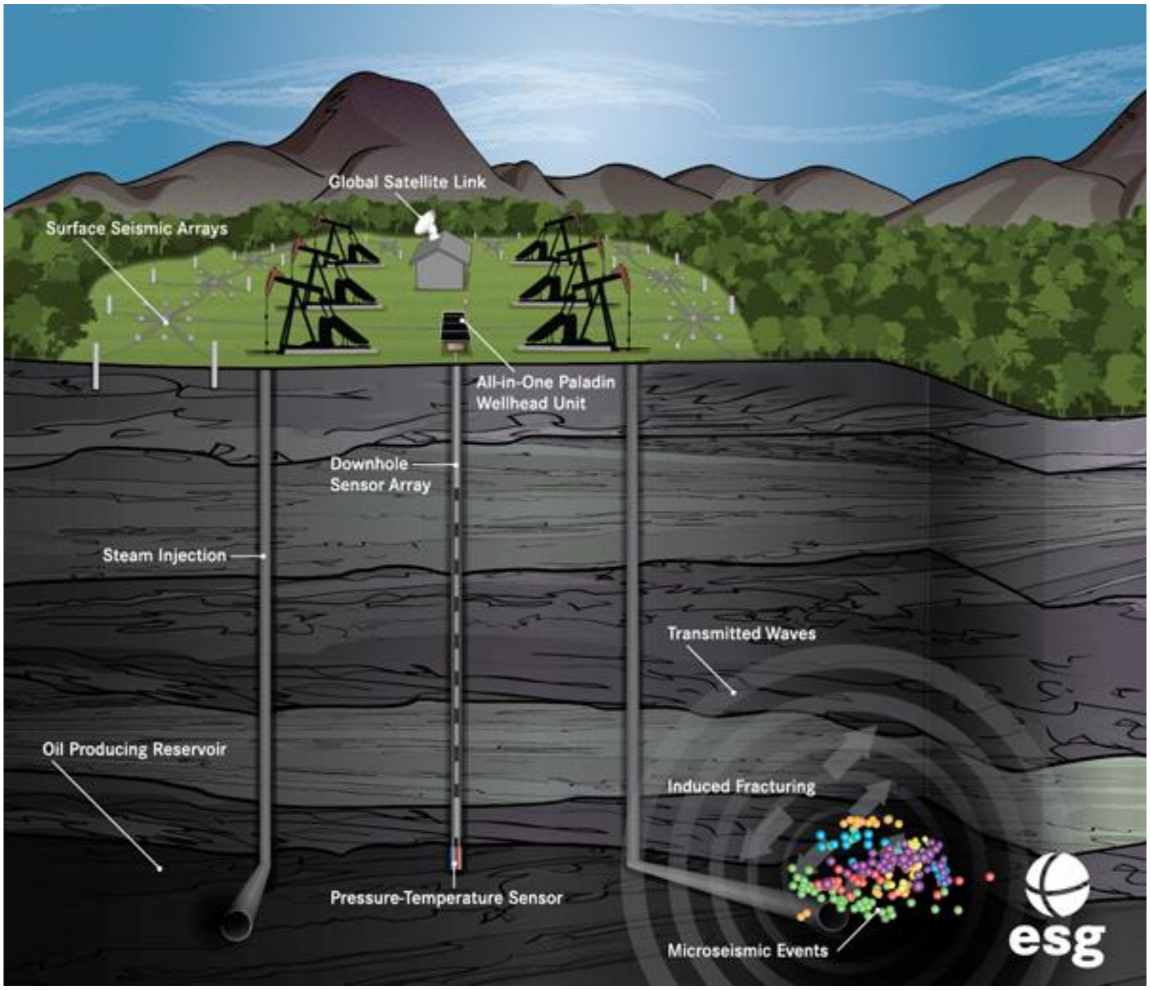

Fig. 1.3 Schematic of microseismic monitoring (Reprinted from (ESG Solutions))

Direct near-wellbore techniques include tracer (Woodroof et al., 2003), temperature logging (Hill, 1990), borehole image logging (Cheung and Heliot, 1990), downhole video (Roberts et al., 2018; Cramer et al., 2019), and others. These techniques are generally implemented inside/through the treated wellbore after the fracture treatment.

Physical properties such as temperature or radioactivity in the near-wellbore region are logged with the appropriate tools.

All those techniques can help in different ways to better map fracture growth, fracture geometry and provide substantial information for optimizing hydraulic fracturing design, improving well stimulation efficiency, as well as enhancing well production performance.

These direct near-wellbore techniques can investigate the fractures that are directly connected to the wellbore. However, they are not able to evaluate the fractures that are not connected with the wellbore.

Indirect fracture techniques including fracture modeling, well testing, production data analysis, and others. Those techniques are widely used to study the fracture treatments and determine the hydraulic fracture geometry, because the data required for the analyses are available on every well.

The main limitation of these indirect techniques is that solutions are generally non-unique because of the large number of unknowns involved and the assumptions made when conducting the analysis. Therefore, it is necessary to calibrate indirect techniques with direct observations.

1.2.2 Fiber-Optic Sensing Technology

Distributed fiber-optic sensors have been existed as a powerful fiber-optic based monitoring tool in many industries, such as pipeline monitoring, power monitoring, railway monitoring, and oilfield services, for a long time. However, due to its high cost, it has not been widely applied. With the vigorous development of electronic and information industry in recent years, the cost of fiber-optic technology has dropped significantly. This makes it possible to apply the fiber-based monitoring technology on a large scale in oilfield services.

Distributed acoustic sensing (DAS) is a revolutionary photonic sensing technology that enables continuous detection of acoustic and vibration variations along with the sensing fiber over long distances in real-time. The fundamental of DAS is using optical fiber to measure phase shifts as response of axial strain and strain rate changes, and the fiber can be used as a distributed interferometer composed of countless small reflectors. A coherent laser pulse is sent downhole along the fiber, then for each reflective site, there is a backscattered signal sending back to the surface, as shown in Fig. 1.4. DAS measurements are gated into channels, and the measured data will be stored in an interrogator unit. DAS signals are a series of phase shifts corresponding to different channels over time, which are correlated with the strain rate.

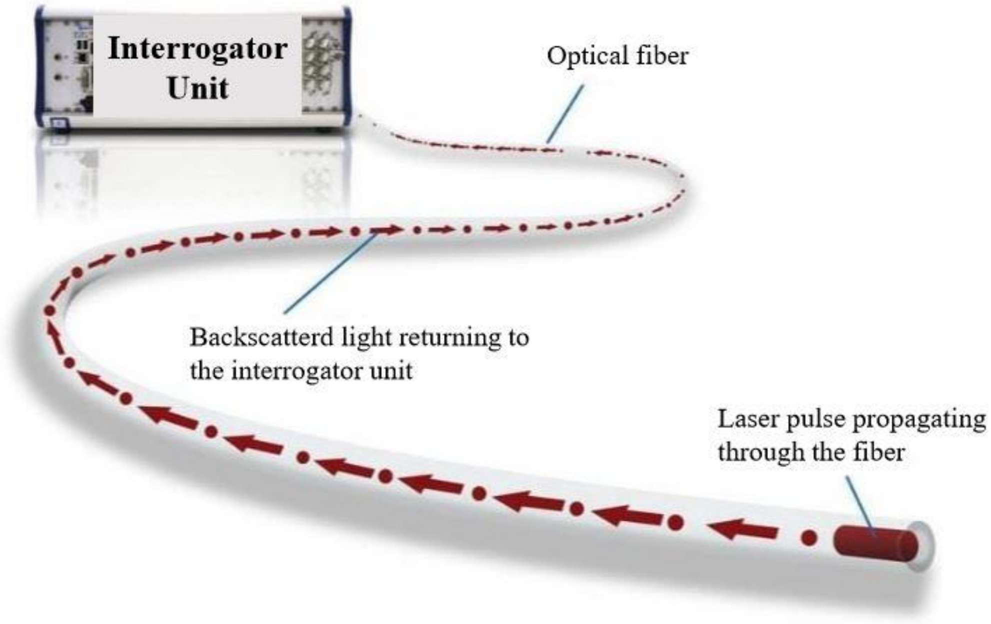

Fig. 1.4 Schematic of a working distributed fiber-optic sensor (Modified from (Johannessen et al., 2012))

The backscattered signal consists of three components: Rayleigh backscattering, Raman backscattering, and Brillouin backscattering. Fig. 1.5 illustrates the frequency features of these three components on the scattered light spectra. The Stokes and anti-Stokes components are also marked in the figure.

The Rayleigh backscattering is an elastic scattering, a form of particle scattering that in this process, the kinetic energy of a particle is conserved in the center-of-mass frame, but its direction of propagation is modified, which is sensitive to acoustic. The Brillouin backscattering is an order of magnitude less in intensity, which is sensitive to strain variations. The Raman backscattering is three to five orders of magnitude smaller in intensity than the Brillouin backscattering, which is sensitive to temperature variations (Krohn et al., 2015).

Rayleigh backscatter events are used to create distributed acoustic sensing (DAS) measurements. Brillouin and Raman scattering are used for seismic and temperature measurements, respectively (Santos, 2018).

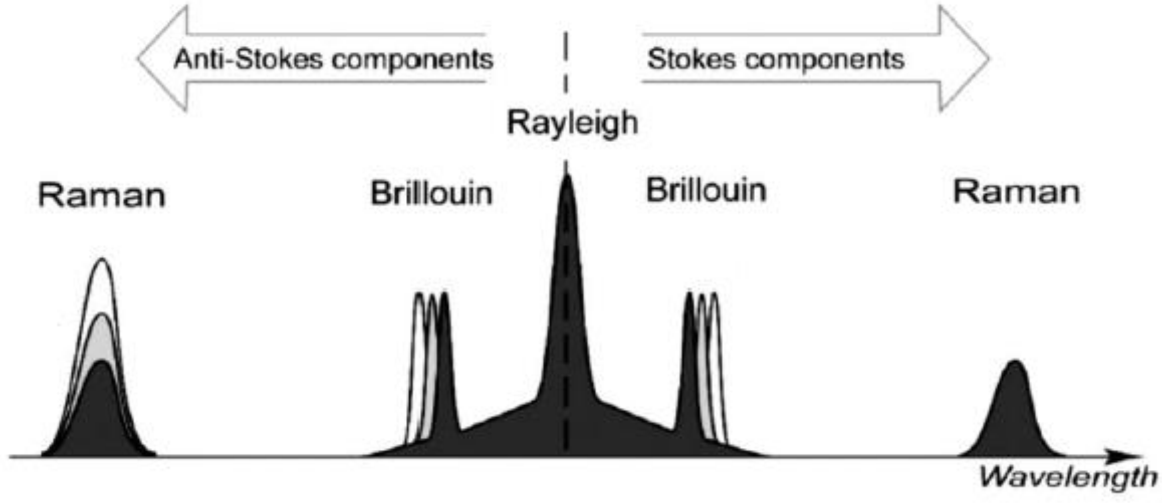

Fig. 1.5 Backscatter components used in fiber-optic sensing (Modified from (Frings and Walk, 2010))

As shown in Fig. 1.6, the installation of distributed fiber-optic sensors can be inside tubing, outside tubing, and outside casing.

Permanent installation outside casing of DAS can provide high-quality data during downhole monitoring, and it is also the best option for life-of-the-well monitoring. With decent cementing, the fiber can be considered as mechanically coupled with the formation rock. Therefore, the strain rate variations of formation due to hydraulic fracturing can be measured by the optical fiber.

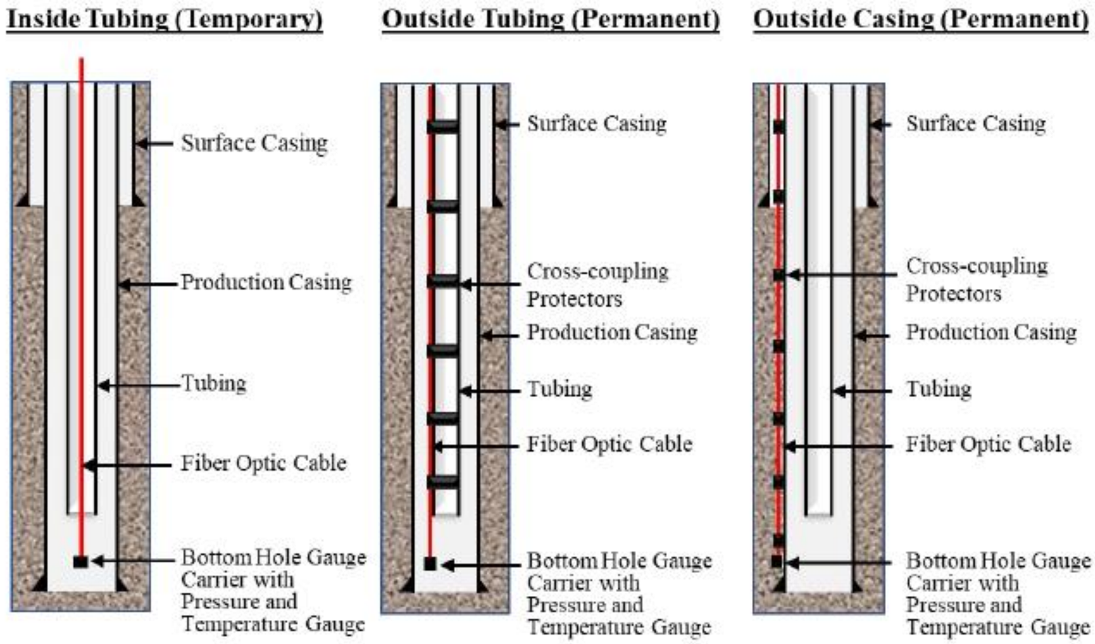

Fig. 1.6 Deployment methods of distributed fiber-optic sensors (Reprinted from (Zhang, 2019))

1.2.3 Hydraulic Fracture Propagation Models

Simulating fracture propagation is challenging, especially nowadays, fracture geometry is more complex because of the combination of extreme large-scale pumping and the heterogeneous formation encountered. However, those difficulties have not stopped the researchers from exploring hydraulic fracturing modeling. Shortly after fracturing technology was implemented, researchers started working on developing fracture propagation models.

Howard and Fast (1957) developed the first 2D fracture model to simulate fracture propagation. This model assumes a constant fracture width and is coupled with the leak-off by using Carter Equation II. It is the first fracture model that makes the fracture design possible.

Later, more 2D models were presented. The most well-known 2D fracture models are Kristonovich-Geertsma-deKlerk (KGD) (Khristianovitch and Zheltov, 1955; Geertsma and de Klerk, 1969) and Perkins-Kern-Nordgren (PKN) (Perkins and Kern, 1961; Nordgren, 1972). Both these two models assume plane strain deformation with fixed fracture height. The KGD model is usually being considered suitable for fracture propagation with the fracture height direction dominating the fracture growth, while the PKN model is usually being considered reasonable for the fracture propagation with the fracture length direction dominating the fracture growth. These two models are very well recognized and have shown useful for fracture modeling. The advantage of both is providing a concise analytical solution and high computational efficiency while maintaining the fracture calculation results in an acceptable and reasonable range.

As an extension of 2D models, pseudo-3D models (Simonson et al., 1978; Settari and Cleary, 1984; Fung et al., 1987) were developed to simulate fracture growth into multiple layers of the formation. Pseudo-3D models transform the 3D fracture problem to a 2D rock deformation problem and a 1D lateral fluid flow problem. Meanwhile, fully 3D models (Clifton and Abou-Sayed, 1981; Abou-Sayed et al., 1984; Weng, 1992; Dontsov and Peirce, 2015) were also developed to enhance the realism further. The general methodology of fully 3D models is based on the 3D rock deformation and 2D fluid flow in the fracture.

In conclusion, all these fracture models are developed under certain assumptions, which are far from the realities. This gives us a basic acknowledgment that hydraulic fracture models should not be put in the first place to determine the fracture propagation but as an assisted tool for us to better understand the fracture growth. The industry does not lack complex hydraulic fracturing propagation models. However, none of the models alone can truly and accurately simulate the complex subsurface fracture development. Thus, when choose fracture propagation models to provide some baseline and insight for the research on fracture monitoring, the strategy is to use simple models instead of complex fracture models. This ensures the efficiency of monitoring interpretation.

1.2.4 Low-Frequency DAS Application

The application of distributed acoustic sensing can be divided into two groups: high frequency and low frequency. DAS data in high-frequency band (200Hz-2000Hz) have been widely applied for wellbore and near-wellbore stimulation and production monitoring in the past few years. The applications include liquid holdup estimation for two-phase flow in pipe (Bukhamsin and Horne, 2014), fracture fluid distribution interpretation during fracturing (Pakhotina et al., 2020a), near-wellbore evaluation of perforation cluster efficiency (Ugueto C. et al., 2016), evaluation of perforation erosion (Pakhotina et al., 2020b) and others.

Recently, low-frequency DAS data (<1 Hz) have been getting attention for the information related to geo-mechanical event detection that provides crucial information for fracture characterization. Low-frequency DAS data were usually obtained in an offset well while a well in the vicinity is under hydraulic stimulation. Raw DAS data would usually be recorded at a high sampling rate. Later, those raw DAS data will be down-sampled at a low frequency and stored as raw low-frequency DAS data. Different data processing methods are performed on the raw low-frequency DAS data by different fiber vendors and researchers. The processed low-frequency DAS data contain geo-mechanical information and deliver evident strain-rate polarity as shown, for instance, in Fig. 1.7. (Jin and Roy, 2017)

Fig. 1.7 shows the low-frequency DAS data recorded in the monitoring well during hydraulic fracturing in an injection well nearby. Compressing and extending are used to describe the measured strain rate in this plot. Blue indicates fiber compressing, and red reveals fiber extending. The current stage area, with time-lapse, shows extended. Meanwhile, the areas on both sides of current stage, with time-lapse, show compressed. Several fracture hits can be identified along with the fiber, where the fiber is extended during pumping and compressed after pumps shut down. This figure shows abundant and concise geo-mechanical information about the interference between two adjacent wells during fracture treatments.

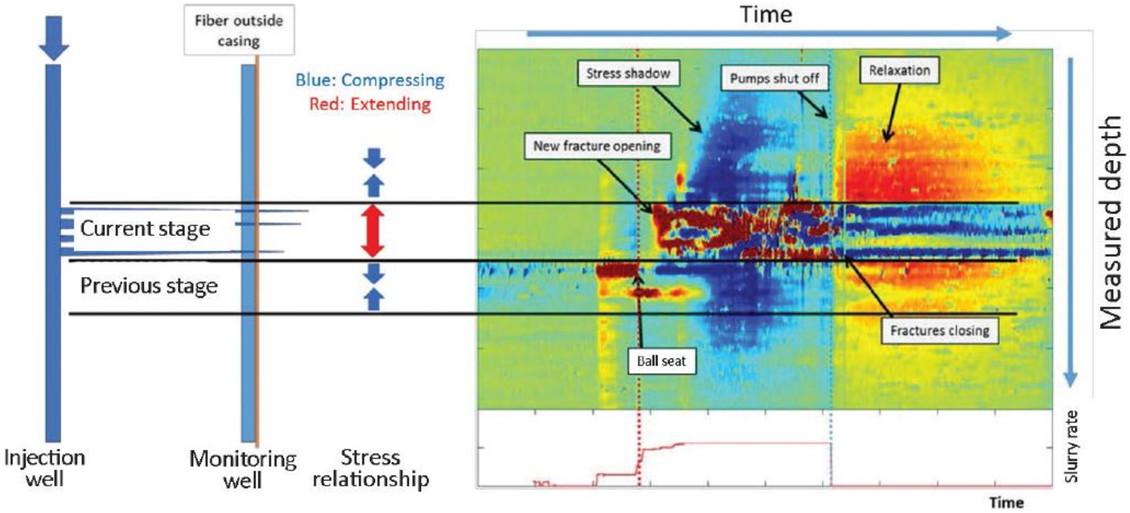

Fig. 1.7 Low-frequency DAS responses from a monitoring well during an adjacent well under hydraulic stimulation (Reprinted from (Jin and Roy, 2017))

More recently, Ugueto et al. (2019) presented a field study in the Groundbirch Montney in Canada, using low-frequency DAS data from an offset well to constrain the fracture geometry and better understand the fracture growth during the operation well is under hydraulic stimulation. A hypothetical evolution with four progressive stages of low-frequency DAS responses during the entire fracture treatments has been concluded, as shown in Fig. 1.8, showing the low-frequency DAS responses change with fracture propagation. Four stages include (1) broad extending low-frequency DAS responses to approaching hydraulic fracs; (2) narrowing extending low-frequency DAS responses to near approaching hydraulic fracs; (3) rapidly extending and compressing zone of low-frequency DAS responses to intercepting hydraulic fracs; (4) extending and compressing reversal zone of low-frequency DAS responses to shortly after stimulation hydraulic fracs.

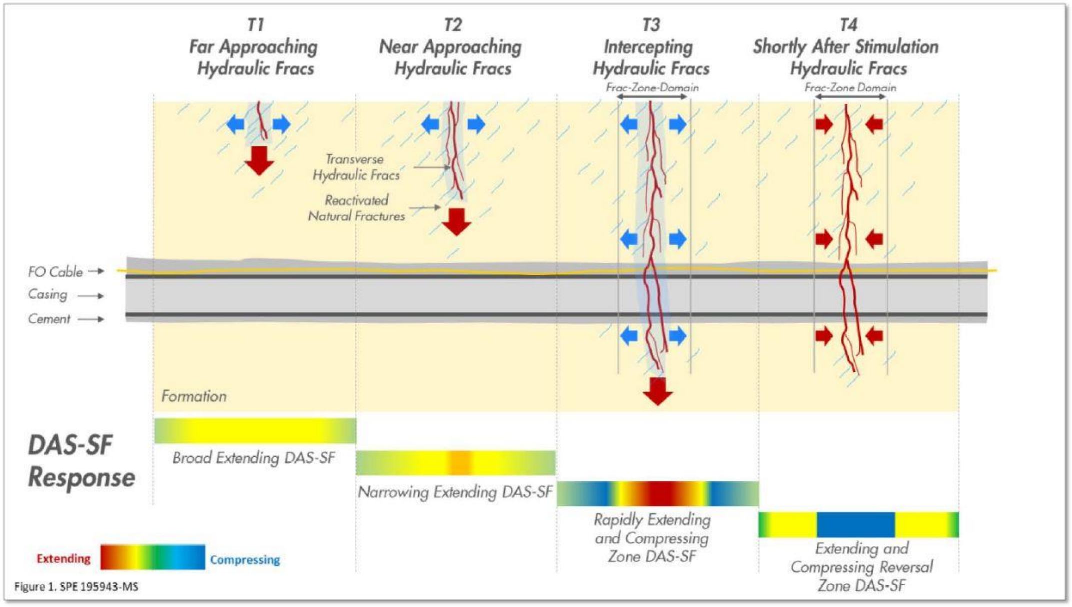

Fig. 1.8 Hypothetical evolution of low-frequency DAS responses with fracture growth in four progressive stages (Reprinted from (Ugueto et al., 2019))

1.3 Objective and Organization of the Dissertation

The objective of this study is to develop an integrated model to simulate the far-field strain rate behavior during hydraulic fracturing. With this model, we can simulate the strain rate responses with various completion scenarios. The general workflow of this simulation study is to simulate fracture geometries using a simple fracture propagation model, and then use the displacement discontinuity method to simulate the displacements in the stimulation domain based on the hypothetical fracture growth. The model will transform the displacements into fiber-measured strain rate responses. In the end, the simulated strain rate will be transformed into polarized patterns by applying a special data processing approach. These patterns can be used in interpreting low-frequency DAS measurements and helping to understand fracture development in multistage fracturing.

This study is presented in six chapters. Chapter 1 reviews the general background of this research, the literature on related subjects, and the research objective. In chapter 2 and Chapter 3, the far-field strain rate model based on rock deformation and fiber-optic measurement for both single fracture and multiple fracture are developed under assumptions. Chapter 4 presents the methodology of the far-field strain rate pattern generation. Single fracture scenarios and multiple fracture scenarios are discussed respectively when generating different patterns. Chapter 5 shows the quantitative study of the far-field strain rate model. The parametric study has been completed to investigate the sensitivity of different parameters to the shape of the patterns. Meanwhile, an empirical correlation has been established based on the simulation results. In Chapter 6, the ideal case pattern system and a field case pattern matching are presented. Chapter 7 summarizes the conclusions from this study and proposes suggestions for future work.

2 MODEL DEVELOPMENT OF SINGLE FRACTURE

2.1 Introduction

The efforts to investigate the stress field surrounding fractures have been conducted for a long time. Sneddon (1946), and Sneddon and Elliot (1946) gave the analytical solution of the stress distribution of a vertical crack in an elastic solid. However, the analytical solution can only be used for single fracture case, not appliable for multiple fracture case. To better understand low-frequency DAS data from the field, we will build a straightforward numerical model that works for both single and multiple fracture scenarios.

Crouch and Starfield (1983) presented a two-dimensional model in semi-analytical approach by applying a special boundary element method with the linear elastic theory, known as two-dimensional displacement discontinuity method (2D DDM). This method allows us to simulate static stress, strain, and displacement near a single fracture and multiple fractures. The two-dimensional displacement discontinuity method simulates fracture with infinite height. Because the assumption for this method is the plain strain where out of the plain direction is vertical. Olson (2004) presented a 3D correction factor that can transform the infinite fracture height to finite fracture height in two-dimensional displacement discontinuity method.

In this chapter, we developed an integrated model to simulate the far-field strain rate along a monitoring well during fracture(s) propagating from an injection well, as shown in Fig. 2.1, by coupling the displacement discontinuity method and a simple fracture propagation model.

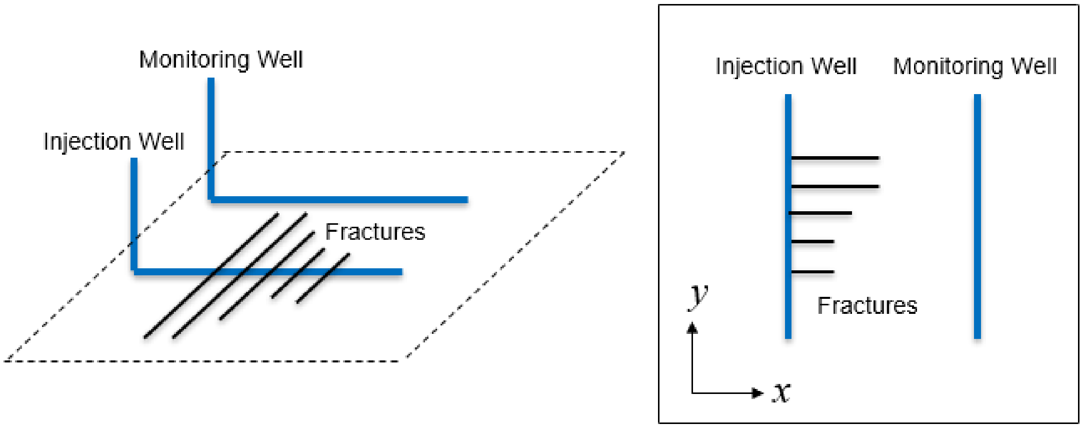

Fig. 2.1 Schematic of the defined problem

The following assumptions have been made to develop the model.

For fracture:

1. Vertical fracture(s) propagating in the straight direction parallel to the maximum horizontal stress, no angle-altered;
2. Constant fracture height;
3. No stress interference among fractures.

For rock:

1. Homogenous and isotropic;
2. Linear elastic.

The model can transform the displacements into fiber-measured strain rate responses with a special data processing approach. Since the strain rate measured by low-frequency DAS is different from the strain rate based on rock deformation, we will discuss the two cases separately.

Fig. 2.2 shows the workflow of the developed model. After loading the synthetic data, the fracture length is calculated by fracture propagation model at one time step by solving Equation 2.45. Then we calculate the fracture width distribution along the fracture by using Equation 2.30. After that, we simulate the stresses and displacements along the fiber location by using displacement discontinuity method (DDM), and they will be used to calculate far-field strain by applying Equation 2.50 (rock deformation) or Equation 2.51 (fiber-optic measurement). At each time step, we will record the far-field strain calculation result along the fiber. This procedure will be performed at each time step, until the stimulation is completed. Then we will calculate the strain rate by taking the derivative of the two adjacent time steps by using Equation 2.52. In the end, pattern generation (special data processing) will be performed to the strain rate data by applying Equation 4.1. The detail about pattern generation will be introduced later in Chapter 4.

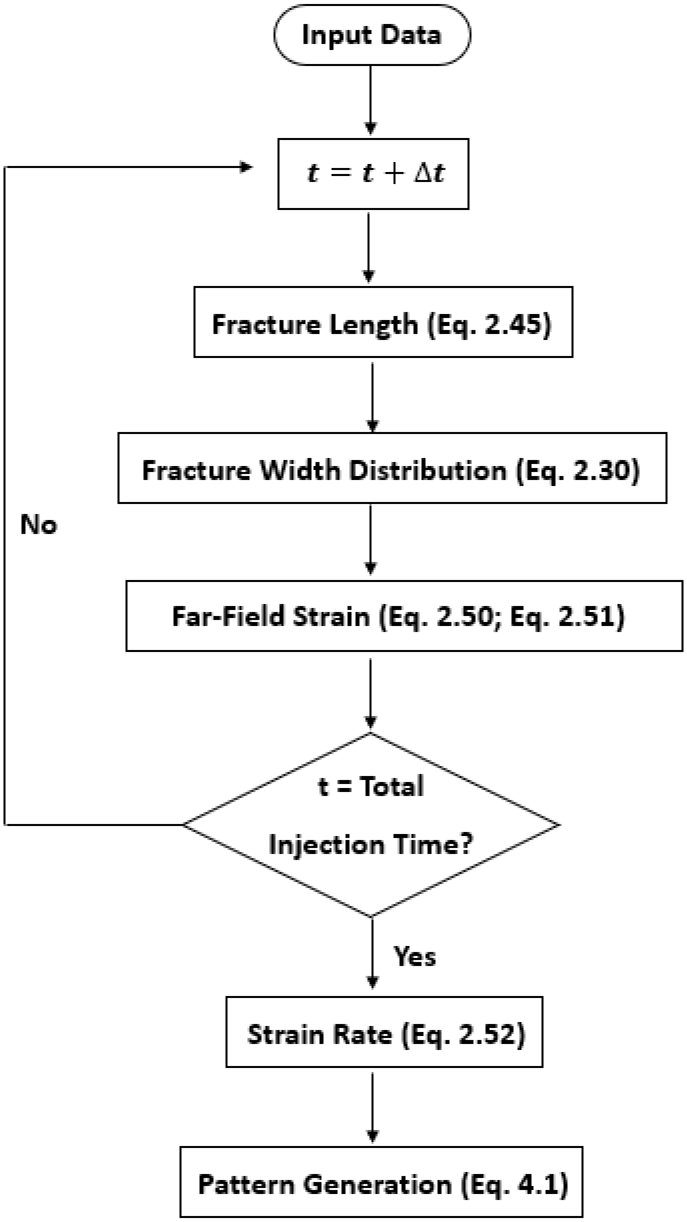

Fig. 2.2 Flowchart of the single fracture model

2.2 Displacement Discontinuity Method

Crouch (1976) developed the displacement discontinuity method, a special boundary element method, to calculate the stress and displacement around a fracture with arbitrary shape in a linear elastic domain. Fig. 2.3 shows a fracture with two-dimensional boundary. The boundary S^+ and S^- are two surfaces of the fracture that divided into multiple elements. The space between the two surfaces is named as a displacement discontinuity, which can influence the stress and displacement at any point in the domain. D_x and D_y are displacement discontinuities in x and y direction, respectively. In this way, the stress and displacement at a single point in the domain can be understood as the total influences of all the displacement discontinuities along the fracture. Thus, solving all the displacement discontinuities along the fracture results in the stress and displacement distribution in the domain. In this way, the stress and displacement at a point ξ in the domain can be calculated by taking the integral of displacement discontinuity Δu_i over the boundary $S^{\pm}$ (Wu, 2014),

$$\sigma_{jk}(\xi) = \int_S \; E_{ijk}(\xi, \eta)\, \Delta u_i(\eta) dS(\eta) \qquad \Delta u_i = u_i^- - u_i^+ \tag{2.1}$$

$$u_j(\xi) = \int_S \; C_{ij}(\xi, \eta)\, \Delta u_i(\eta) dS(\eta) \qquad \Delta u_i = u_i^- - u_i^+ \tag{2.2}$$

where $\sigma_{jk}(\xi)$ is the stress, and $u_j(\xi)$ is the displacement. $E_{ijk}(\xi, \eta)$ and $C_{ij}(\xi, \eta)$ are the quantities representing the influences on stress and displacement respectively at the point ξ by a displacement discontinuity at point η.

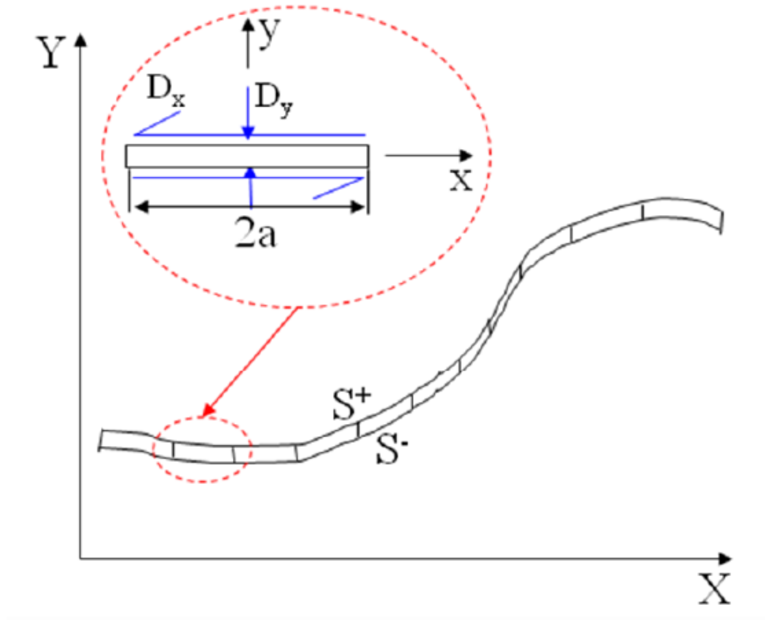

Fig. 2.3 Illustration of a fracture with two-dimensional boundary (Reprinted from (Wu, 2014))

The kernel function $f(x,y)$ of the analytical solution to this problem can be obtained from Crouch's method (1983) as expressed,

$$f(x,y) = \frac{-1}{4\pi(1-\nu)}[y\left(arctan\frac{y}{x-a} - arctan\frac{y}{x+a}\right) - (x-a)ln\sqrt{(x-a)^2+y^2}$$

$$+(x+a)ln\sqrt{(x+a)^2+y^2}] \tag{2.3}$$

where ν is Poisson's ratio, and a is half-length of an element.

The solution of stresses and displacements is a function of $f(x,y)$ given as,

$$\sigma_{xx} = 2GD_x\left[2f_{,xy} + yf_{,xyy}\right] + 2GD_y\left[f_{,yy} + yf_{,yyy}\right] \tag{2.4}$$

$$\sigma_{yy} = 2GD_x\left[-yf_{,xyy}\right] + 2GD_y\left[f_{,yy} - yf_{,yyy}\right] \tag{2.5}$$

$$\sigma_{xy} = 2GD_x\left[f_{,yy} - yf_{,yyy}\right] + 2GD_y\left[-yf_{,xyy}\right] \tag{2.6}$$

$$u_x = D_x\left[2(1-\nu)f_{,y} - yf_{,xx}\right] + D_y\left[-(1-2\nu)f_{,x} - yf_{,xy}\right] \tag{2.7}$$

$$u_y = D_x\left[(1-2\nu)f_{,x} - yf_{,xy}\right] + D_y\left[2(1-\nu)f_{,y} + yf_{,xx}\right] \tag{2.8}$$

where D_x and D_y are displacement discontinuities in the *x* and *y* direction respectively, and *G* is shear modulus,

$$G = \frac{E}{2(1+\nu)} \tag{2.9}$$

where E is Young's modulus, and ν is Poisson’s ratio.

And the derivatives of the function $f(x, y)$, that need to be taken into the calculation of previous solution, through first, second and third order are shown below,

$$f_{,x} = \frac{1}{4\pi(1-\nu)}[\ln\sqrt{(x-a)^2+y^2} - \ln\sqrt{(x+a)^2+y^2}] \tag{2.10}$$

$$f_{,y} = \frac{-1}{4\pi(1-\nu)}[\arctan\frac{x+a}{y} - \arctan\frac{x-a}{y}] \tag{2.11}$$

$$f_{,xx} = \frac{1}{4\pi(1-\nu)}[\frac{x-a}{(x-a)^2+y^2} - \frac{x+a}{(x+a)^2+y^2}] \tag{2.12}$$

$$f_{,yy} = \frac{-1}{4\pi(1-\nu)}[\frac{x-a}{(x-a)^2+y^2} - \frac{x+a}{(x+a)^2+y^2}] \tag{2.13}$$

$$f_{,xy} = \frac{1}{4\pi(1-\nu)}[\frac{y}{(x-a)^2+y^2} - \frac{y}{(x+a)^2+y^2}] \tag{2.14}$$

$$f_{,xyy} = \frac{1}{4\pi(1-\nu)}[\frac{(x-a)^2-y^2}{\{(x-a)^2+y^2\}^2} - \frac{(x+a)^2-y^2}{\{(x+a)^2+y^2\}^2}] \tag{2.15}$$

$$f_{,yyy} = \frac{2y}{4\pi(1-\nu)}[\frac{x-a}{\{(x-a)^2+y^2\}^2} - \frac{x+a}{\{(x+a)^2+y^2\}^2}] \tag{2.16}$$

However, in this study, as the defined problem demonstrated in Fig. 2.1, the objective is to simulate the far-field strain rate along a monitoring well in *y* direction and the propagating fracture(s) are assumed to be vertical in *x* direction and no angle-altered. Therefore, only normal stresses in both the *x* and *y* direction (σ_{xx}, σ_{yy}), and the displacements in the *y* direction (u_y) are needed for the following simulation study. Shear stress (σ_{xy}) and displacements in the *x* direction (u_x) will not be investigated in this work.

In this way, the problem can be simplified as shown in Fig 2.4, a vertical fracture locates in the center of the coordinate, and the fracture is discretized into multiple single elements, as shown in Fig. 2.5. Because of the fracture is vertical to the *y* direction, thus, there are only displacement discontinuities in the *y* direction (D_y) and no displacement discontinuities in the *x* direction (D_x) along the fracture. Therefore, Crouch's method can also be simplified by eliminating the terms with multiplication of D_x. The simplification is shown below.

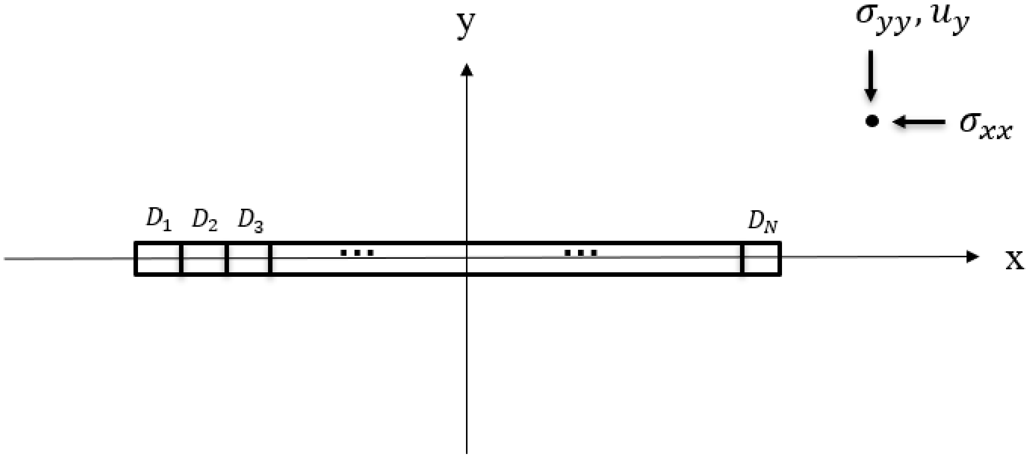

Fig. 2.4 Illustration of a discretized two-dimensional vertical fracture

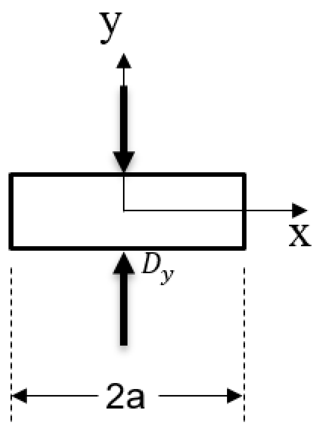

Fig. 2.5 Illustration of a single two-dimensional discretized element

The solution of displacement discontinuity method is point sourced. Therefore, for n^{th} element, its induced stress and displacement at a position (x, y) is given as,

$$\sigma_{xx}^{n} = 2GD_{y}^{n}\left[f_{,yy} + \bar{y}_{n}f_{,yyy}\right] \tag{2.17}$$

$$\sigma_{yy}^{n} = 2GD_{y}^{n}\left[f_{,yy} - \bar{y}_{n}f_{,yyy}\right] \tag{2.18}$$

$$u_{y}^{n} = D_{y}^{n}\left[2(1-\nu)f_{,y} - \bar{y}_{n}f_{,yy}\right] \tag{2.19}$$

Each element will be calculated in its location coordinate system. The local coordinate of the n^{th} element is,

$$\bar{x}_{n} = x - x_{n}, n = 1,2,3, \dots, N \tag{2.20}$$

$$\bar{y}_{n} = y - y_{n}, n = 1,2,3, \dots, N \tag{2.21}$$

where N denotes the number of elements in the fracture.

And the following derivatives of the function $f(x, y)$ are only needed to take into the calculation of the simplified problem,

$$f_{,y} = \frac{-1}{4\pi(1-\nu)}[\arctan\frac{\bar{x}_n+a}{\bar{y}_n} - \arctan\frac{\bar{x}_n-a}{\bar{y}_n}] \tag{2.22}$$

$$f_{,yy} = \frac{-1}{4\pi(1-\nu)}[\frac{\bar{x}_n-a}{(\bar{x}_n-a)^2+\bar{y}_n{}^2} - \frac{\bar{x}_n+a}{(\bar{x}_n+a)^2+\bar{y}_n{}^2}] \tag{2.23}$$

$$f_{,yyy} = \frac{2\bar{y}_n}{4\pi(1-\nu)}[\frac{\bar{x}_n-a}{\{(\bar{x}_n-a)^2+\bar{y}_n{}^2\}^2} - \frac{\bar{x}_n+a}{\{(\bar{x}_n+a)^2+\bar{y}_n{}^2\}^2}] \tag{2.24}$$

Thus, the induced stress and displacement by a whole fracture at a point (x, y) can be expressed as,

$$\sigma_{xx} = \sum_{n=1}^{N} G^n \sigma_{xx}^n \tag{2.25}$$

$$\sigma_{yy} = \sum_{n=1}^{N} G^n \sigma_{yy}^n \tag{2.26}$$

$$u_y = \sum_{n=1}^{N} G^n u_y^n \tag{2.27}$$

The 2D DDM assumes plane strain and the fracture height is infinite. To enhance the reality of the fracture, we adopt a 3D correction factor G^nderived by Olson (2004) that transforms the infinite fracture height to finite fracture height in 2D DDM calculation,

$$G^n = 1 - \frac{d_n^\beta}{[d_n^2+(\frac{h}{\alpha})^2]^{\frac{\beta}{2}}} \tag{2.28}$$

where $\alpha = 1$ and $\beta = 2.3$ are empirical constants, h is the fracture height. And d_n is defined as,

$$d_n = \sqrt{\bar{x}_n{}^2 + \bar{y}_n{}^2} \tag{2.29}$$

2.3 Fracture Propagation Model

For single fracture, KGD model with fixed injection rate and time is used to calculate fracture length, x_f, and net pressure, p_{net}, at each time step. The KGD model was introduced by Khristianovich and Zheltov (1955) and Geertsma and de Klerk (1969). The model assumed that the fracture opens with the same width at any vertical coordinate within the fixed height. The KGD model is determined from the plane strain assumption applied in every horizontal plane, and no variation of fracture width in the vertical direction, as shown in Fig. 2.6. The following derivation of the KGD model is developed based on the SI unit. The conversion to the oilfield unit is introduced later.

The calculation of fracture width is based on analytical solution of a crack in an infinite linear elastic solid developed by Sneddon (1951),

$$w(x) = \frac{4p}{E'}(L^2 - x^2)^{\frac{1}{2}} \tag{2.30}$$

where $w(x)$ is the width along the crack at the location of x, p is the constant net pressure inside the crack, L is the half-length of the crack, E' is plane strain modulus and defined as

$$E' = \frac{E}{1-\nu^2} \tag{2.31}$$

where E is Young's modulus, and ν is Poisson's ratio.

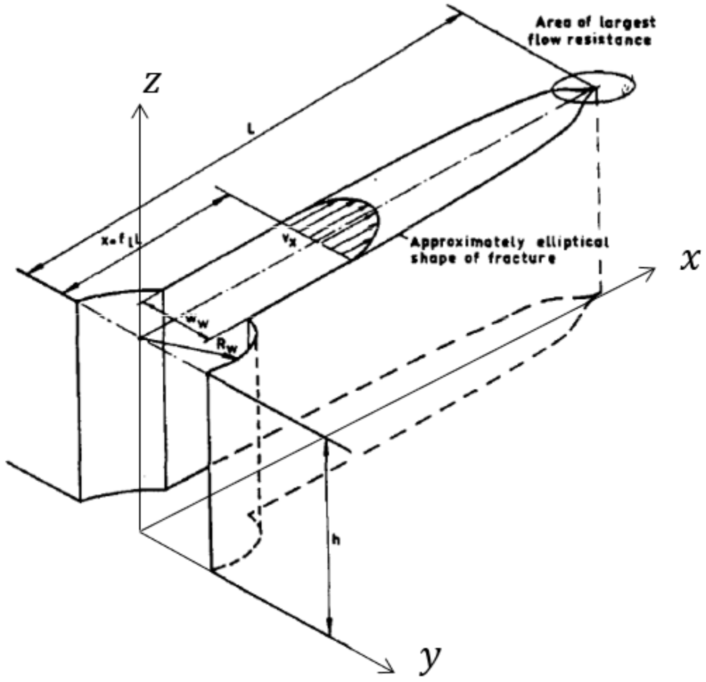

Fig. 2.6 KGD fracture schematic diagram (Reprinted from (Geertsma and de Klerk, 1969))

The assumption of KGD model of flow rate is everywhere equal to the injection rate, q. Since the model has a rectangular flow channel perpendicular to fracture propagation direction, assuming a Newtonian fluid, the total pressure drop from the wellbore to the fracture tip can be given by,

$$p_{n,w} - p_{n,tip} = \frac{12\mu q x_f}{h_f}\left(\frac{1}{x_f}\int_0^{x_f}\frac{1}{w^3}dx\right) \tag{2.32}$$

where $p_{n,w}$ is net pressure at the wellbore, $p_{n,tip}$ is net pressure at the fracture tip, μ is viscosity of injection fluid, q is the injection rate per one wing, x_f is the half of the fracture length, h_f is the fracture height, and w is the fracture width.

Valko and Economides (1995) made the following three assumptions to enhance the reality of the KGD model. Firstly, the pressure equals the wellbore pressure almost everywhere. From Equation 2.30, the wellbore pressure is related to fracture width at the wellbore as,

$$w_w = \frac{4x_f p_{n,w}}{E'} \tag{2.33}$$

where w_w is the fracture width at wellbore. Secondly, the net pressure at the fracture tip is zero,

$$p_{n,tip} = 0 \tag{2.34}$$

Thirdly, the average value of $1/w(x)^3$can be obtained from its value at the wellbore multiplied by a constant which is postulated to be $7/\pi$. The explanation and derivation of this assumption are well documented in their literature. Therefore, we can obtain,

$$\left(\frac{1}{x_f}\int_0^{x_f}\frac{1}{w^3}dx\right) = \frac{1}{w_w^3}\cdot\frac{7}{\pi} \tag{2.35}$$

combining Equation 2.32 to Equation 2.35, we can get,

$$p_{n,w} = \frac{84\mu q x_f}{\pi h_f w_w^3} \tag{2.36}$$

then the wellbore width can be expressed as following by combining Equation 2.33 and Equation 2.36,

$$w_w = \sqrt[4]{\frac{336\mu q x_f^2}{\pi E' h_f}} = 3.22\left(\frac{\mu q x_f^2}{E' h_f}\right)^{\frac{1}{4}} \tag{2.37}$$

Knowing the average fracture width can be calculated by the product of the wellbore fracture width and a shape factor (Valko and Economides, 1995),

$$\bar{w} = w_w \cdot \gamma \tag{2.38}$$

where $\bar{w}$ is the average fracture width and γ is the shape factor.

For the KGD model, the shape factor has no vertical component. And the elliptical shape in the horizontal direction makes the only contributor to the shape factor that can be given by,

$$\gamma = \frac{\pi}{4} \tag{2.39}$$

Combining Equation 2.37 to Equation 2.39, the average width can be expressed as,

$$\bar{w} = \frac{\pi}{4}(\frac{336}{\pi})^{\frac{1}{4}}(\frac{\mu q x_f^2}{E' h_f})^{\frac{1}{4}} = 2.53(\frac{\mu q x_f^2}{E' h_f})^{\frac{1}{4}} \tag{2.40}$$

In this research, for simplicity, assumptions have been made to the fracture geometry to reduce uncertain parameters in the complex flow system. The material balance within the fracture can be written as,

$$\frac{\partial q}{\partial x} + q_L + \frac{\partial A}{\partial t} = 0 \tag{2.41}$$

where q is flow rate through the fracture cross section, q_L is volume rate of fluid loss to the formation per unit length of fracture, and *A* is the cross-sectional area of the fracture.

Carter's equation (Carter, 1957) is used to evaluate the fluid loss, which is expressed as,

$$q_L = \frac{2C_L h_f}{\sqrt{t-\tau(x)}} \tag{2.42}$$

where C_L is the fluid loss coefficient and $\tau(x)$ is the time at which fracture reaches position x.

To obtain the analytical form of the material balance, integrations should be taken over the fracture half-length, x_f, and total injection time, t_e.

$$\int_0^{t_e}\int_0^{x_f}\frac{\partial q}{\partial x}dxdt + \int_0^{t_e}\int_0^{x_f} q_L dxdt + \int_0^{t_e}\int_0^{x_f}\frac{\partial A}{\partial t}dxdt = 0 \tag{2.43}$$

The analytical solution (Al Jawad, 2018) can be expressed as a function of time, t, and position, x, as follows,

$$qt - 2xh_f(\kappa C_L\sqrt{t} + S_p) - \overline{w}xh_f = 0 \tag{2.44}$$

where κ is the opening time distribution factor, and S_p is the spurt loss coefficient. In this dissertation, we assume $\kappa = 1$, and $S_p = 0\ in$ for all the simulations.

Transforming Equation 2.44 to oilfield unit, it becomes,

$$5.615 \cdot qt - 2xh_f c_L\sqrt{t} - 0.0274 \cdot \left(\frac{\mu q x^2}{E' h_f}\right)^{\frac{1}{4}} \cdot xh_f = 0 \tag{2.45}$$

where q in bbl/min, t in min, h_f in ft, $C_L$in $ft/min^{0.5}$, μ in cp, E'in psi, and x in ft.

After solving the fracture length from Equation 2.45, combining with Equation 2.33 and Equation 2.37, net pressure can be calculated with transforming to oilfield unit,

$$p_{net} = 0.0087 \cdot \frac{E'}{x_f} \cdot \left(\frac{\mu q x_f^2}{E' h_f}\right)^{\frac{1}{4}} \tag{2.46}$$

where p_{net} in psi, E'in psi, and x_f in ft, q in bbl/min, h_f in ft, μ in cp.

In this dissertation, we tried to apply around 50% of the total leak-off for the case studies which is close to reality in the field.

2.4 Space Domain Calculation

The notion of space domain, or also referred to as stimulation domain in this dissertation, is compared to that of time domain. As a matter of fact, a dynamic field is associated with time, thus when considering time, it is dynamically solving the problem. To simplify the solution, we solve the space domain separately from the time domain for the problem. At each time step, we solve a static problem in the defined space domain for stress and displacement. We then use a fracture propagation model to advance the fracture. Once the new fracture space domain is generated, we solve the stress and displacement problem within a new space domain. The purpose of investigating space domain is to solve a series of static physical quantities, such as stress, displacement, strain, and characterize their distribution.

The entire hydraulic stimulation process is broken down into multiple static "snapshots" of the space domain. Each "snapshot" depicts the fracture's current shape and the geo-mechanical information in its space domain.

Furthermore, with stitching the "snapshots" of static stress, displacement, and strain in all time steps, dynamic progress of rate of change over time can be made to simulate rock deformation and fiber-optic measurement. This content will be introduced later.

2.4.1 Stress and Displacement Domain Calculation

The stresses in the space domain include two normal stresses (σ_{xx}, σ_{yy}) and a shear stress (σ_{xy}). In this study, as mentioned before, all fractures are considered as vertical. Thus, there is no shear stress considered. The focus of this study is evaluating and interpreting the measurements by fiber-optic sensors. Fiber-optic sensors measure physical responses through the axial stretch of the cable. Based on this, the stress domain considered in this study only refers to the normal stress perpendicular to the fractures and parallel to the fiber.

The same principle applies to the displacement domain as well. The displacement mentioned in this dissertation refers to the displacement in the *y* direction normal to the fractures.

Fig. 2.7 shows an example of a synthetic single fracture located in the space domain. The input data are listed in Table 2.1. Displacement discontinuity method (DDM) is used to solve the stress and displacement domain inside of the space domain.

Using DDM to solve the stresses and displacements in the space domain requires the known displacement discontinuities (fracture width) along the fracture. Therefore, we first need to use the input data to calculate the fracture width along the fracture.

As introduced in the last section, we use the KGD model to propagate fracture. Thus, for a "Snapshot" of the space domain by certain time step, we can use Equation 2.30 to calculate the fracture width distribution along the fracture.

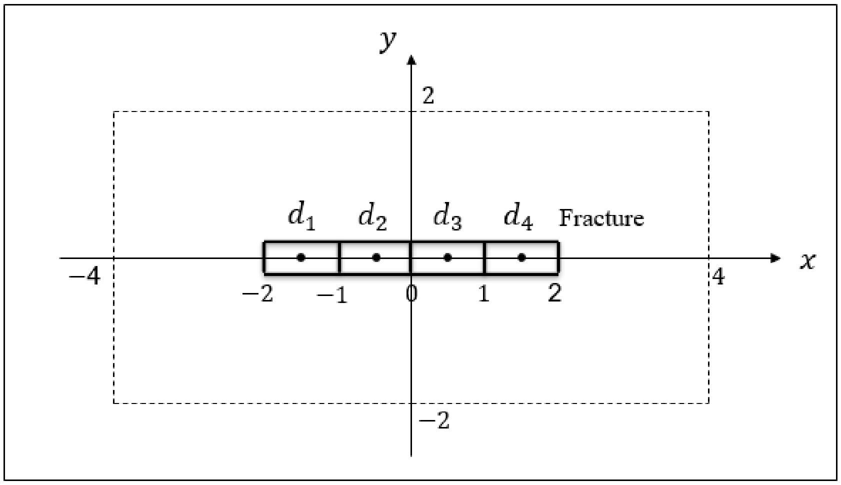

Fig. 2.7 Illustration of the synthetic single fracture in space domain

Table 2.1 Input data for the synthetic single fracture space domain calculation

Parameter	Value
Fracture length, ft	4
Fracture height, ft	100
Young's modulus, psi	4350000
Poisson's ratio, /	0.2
Net pressure, psi	145

In this case, the fracture is discretized into four elements. From -2 to 2 on the *x* axial, the fracture width along the fracture is named as d_1, d_2, d_3, d_4. It is assumed that the net pressure along the fracture is constant. By applying the input data listed in Table 2.1, the fracture width distribution (ft) can be calculated as shown,

$$\begin{bmatrix} d_1 \\ d_2 \\ d_3 \\ d_4 \end{bmatrix} = \begin{bmatrix} 0.000169 \\ 0.000248 \\ 0.000248 \\ 0.000169 \end{bmatrix} \tag{2.47}$$

After obtaining the fracture distribution, by applying Equation 2.25 to Equation 2.27, the stress (psi) and displacement (in) domain can be calculated,

$$\sigma_{yy} = \begin{bmatrix} 28.82 & 28.76 & -18.87 & -82.10 & -82.10 & -18.87 & 28.76 & 28.82 \\ 34.30 & 69.58 & -6.36 & -120.53 & -120.53 & -6.36 & 69.58 & 34.30 \\ 34.30 & 69.58 & -6.36 & -120.53 & -120.53 & -6.36 & 69.58 & 34.30 \\ 28.82 & 28.76 & -18.87 & -82.10 & -82.10 & -18.87 & 28.76 & 28.82 \end{bmatrix}$$

……………………………………………………………………………………… (2.48)

$$u_y = 10^{-4} \cdot \begin{bmatrix} -1.6 & -3.2 & -6.4 & -9.7 & -9.7 & -6.4 & -3.2 & -1.6 \\ -0.4 & -1.1 & -6.6 & -13.3 & -13.3 & -6.6 & -1.1 & -0.4 \\ 0.4 & 1.1 & 6.6 & 13.3 & 13.3 & 6.6 & 1.1 & 0.4 \\ 1.6 & 3.2 & 6.4 & 9.7 & 9.7 & 6.4 & 3.2 & 1.6 \end{bmatrix}$$

……………………………………………………………………………………… (2.49) and the stress domain can be plotted in the waterfall as shown in Fig. 2.8, and the displacement domain can be plotted in the waterfall as shown in Fig. 2.9.

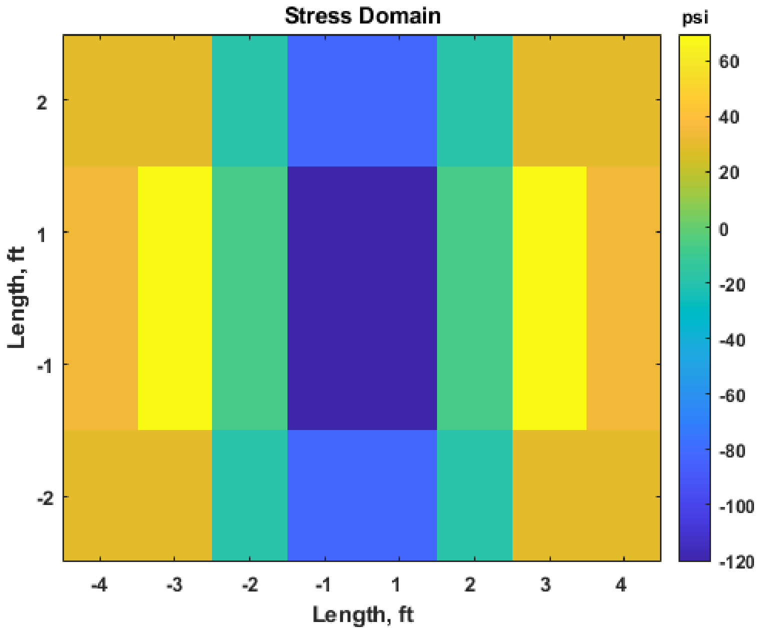

Fig. 2.8 Illustration of the stress domain of the synthetic single fracture

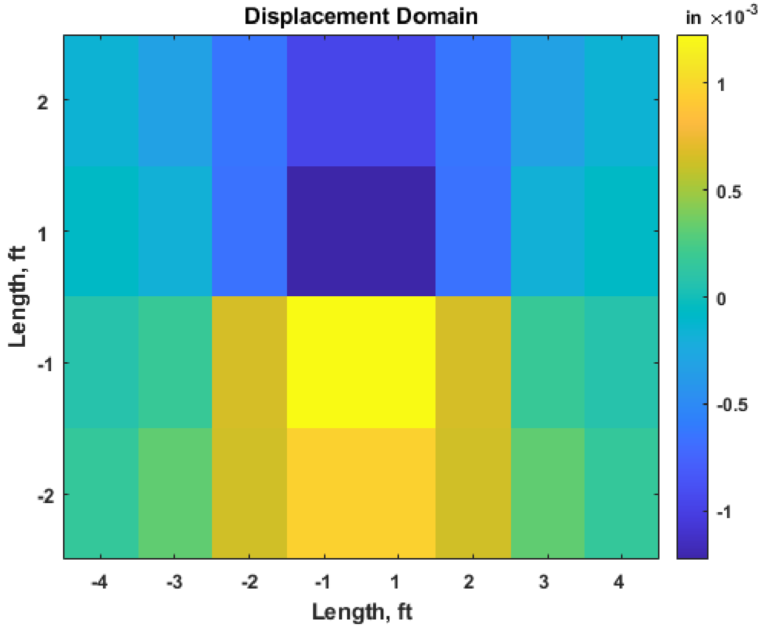

Fig. 2.9 Illustration of the displacement domain of the synthetic single fracture

To compare with the fracture of the field size, we demonstrate another case study for a single fracture. As shown in Fig. 2.10, a single fracture locates in the space domain, and the input data are listed in Table 2.2. The dashed lines at 200 ft, 300 ft, and 400 ft are the observation location lines. The 200 ft line locates behind the fracture tip. The 300 ft line locates on the fracture tip. The 400 ft line locates beyond fracture tip. The stress and displacement details along these lines are further investigated for stress and displacement distribution.

In this dissertation, we assume that bi-wing hydraulic fractures are symmetrical when they extend to each side of the wellbore. Therefore, for the convenience of discussing the defined problem, we only demonstrate half of the fracture.

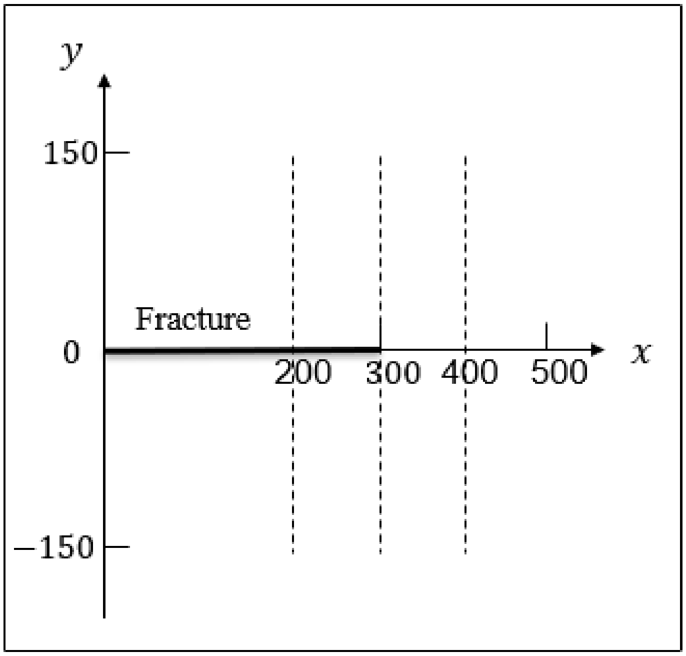

Fig. 2.10 Illustration of the single fracture in the space domain

Table 2.2 Input data for the single fracture space domain calculation

Parameter	Value
Fracture half-length, ft	300
Fracture height, ft	100
Young's modulus, psi	4350000
Poisson's ratio, /	0.2
Net pressure, psi	145
Gauge length, m	2

Following the procedure of the last example, we first solve the fracture width along the fracture, as shown in Fig. 2.11. Afterward, the stress and displacement distribution can be generated by applying 2D DDM.

The stress domain calculation result is shown in Fig. 2.12. The stress calculation results along three observation lines are shown in Fig. 2.13, Fig. 2.14, and Fig.2.15.

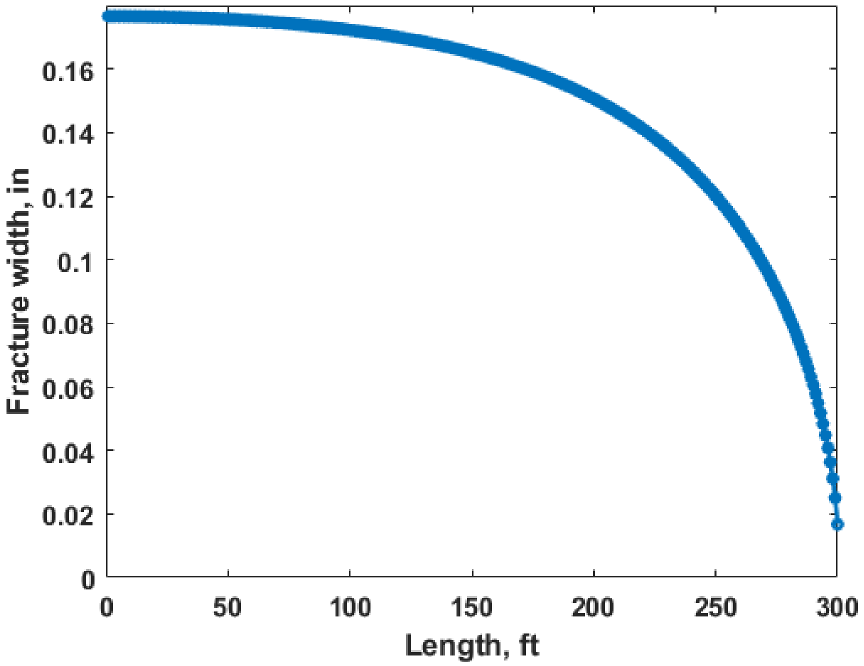

Fig. 2.11 Width distribution along the fracture

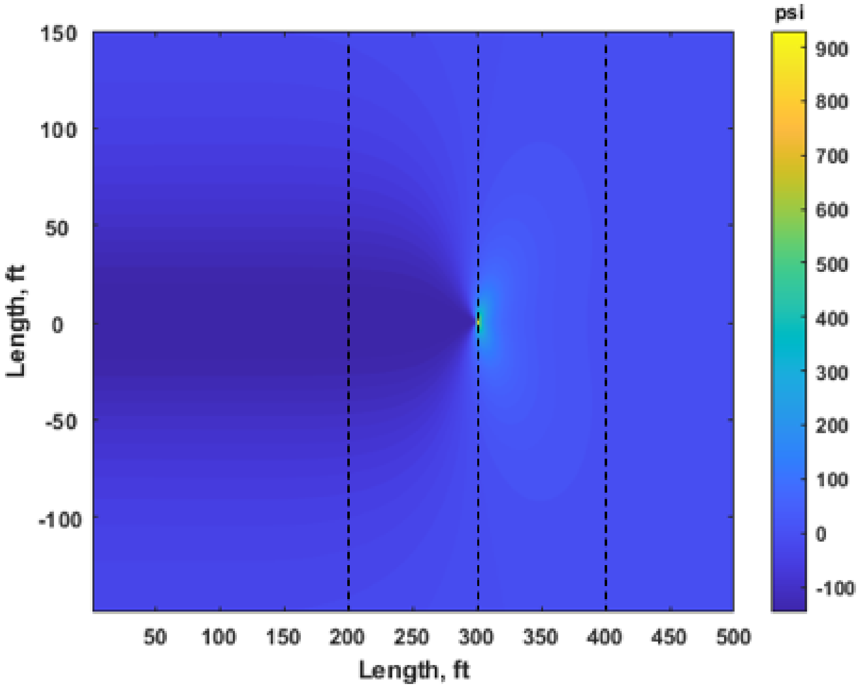

Fig. 2.12 Stress domain of the single fracture case

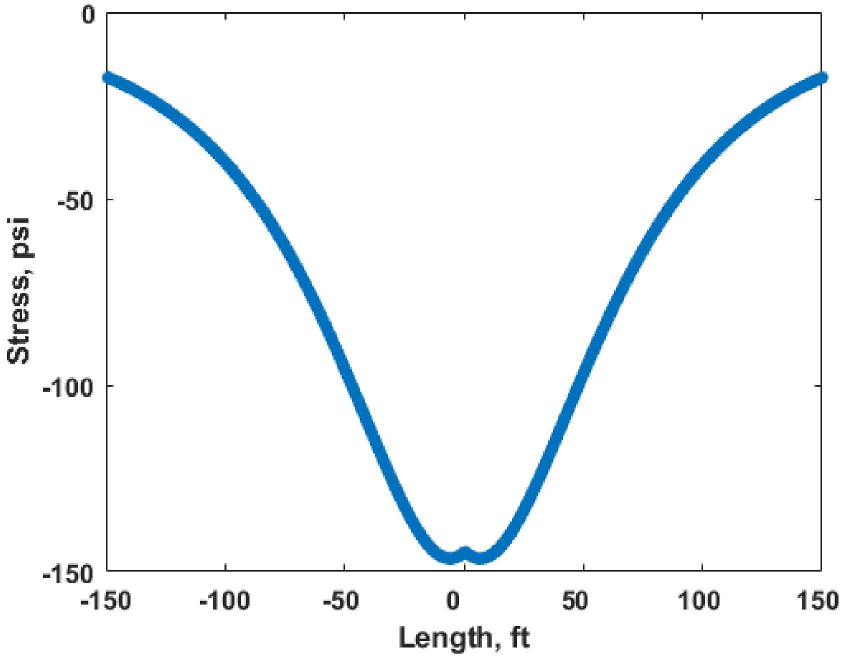

Fig. 2.13 Stress distribution along the 200 ft location of the single fracture case

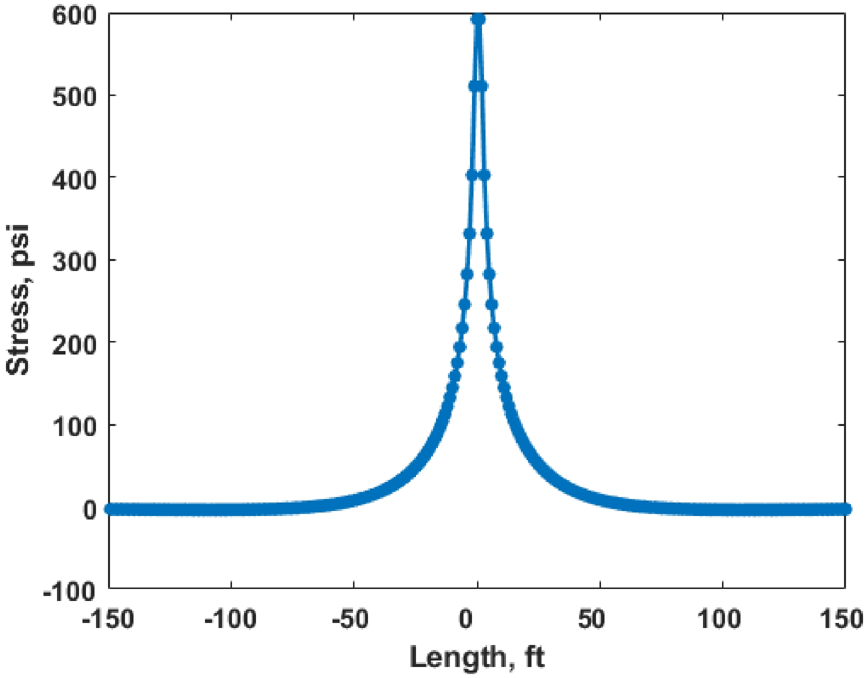

Fig. 2.14 Stress distribution along the 300 ft location of the single fracture case

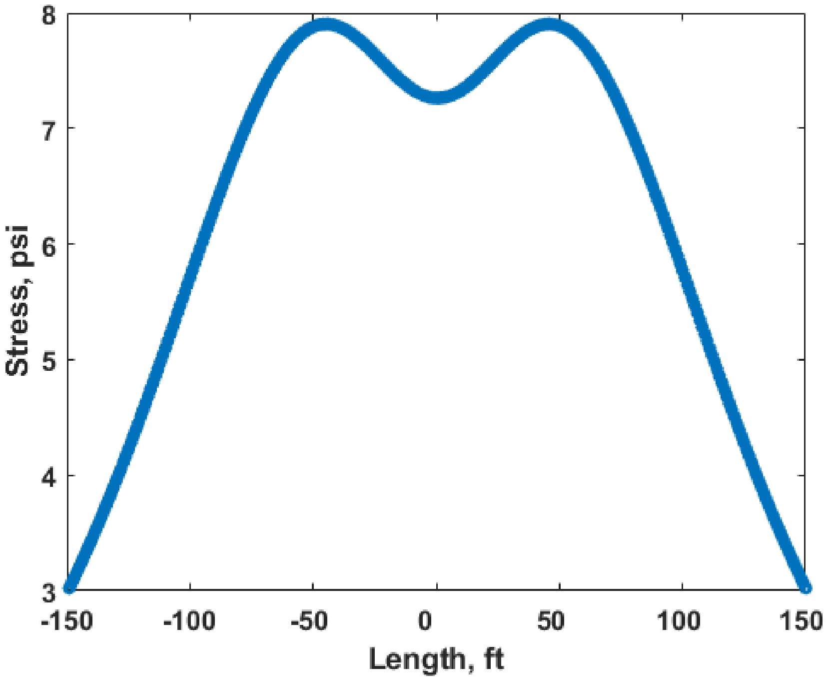

Fig. 2.15 Stress distribution along the 400 ft location of the single fracture case

As the simulation shows in Fig. 2.12, the stress domain consists of the compressive zones (negative numbers) and the tensile zones (positive numbers). The compressive zones are located outside the fracture at both sides of the fracture because the fracture is pushing the rock. The tensile zones are located in front of the fracture tip. From Fig. 2.13, we can see that, at both sides of the fracture, the magnitude of stresses decreases as the location far away from the fracture. Fig. 2.14 shows, right at the fracture tip, there are the largest tensile stresses. A “heart shape” of the stress distribution can be observed in Fig. 2.15.

After showing the simulation of the stress domain, the simulation of the displacement domain is performed. The displacement domain calculation result is shown in Fig. 2.16. The displacements along the three observation lines are shown in Fig. 2.17, Fig. 2.18, and Fig.2.19.

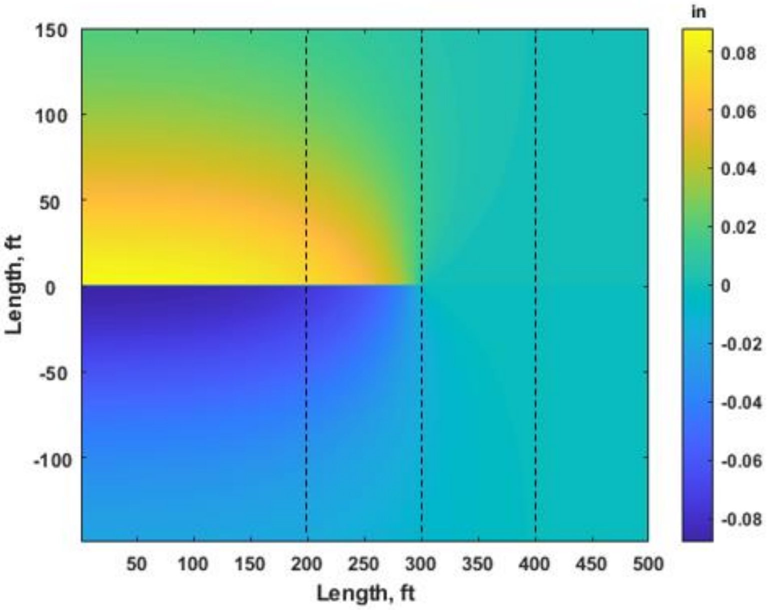

Fig. 2.16 Displacement domain of the single fracture case

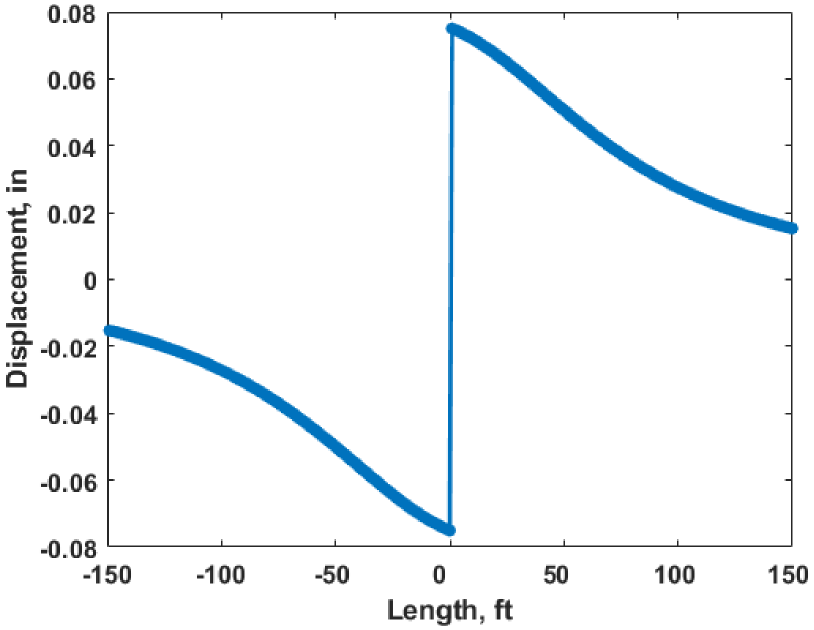

Fig. 2.17 Displacement distribution along the 200 ft location of the single fracture case

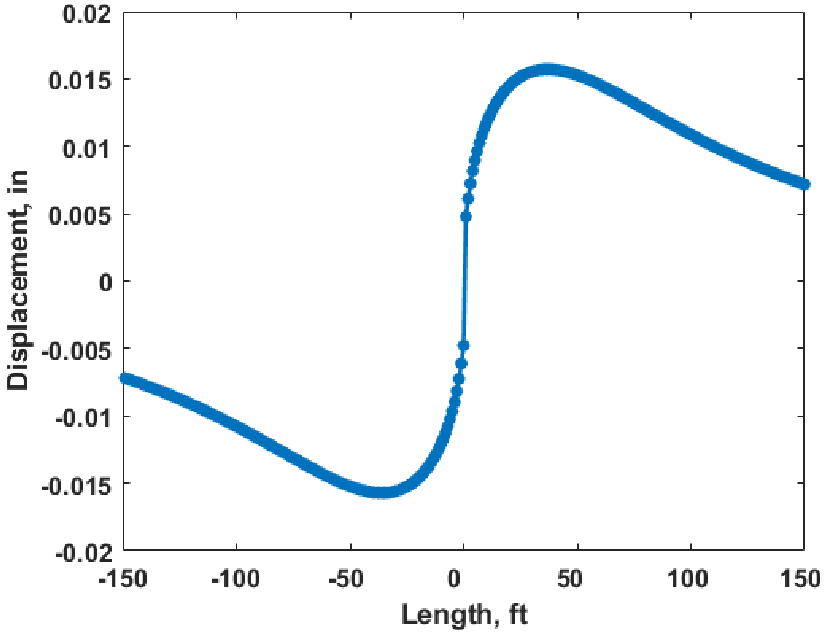

Fig. 2.18 Displacement distribution along the 300 ft location of the single fracture case

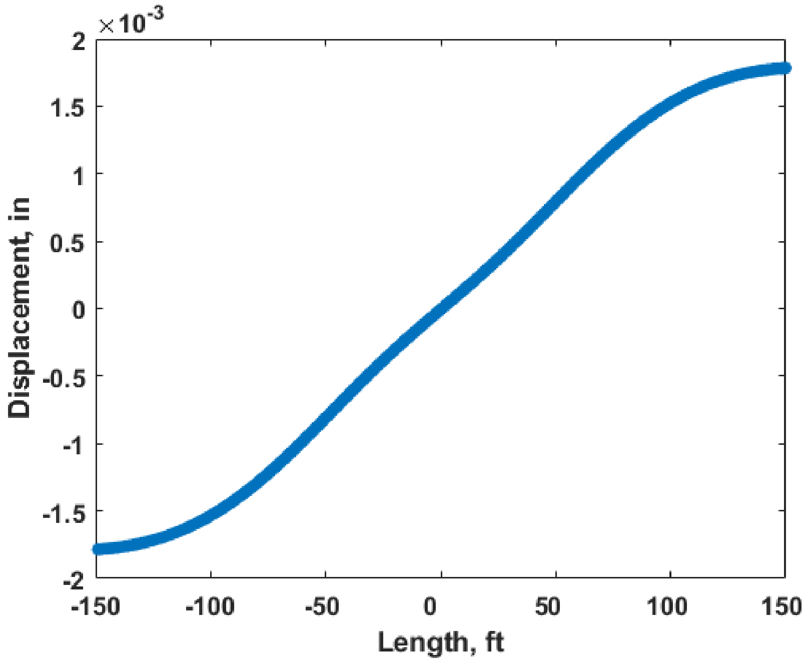

Fig. 2.19 Displacement distribution along the 400 ft location of the single fracture case

Fig. 2.16 shows the displacement domain due to the opened fracture. Taking the fracture and its extending line as a benchmark, the displacement distribution can be divided into two regions. The region on one side of the benchmark, and the region on the other side of the benchmark. The displacements on both sides of the benchmark are in the opposite direction against each other. In this case, the upper side displays positive numbers, and the lower side displays negative numbers. This is because the fracture squeezes the rock and makes them move in the opposite direction. And the magnitude of the displacements in front of the fracture is much smaller than the ones on the two sides of the fracture.

As we can see in Fig. 2.17, on different sides of the fracture, the direction of the displacement is different against each other, and the magnitude of displacement decreases as the location far away from the fracture. In Fig. 2.18, we can find the smallest displacement along the fracture at the fracture tip. Fig. 2.19 shows, in front of the fracture tip, the direction of the displacement is different against each other. However, opposite from displacement on both sides of the fracture, the magnitude of the displacement in front of the fracture increases as the location far away from the center.

2.4.2 Strain Domain Calculation Based on Rock Deformation

In two-dimensional elasticity, plane stress means that the stresses are restricted to a single plane. In this way, axial plain strain can be determined as,

$$\varepsilon_{yy} = \frac{(1-\nu^2)}{E}\left[\sigma_{yy} - \frac{\nu}{1-\nu}\sigma_{xx})\right] \tag{2.50}$$

where σ_{xx} and σ_{yy} are plane stresses in different directions, *E* is Young's modulus, and ν is Poisson's ratio.

Thus, we are going to simulate the strain domain based on rock deformation of the single fracture case above.

The same single fracture case is used, shown in Fig. 2.10. We can calculate both normal stresses, σ_{xx} and σ_{yy}, by using two-dimensional displacement discontinuity method. After obtaining the normal stresses, strain can be calculated by Equation 2.50. The strain distribution is shown in Fig. 2.20, and the strain distribution along the fracture at 200 ft, 300 ft, and 400ft locations are shown in Fig. 2.21, Fig. 2.22, and Fig. 2.23.

Similar to the stress domain, the strain domain consists of two types of regions as well. The compressive zones (negative numbers) locate on the sides of the fracture. The tensile zones (positive numbers) locate at the front of the fracture. As shown in Fig. 2.20, on the sides of the fracture, the strain decreases as the location far away from the fracture. And the tensile zone locates in front of the fracture tip. Right at the fracture tip, there is the largest tensile strain. And a "heart shape" of the strain distribution can be detected. Comparing the magnitude of strain, there is a compelling tensile zone in front of the fracture tip than the compressive ones on both sides of the fracture.

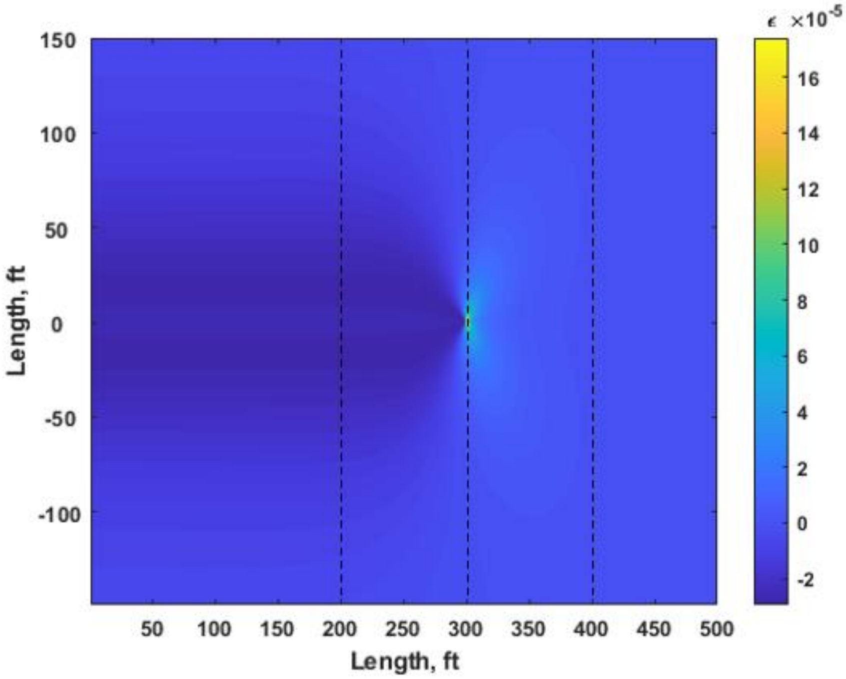

Fig. 2.20 Strain domain of the single fracture case based on rock deformation

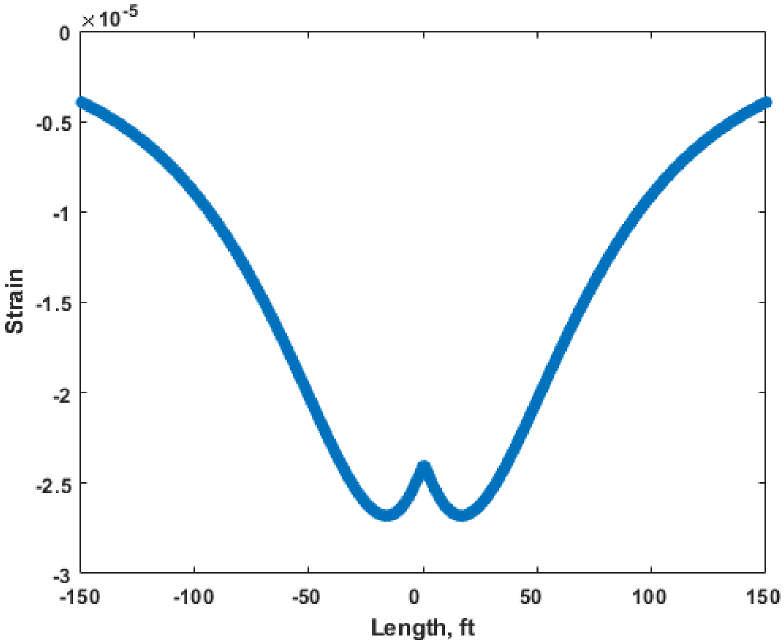

Fig. 2.21 Strain distribution based on rock deformation along the 200 ft location of the single fracture case

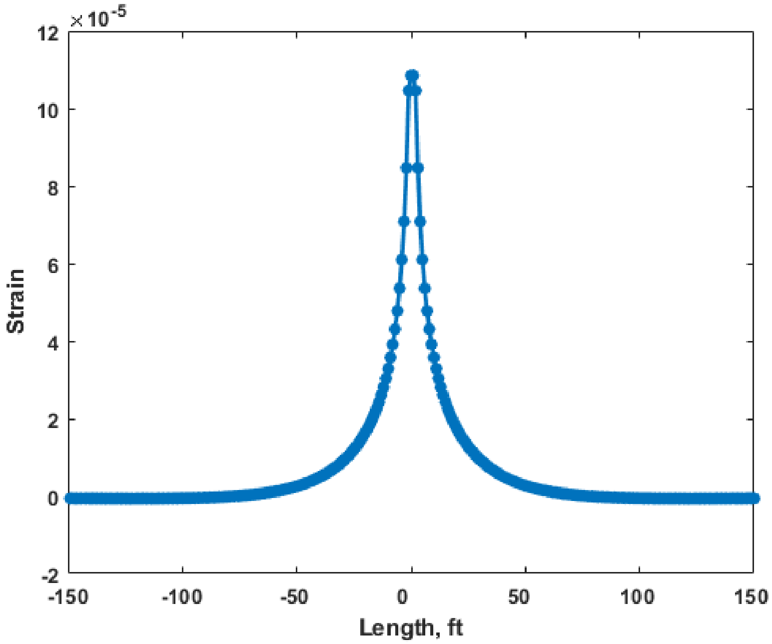

Fig. 2.22 Strain distribution based on rock deformation along the 300 ft location of the single fracture case

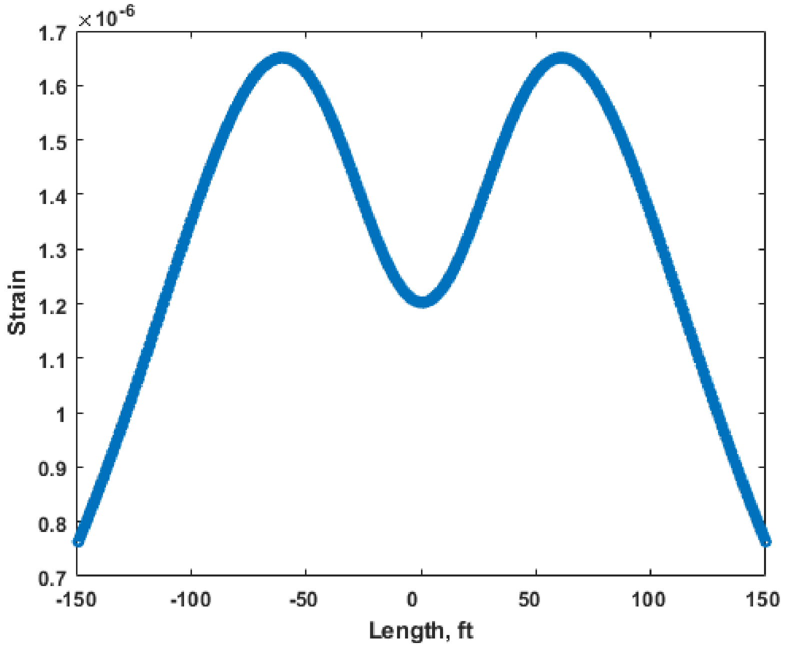

Fig. 2.23 Strain distribution based on rock deformation along the 400 ft location of the single fracture case

2.4.3 Strain Domain Calculation Based on Fiber-Optic Measurement

As introduced before, when a fiber-optic sensor is permanently deployed, it is usually cemented outside the casing. With good cementing, the fiber-optic sensor is considered as in good mechanically coupled with the formation. In such case, the strain rate variations of formation due to hydraulic fracturing can be measured by the optical fiber. However, the strain measurements by fiber-optic sensors are the difference of displacement over a gauge length.

DAS generates digital waveforms at each channel that are not a point measurement but are strain changes measured over a spatial distance. This distance is referred to as gauge length (Dou et al., 2017). Gauge length should not confuse with spatial resolution.

It is not necessarily equal to the spatial resolution, which is a measurement performance parameter. The gauge length of DAS can be very different from different manufacturers or service providers based on different use.

Thus, the fiber measured strain differs from the rock deformation strain. Fiber measured strain can be expressed as,

$$\varepsilon_{yy} = \frac{u_y^{(j+\frac{1}{2}GL)} - u_y^{(j-\frac{1}{2}GL)}}{GL} \tag{2.51}$$

where u_y is the positional displacement vector in direction y parallel to the offset well, with the superscripts indicating positions, j indicates positions along the fiber, and GL is the fiber's gauge length.

Strain domain based on fiber-optic measurement for single fracture case is studied. The same single fracture case shown in Fig. 2.10 is used, with input data listed in Table 2.2, we can calculate the displacement in the y direction, u_y, by using two-dimensional displacement discontinuity method. After obtaining the displacements, strain by fiber-optic measurement can be calculated by Equation 2.51. The calculated strain distribution is shown in Fig. 2.24, and the strain distribution along the fracture at 200 ft, 300 ft, and 400 ft locations are shown in Fig. 2.25, Fig. 2.26, and Fig. 2.27.

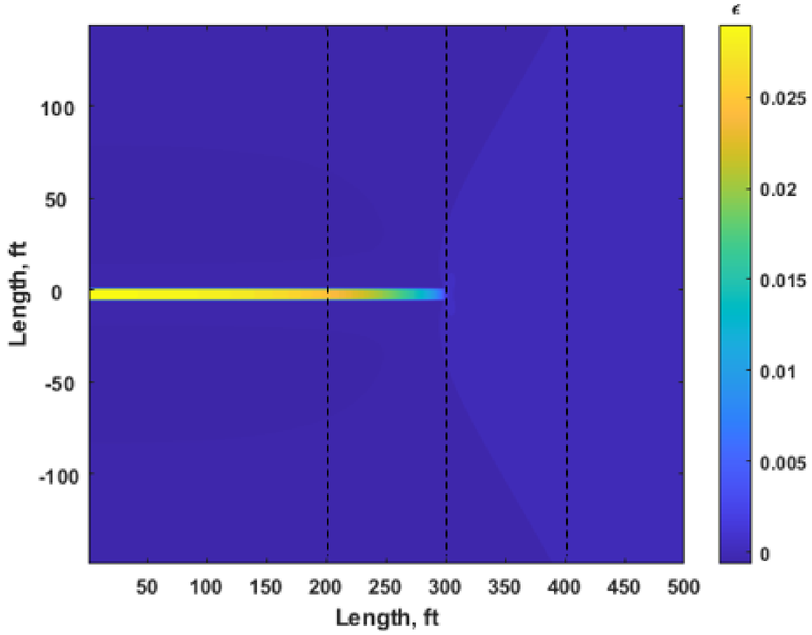

Fig. 2.24 Strain domain of the single fracture case based on fiber-optic measurement

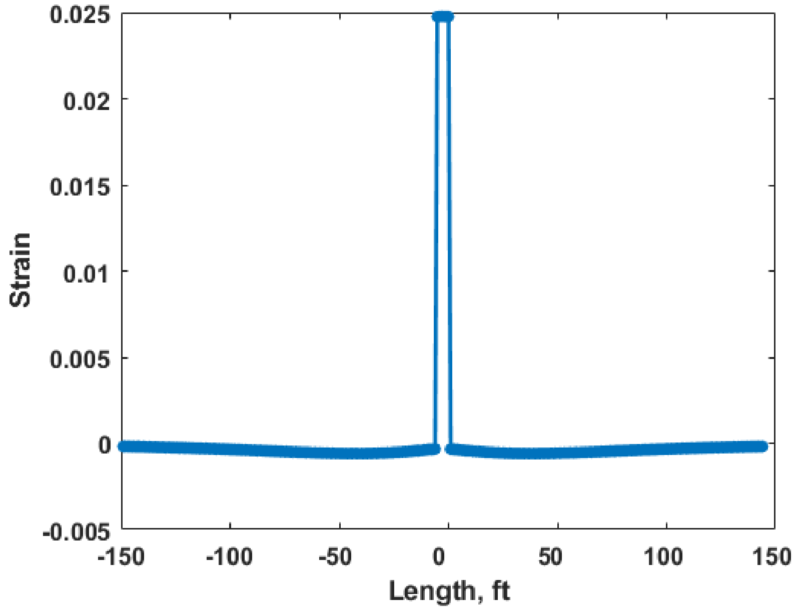

Fig. 2.25 Strain distribution based on fiber-optic measurement along the 200 ft location of the single fracture case

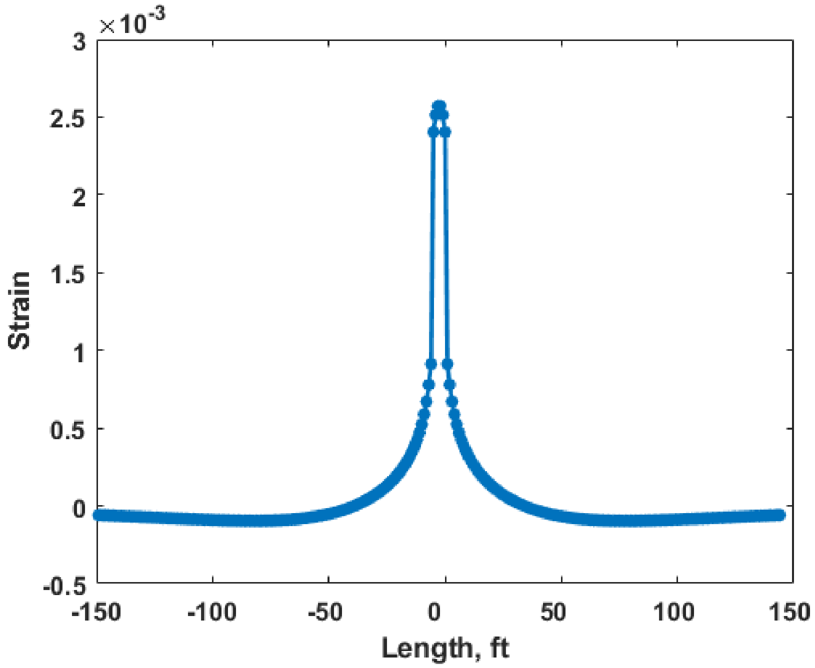

Fig. 2.26 Strain distribution based on fiber-optic measurement along the 300 ft location of the single fracture case

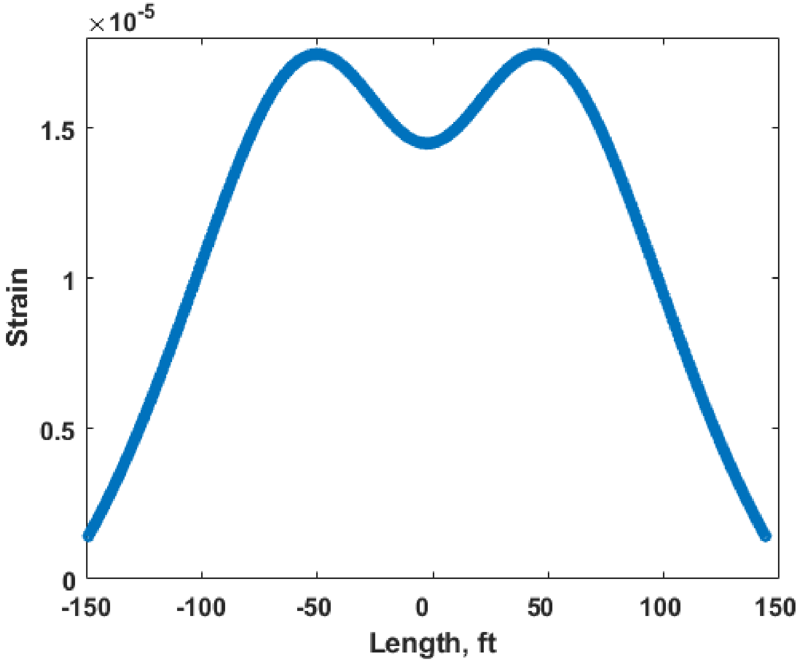

Fig. 2.27 Strain distribution based on fiber-optic measurement along the 400 ft location of the single fracture case

The strain domain based on fiber-optic measurement has tensile zones (positive numbers) locate on the fracture, and in the front of the fracture tip. And the tensile zone along the fracture appears a “strip” shape. However, the compressive zone can hardly find in the strain domain based on fiber-optic measurement.

By comparing Fig. 2.20 and Fig. 2.24, we can find that the strain distribution based on fiber-optic measurement differs from the strain distribution based on rock deformation. The stain based on fiber-optic measurement has a “strip” of extension zone on the fracture location. This is because the strain based on the fiber-optic measurement is calculated by the displacement over a certain gauge length, and the displacement direction on each side of the fracture is different from each other. Thus, we see a “strip” in Fig. 2.24. And the width of the “strip” is equal to the magnitude of the gauge length. Therefore, the larger the gauge length, the wider the “strip” will get from the displacement simulation based on fiber-optic measurement. From the magnitude point of view, the strain calculation based on fiber-optic measurement cannot match the real strain of rock deformation. It can only represent the same trend and status of the rock as compression or extension.

2.5 Strain Rate Calculation Model

As mentioned before, this dissertation aims at using DAS measurements for cross-well hydraulic fracture monitoring. The illustration of the problem is shown in Fig. 2.1. The objective of this study is to investigate the far-field strain rate behavior at fiber-optic sensors locations in a nearby well during hydraulic fracturing, and detect the fractures propagate from injection well to monitoring well from strain rate behavior.

As we have developed strain calculation method and fracture propagation model, by coupling those two, strain rate can be calculated by taking the derivative of the two adjacent time steps. Strain rate calculation will be presents based on rock deformation and fiber-optic measurement, respectively.

Using the fracture propagation model that we developed to propagate fractures, multiple time-lapse strain responses can be simulated at different time step. To obtain the far-field strain rate data that we are interested, an imaginary offset well is set in the simulated space domain parallel to the wellbore with a giving well spacing, as shown in Fig. 2.28.

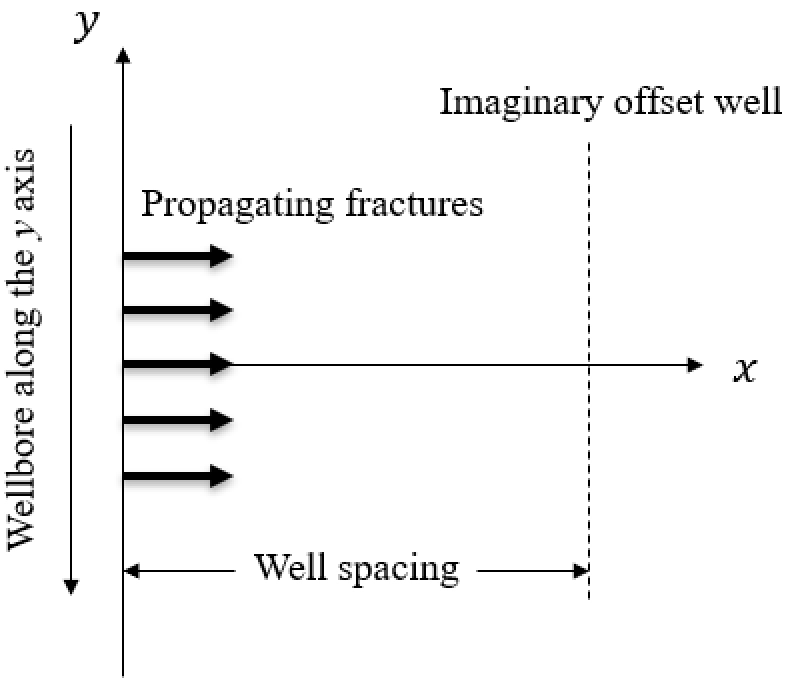

Fig. 2.28 Schematic of the cross-well monitoring for multiple fracture treatment

Recording the stress and displacement value at the imaginary offset well at all time steps, strain based on rock-deformation and strain based on fiber-optic measurement can be calculated. Strain rate can be simulated in the time domain by taking the difference of strain value at the imaginary offset well at each time step by applying the following equation,

$$\dot{\varepsilon} = \frac{\varepsilon^{n+1} - \varepsilon^{n}}{t^{n+1} - t^{n}} \tag{2.52}$$

where $\dot{\varepsilon}$ is strain rate, ε is strain, t is time, and n represents the time index.

A single fracture case study will first present to illustrate the calculation of strain rate based on rock deformation and strain rate based on fiber-optic measurement. In Fig. 2.29, a single fracture propagates to the offset well during hydraulic fracturing in the domain. The simulation domain is 400 ft by 1500 ft. The distance between the fractured well and imaginary well is 600 ft. The rest of the input used in simulation is listed in Table 2.3.

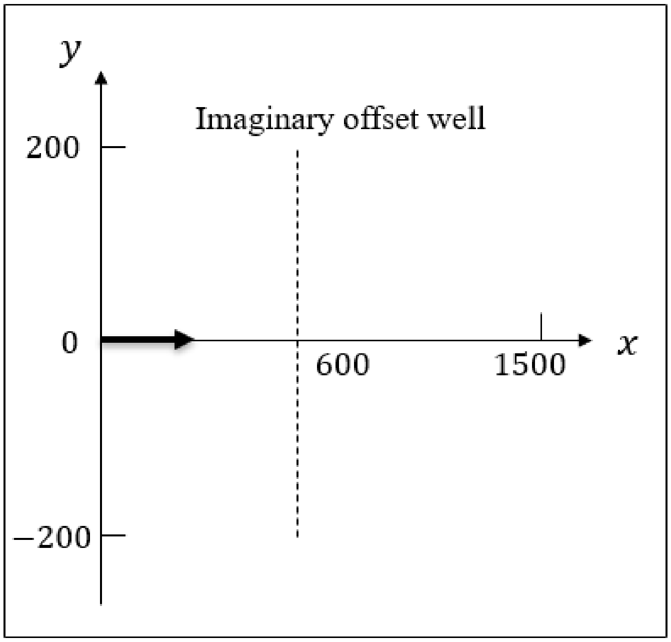

Fig. 2.29 The stimulation space domain for the single fracture case study

Table 2.3 Input data for strain rate simulation of the single fracture case

Parameter	Value
Young’s modulus, psi	4350000
Poisson’s ratio, /	0.2
Injection rate per one wing, bbl/min	20
Fluid viscosity, cp	5
Fracture height, ft	200
Injection time, min	60
Leak-off coefficient, $\mathrm{ft/min}^{0.5}$	0.001
Domain dimension, ft	400×1500
Well spacing, ft	600
Gauge length, m	2

We first calculate fracture half-length and net pressure evolution over time by using Equation 2.45 and Equation 2.46. The calculation results show in Fig. 2.30 and Fig. 2.31. Then, the fracture width distribution over time can be calculated by Equation 2.30.

Afterward, putting all these data into the strain rate calculation model, strain rate map based on rock deformation, and strain rate map based on displacement can be generated.

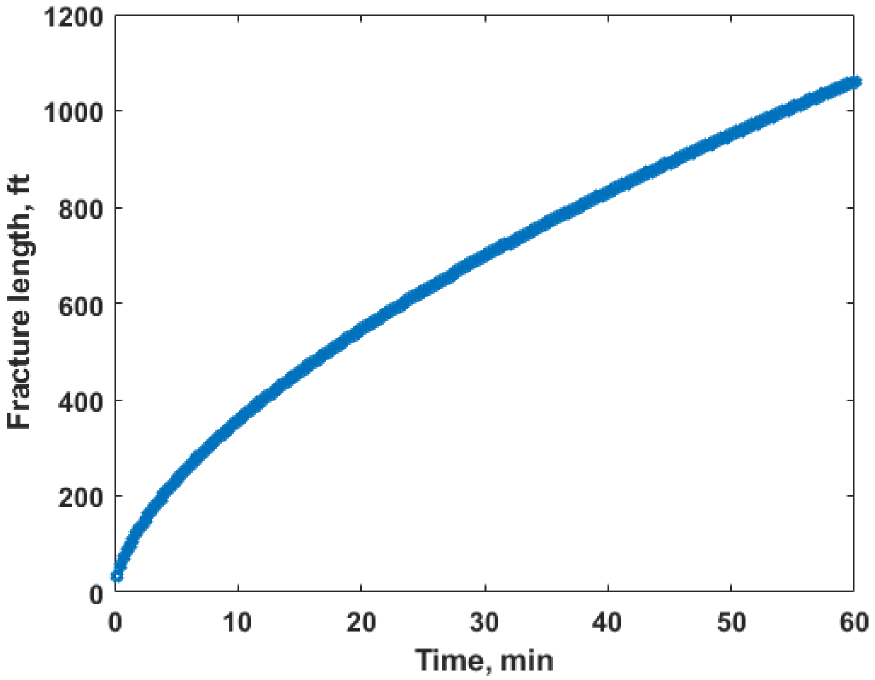

Fig. 2.30 Fracture half-length evolution over time of the single fracture case

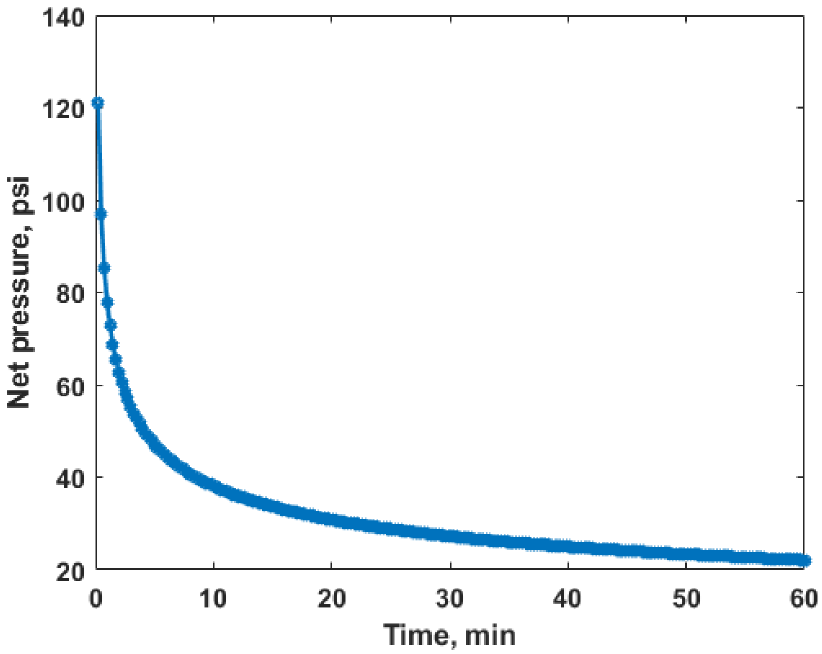

Fig. 2.31 Net pressure evolution over time of the single fracture case

2.5.1 Strain Rate Calculation Based on Rock Deformation

In order to understand the strain rate calculation based on rock deformation, we simulated stress distribution at the fracture location ($y = 0$), and the results are shown in Fig. 2.32.

Fig. 2.32(a) shows when the fracture starts to propagate from the treated well to the offset well, but still far away from the offset well. This is when fracture propagates 3.9 min, and the fracture length is 200 ft. Fig. 2.32(b) shows that the fracture is approaching the offset well, when fracture propagates 17.4 min, and the fracture length is 500 ft. Fig. 2.32(c) shows when fracture actually arrives at the offset well. This is when fracture propagates 23.4 min, and the fracture length is 600 ft, which equals the well spacing. Fig. 2.32(d) shows when the fracture has intercepted the offset and passes through it. This is when fracture propagates 55.4 min, and the fracture length was 1000 ft. Fig. 2.33 displays the stresses along the imaginary well as a function of time.

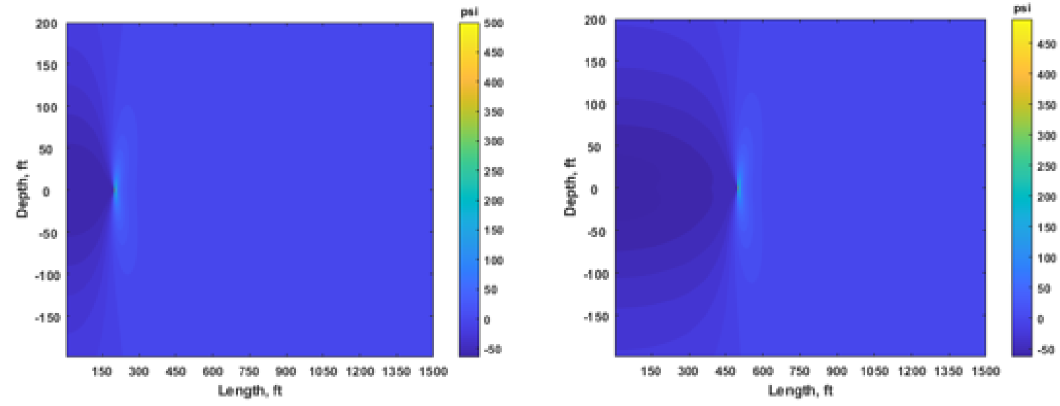

(a) $x_f = 200\ ft, t = 3.9\ min$ (b) $x_f = 500\ ft, t = 17.4\ min$

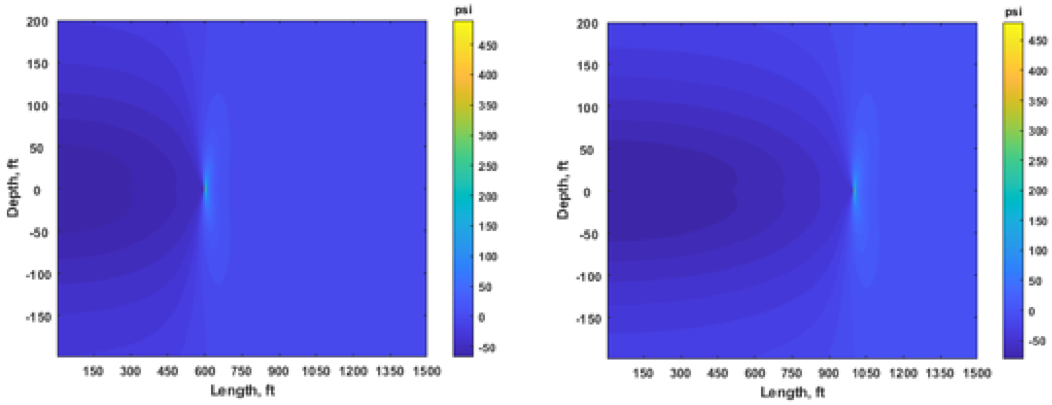

(c) $x_f = 600\ ft, t = 23.4\ min$ (d) $x_f = 1000\ ft, t = 55.4\ min$

Fig. 2.32 Stress domain at different time step with different fracture half-length

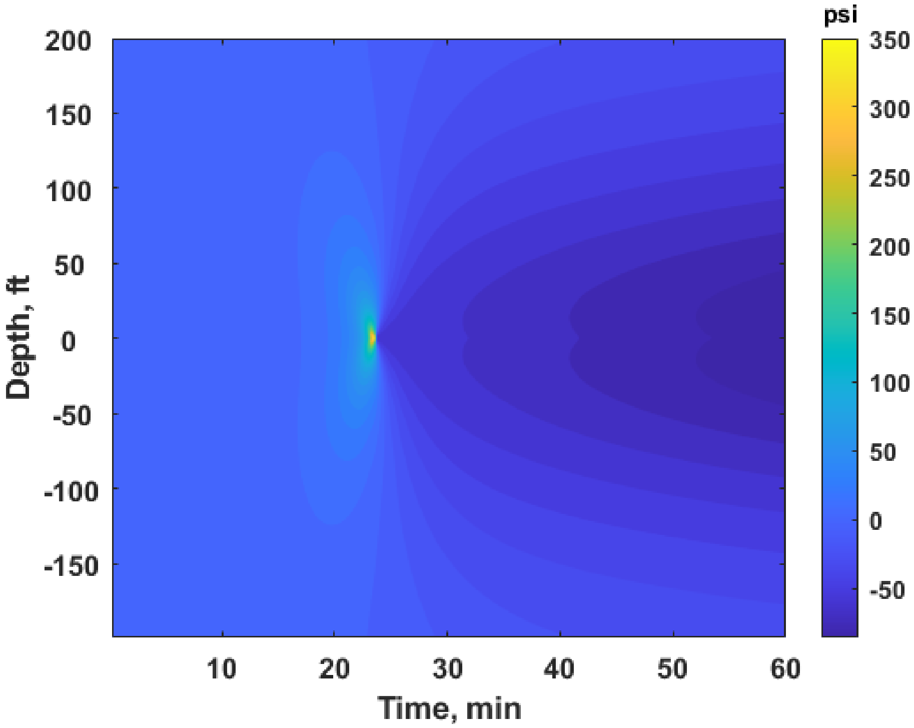

Fig. 2.33 Stress evolution at fiber location over time

After obtaining the stress information, we can convert the stress to strain by using Equation 2.50. We will show the progress of strain changes as fracture develops. Same as the stress investigation, we use the fracture location at different time steps with different fracture lengths, as shown in Fig. 2.34.

Fig. 2.34(a) shows the strain distribution at 3.9 min, and the fracture length is 200 ft. This is at the beginning of the treatment. Fig. 2.34(b) shows when the fracture is getting close to the offset well. This is when fracture propagates 17.4 min, and the fracture length was 500 ft. Fig. 2.34(c) shows at 23.4 min, the fracture intercepts the offset well where strain is measured and the fracture length was 600 ft. Fig. 2.34(d) shows at 55.4 min, the fracture has passed the offset well and the fracture length was 1000 ft.

Fig. 2.35 is the recording of the strain along the imaginary well as a function of time based on rock deformation.

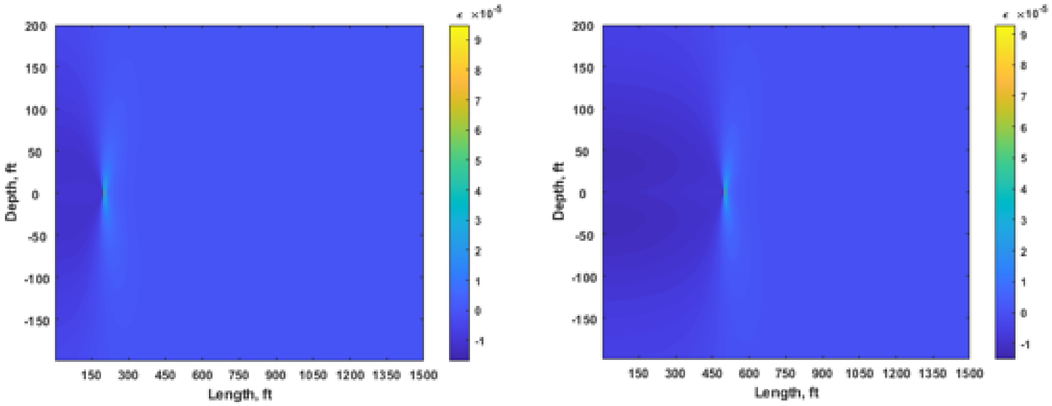

(a) $x_f = 200\ ft, t = 3.9\ min$ (b) $x_f = 500\ ft, t = 17.4\ min$

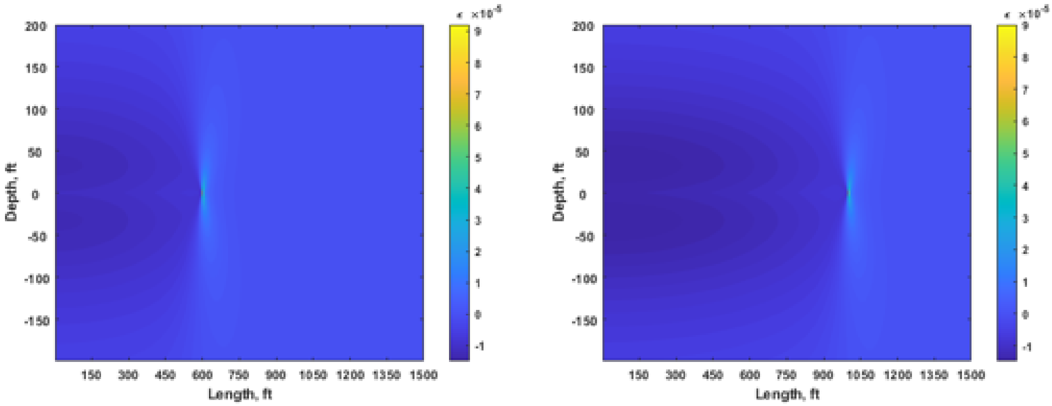

(c) $x_f = 600\ ft, t = 23.4\ min$ (d) $x_f = 1000\ ft, t = 55.4\ min$

Fig. 2.34 Strain domain based on rock deformation at different time step with different fracture half-length

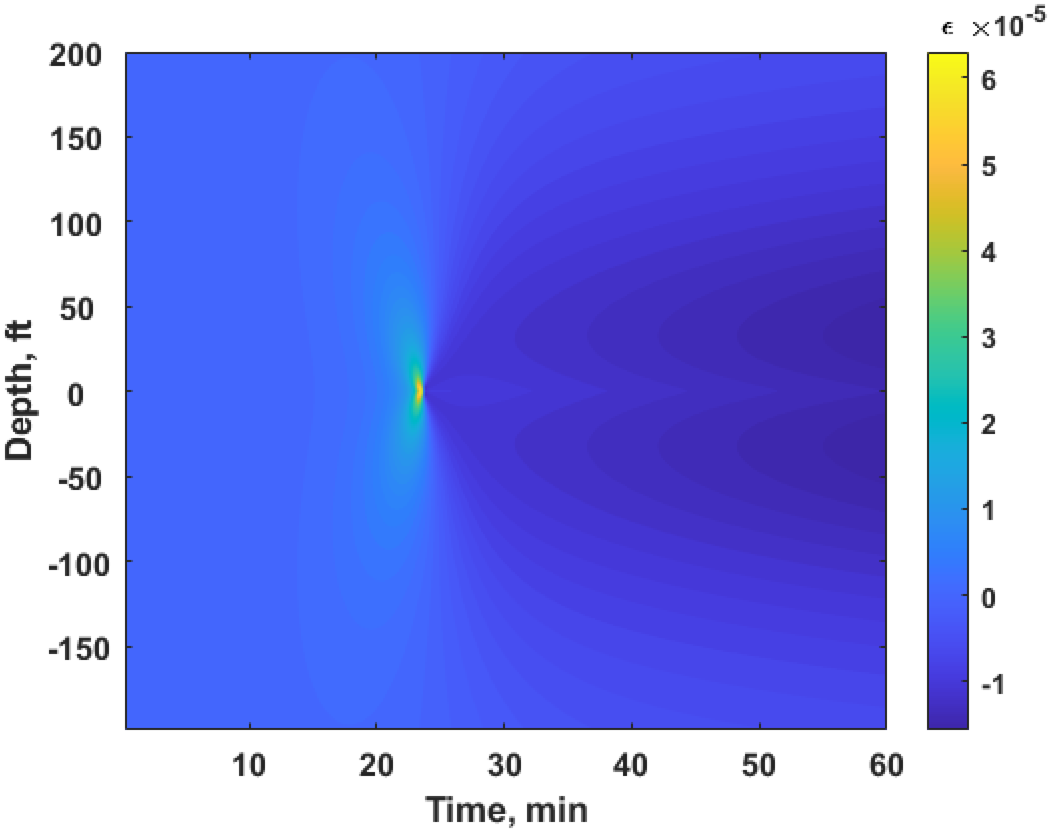

Fig. 2.35 Strain evolution based on rock deformation at fiber location over time

After simulating the strain distribution based on rock deformation along the imaginary well over time, we can calculate strain rate over time by using Equation 2.52. The calculation result is shown in Fig. 2.36 based on Fig. 2.35.

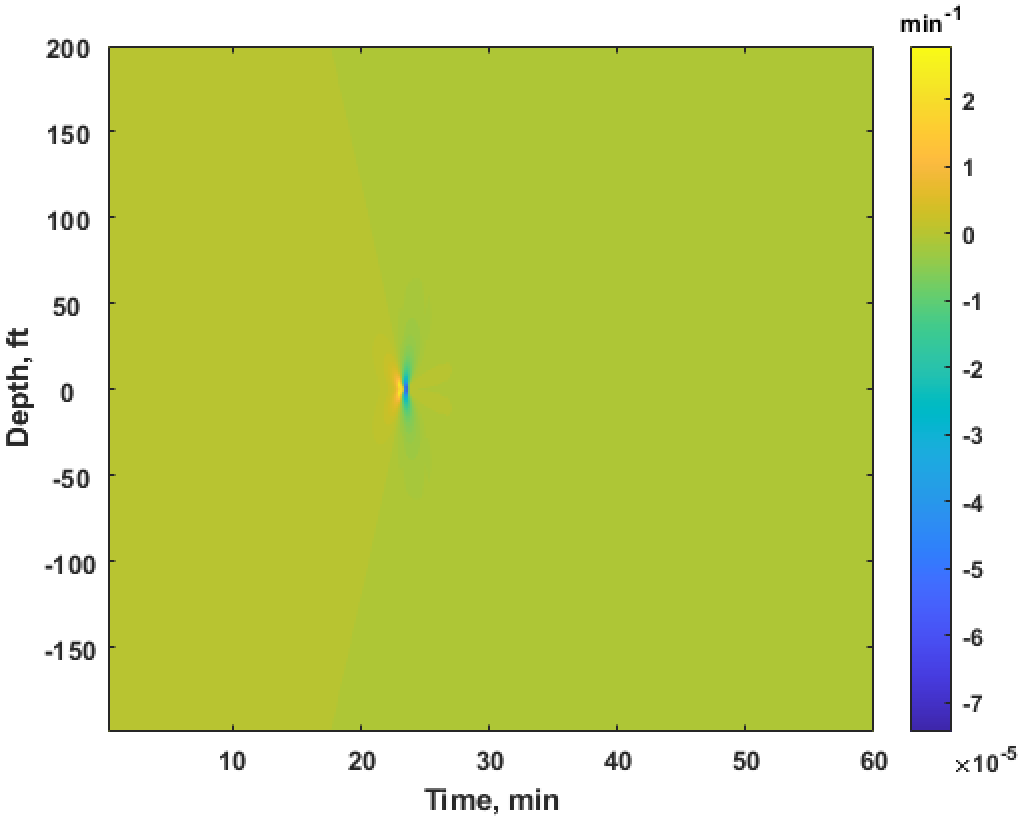

Fig. 2.36 Strain rate evolution based on rock deformation at fiber location over time

2.5.2 Strain Rate Calculation Based on Fiber-Optic Measurement

As introduced before, strain based on rock deformation is different from strain based on fiber-optic measurement. Therefore, the strain rate results of the counterpart should be different as well. Strain rate calculation based on fiber-optic measurement is derived from displacements. We investigate the strain rate based on fiber-optic measurement by demonstrating the displacement distribution change as a function of time. Fig. 2.37 shows the displacement behavior at the fracture location at four different times. These times are selected based on fracture half-length change.

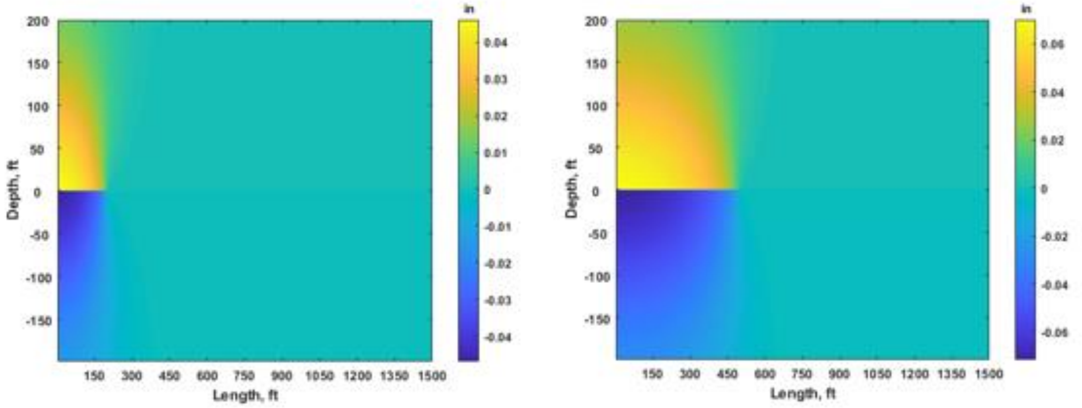

(a) $x_f = 200\, m, t = 3.9\, min$ (b) $x_f = 500\, m, t = 17.4\, min$

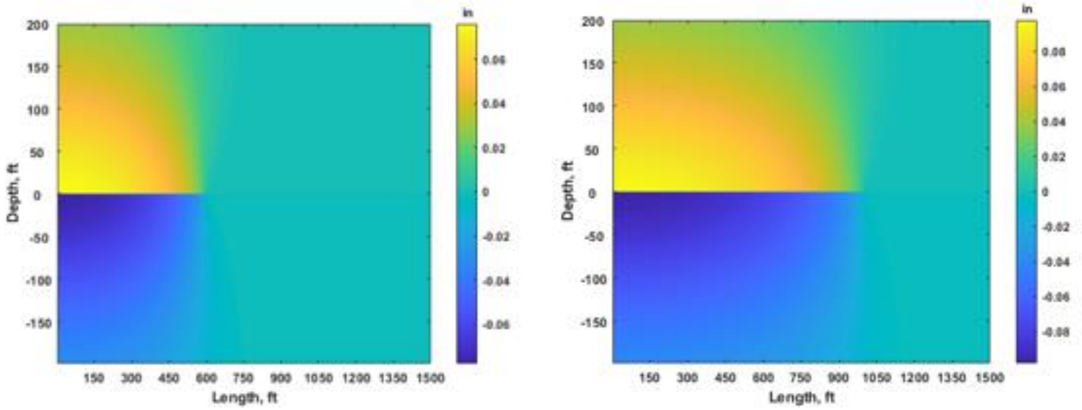

(c) $x_f = 600\, m, t = 23.4\, min$ (d) $x_f = 1000\, m, t = 55.4\, min$

Fig. 2.37 Displacement domain at different time step with different fracture half-length

Fig. 2.37(a) shows when initial stage of fracture propagation from the treated well to the offset well. The fracture tip is still far away from the offset well. At 3.9 min, the fracture length was 200 ft. Fig. 2.37(b) shows when the fracture is approaching close to the offset well. This is when fracture propagated 17.4 min, and the fracture length was 500 ft. Fig. 2.37(c) shows when fracture actually arrived at the offset well. This is when fracture propagated 23.4 min, and the fracture length was 600 ft which equals the well spacing. Fig. 2.37(d) shows when the fracture has already intercepted the offset and passed through it. This is when fracture propagated 55.4 min, and the fracture length was 1000 ft. Fig. 2.38 displays the displacements along the imaginary well as a function of time.

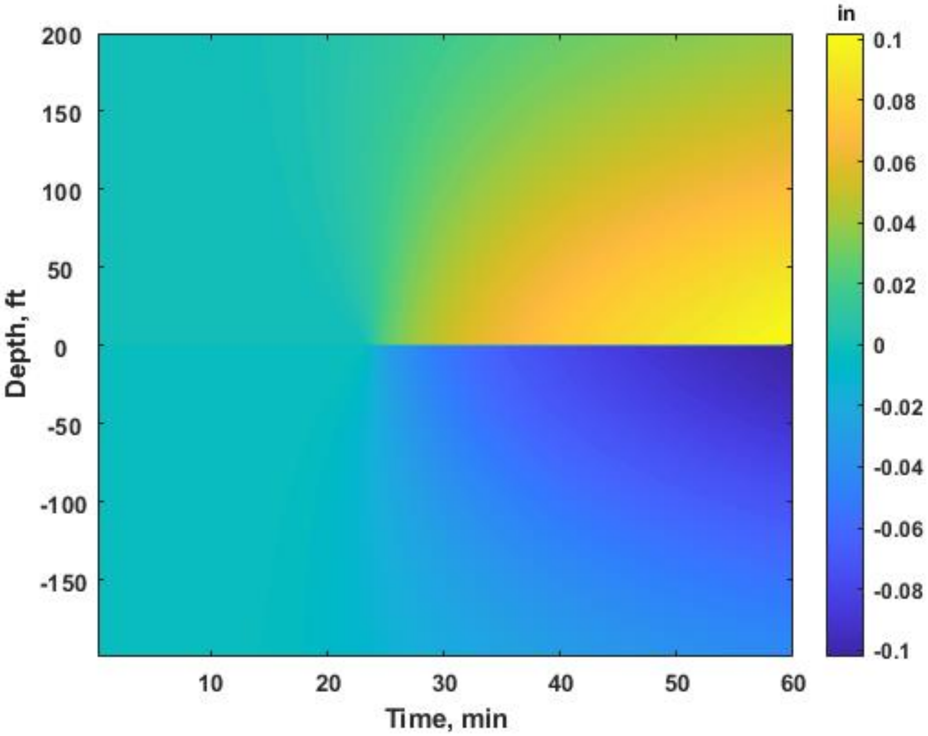

Fig. 2.38 Displacement evolution at fiber location over time

After getting the dispalcement, we transform the displacement to strain based on fiber-optic measurement by using Equation 2.51. In order to show the full progress of how the strain domain change during the hydraulic fracturing. Four strain domains based on different time step with different fracture length are shown in Fig. 2.39.

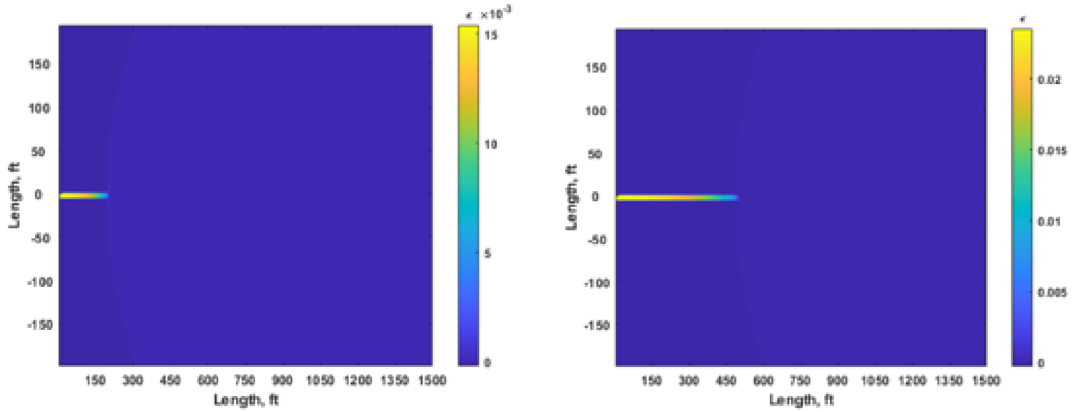

(a) $x_f = 200\ m, t = 3.9\ min$ (b) $x_f = 500\ m, t = 17.4\ min$

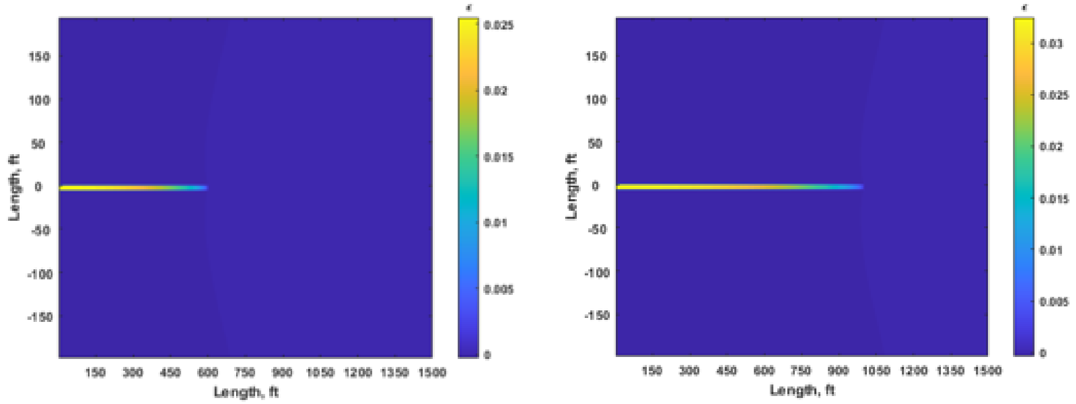

(c) $x_f = 600\ m, t = 23.4\ min$ (d) $x_f = 1000\ m, t = 55.4\ min$

Fig. 2.39 Strain domain based on fiber-optic measurement at different time step

Fig. 2.39(a) shows the strain distribution at 3.9 min, and the fracture length was 200 ft. This is at the beginning of the treatment. A “yellow strip” can be found at the fracture location, and other area in the domain show strain close to zero. This is because fiber measures the extension at fractue location, and nearly zero strain at other locations. Fig. 2.39(b) shows when the fracture is getting close to the offset well. This is when fracture propagates 17.4 min, and the fracture length was 500 ft. With the fracture growth, the "yellow strip" extends and becomes longer. Fig. 2.39(c) shows at 23.4 min, the fracture intercepts the offset well where strain is measured and the fracture length was 600 ft. At last, Fig. 2.39(d) shows at 55.4 min, the fracture has passed the offset well and the fracture length was 1000 ft. During the whole process, we can only see the lengthening of the "yellow strip", which is the extension at the fracture location, the other area keeps strain close to zero all the time.

Fig. 2.40 is the recording of the strain along the imaginary well as a function of time based on fiber-optic measurement. Then we transform the strain to the strain rate over time by using Equation 2.52. The calculation result is shown in Fig. 2.41 based on Fig. 2.40.

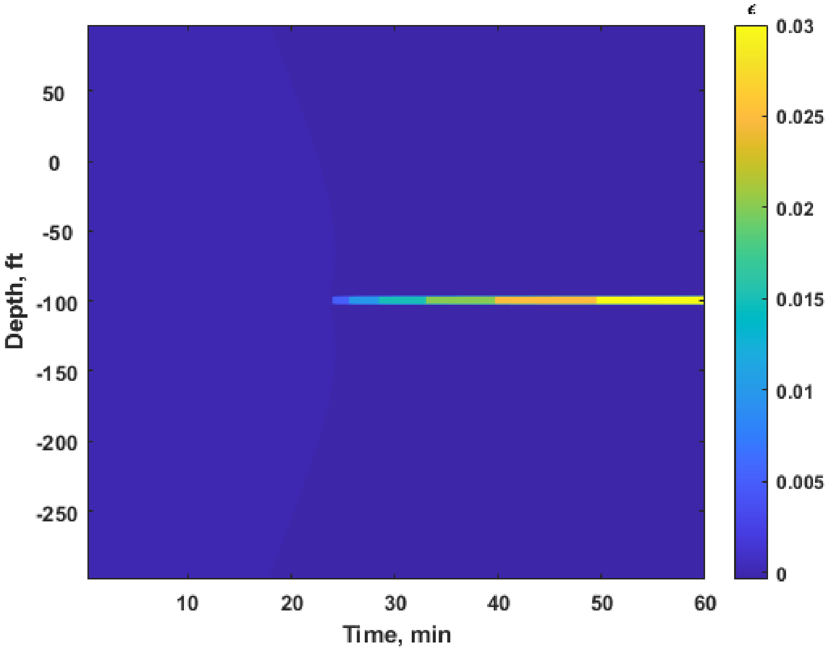

Fig. 2.40 Strain evolution based on fiber-optic measurement at fiber location over time

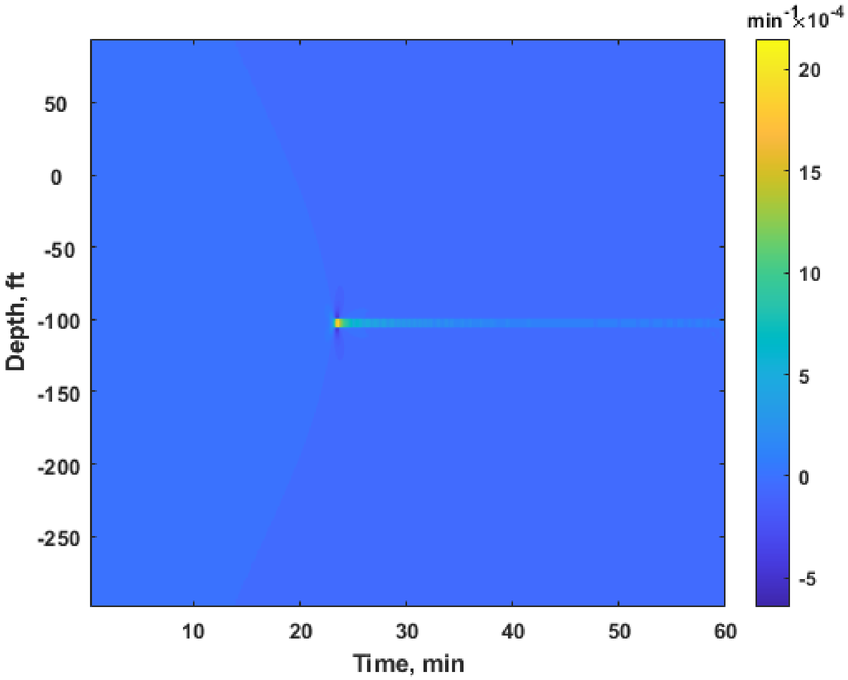

Fig. 2.41 Strain rate evolution based on fiber-optic measurement at fiber location over time

3 MODEL DEVELOPMENT OF MULTIPLE FRACTURE

3.1 Introduction

For multiple fracture scenarios, we assume fractures propagation independently and are not affected by stress interference between them. The net pressures in the fractures are equal and constant. Each fracture is simulated separately by using the KGD model with fixed injection rate and time.

The KGD model has been derived in Chapter 2. The flowchart of modeling multiple fracture scenarios is shown in Fig. 3.1. Similar to the single fracture workflow, after reading the input data, the fracture lengths of each one of the fractures are calculated by KGD model independently at a single time step by solving Equation 2.45. Then the fracture width distribution along the fracture of each one of the fractures will be calculated by using Equation 2.30. After that, we use DDM to simulate stresses and displacements along the fiber location, and they will be used to calculate the far-field strain by applying Equation 2.50 (rock deformation) or Equation 2.51 (fiber-optic measurement). At each time step, we document the far-field strain along the fiber. This procedure will be performed at each time step, until the stimulation is completed. Then we will calculate the strain rate by taking the derivative of the two adjacent time steps by applying Equation 2.52. In the end, pattern generation will be performed to the strain rate data by applying Equation 4.1.

The objective of this chapter is to use a computationally efficient method to generate hypothetical multiple fracture geometries and demonstrate the far-field strain rate responses if the proposed hypothetical cases really happened.

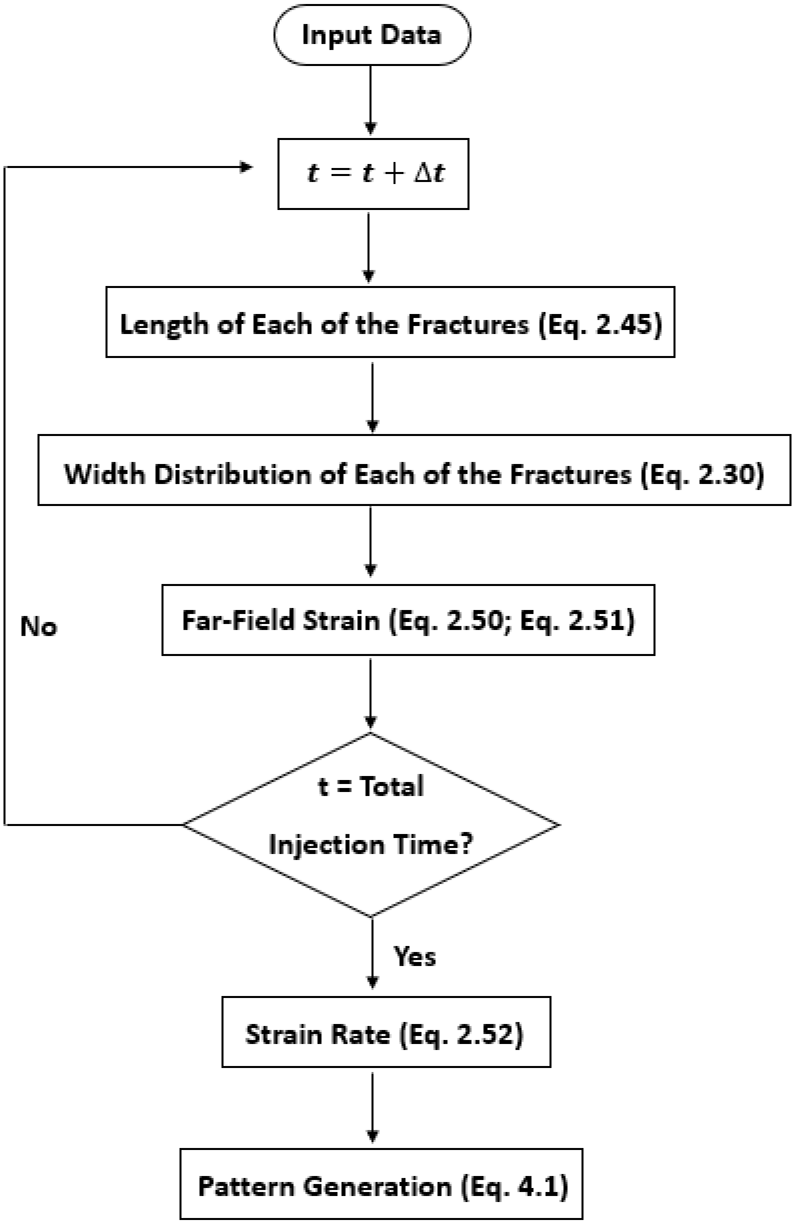

Fig. 3.1 Flowchart of the multiple fracture model

3.2 Space Domain Calculation

3.2.1 Stress and Displacement Domain Calculation

An example is shown in Fig. 3.2 of three synthetic fractures located in the space domain. All fractures are discretized in multiple elements. On each element, there is a displacement discontinuity. Since all the displacement discontinuities will be considered into the calculation of stress and displacement later, thus, we name them from d_1 to d_{12}. The other input data are listed in Table 3.1.

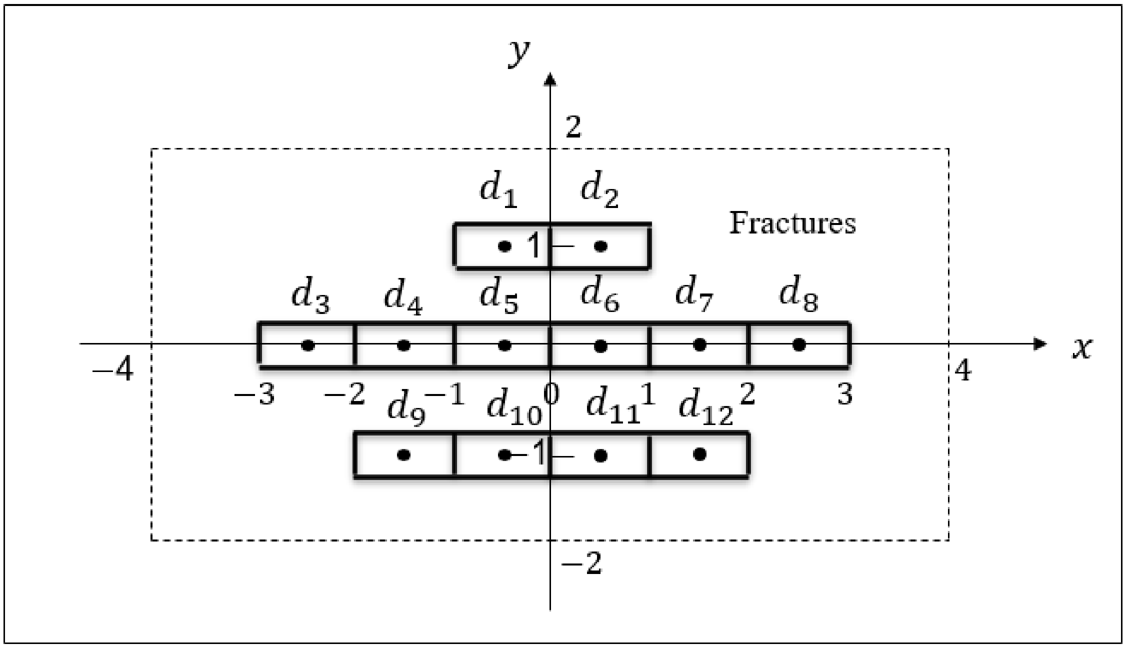

Fig. 3.2 Illustration of the synthetic multiple fracture in space domain

Table 3.1 Input data for the synthetic multiple fracture space domain calculation

Parameter	Value
Fracture half-length @ +1 ft, ft	1
Fracture half-length @ 0 ft, ft	3
Fracture half-length @ -1 ft, ft	2
Fracture height, ft	100
Young’s modulus, psi	4350000
Poisson’s ratio, /	0.2
Net pressure, psi	145

Following the flowchart of the multiple fracture scenario, like solving the single fracture scenario, we use Equation 2.30 to calculate the fracture width distribution (ft) of all fractures separately. The calculation results are showing below,

$$\begin{bmatrix} d_1 \\ d_2 \\ d_3 \\ d_4 \\ d_5 \\ d_6 \\ d_7 \\ d_8 \\ d_9 \\ d_{10} \\ d_{11} \\ d_{12} \end{bmatrix} = \begin{bmatrix} 0.000110851251684408 \\ 0.000110851251684408 \\ 0.000212263986582746 \\ 0.000332553755053224 \\ 0.000378629106118375 \\ 0.000378629106118375 \\ 0.000332553755053224 \\ 0.000212263986582746 \\ 0.000169328083908134 \\ 0.000247870934157275 \\ 0.000247870934157275 \\ 0.000169328083908134 \end{bmatrix} \tag{3.1}$$

After obtaining the fracture distribution, by applying Equation 2.25 to Equation 2.27, the stress (psi) and displacement (in) domain can be calculated,

$$\sigma_{yy} = \begin{bmatrix} 64.7 & 20.7 & -59.1 & -176.9 & -176.9 & -59.1 & 20.7 & 64.7 \\ 125.0 & 76.0 & -78.8 & -232.0 & -232.0 & -78.8 & 76.0 & 125.0 \\ 124.3 & 103.0 & -82.7 & -256.0 & -256.0 & -82.7 & 103.0 & 124.3 \\ 77.0 & 63.3 & -66.4 & -220.3 & -220.3 & -66.4 & 63.3 & 77.0 \end{bmatrix}$$

………………………………………………………………………………………… (3.2)

$$u_y = 10^{-4} \cdot \begin{bmatrix} -5.9 & -11.0 & -17.8 & -24.9 & -24.9 & -17.8 & -11.0 & -5.9 \\ -2.3 & -9.1 & -20.1 & -25.0 & -25.0 & -20.1 & -9.1 & -2.3 \\ 1.4 & 6.9 & 11.0 & 10.2 & 10.2 & 11.0 & 6.9 & 1.4 \\ 4.9 & 9.8 & 18.7 & 27.6 & 27.6 & 18.7 & 9.8 & 4.9 \end{bmatrix}$$

………………………………………………………………………………………… (3.3)

and the stress domain can be plotted in the waterfall as shown in Fig. 3.3, and the displacement domain can be plotted in the waterfall as shown in Fig. 3.4.

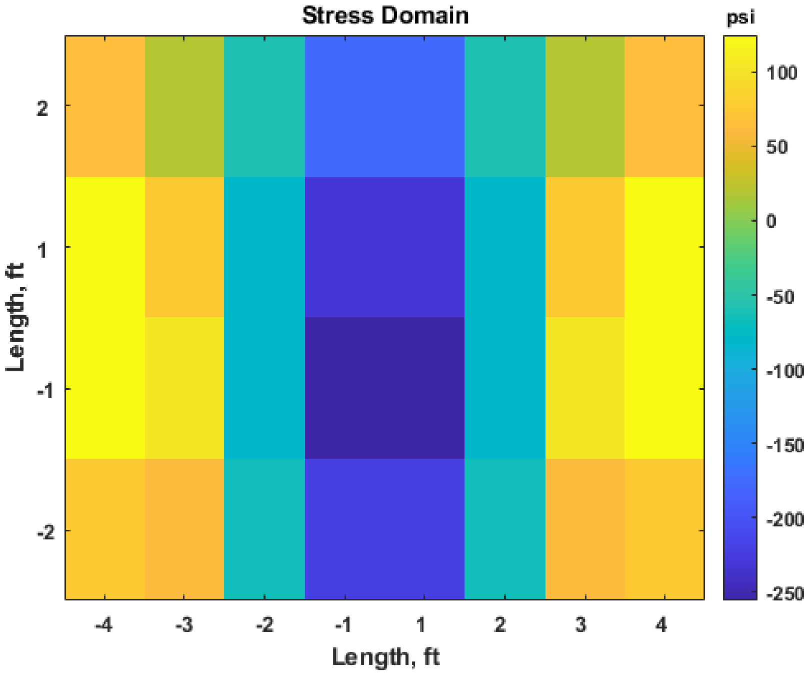

Fig. 3.3 Illustration of the stress domain of the synthetic multiple fracture

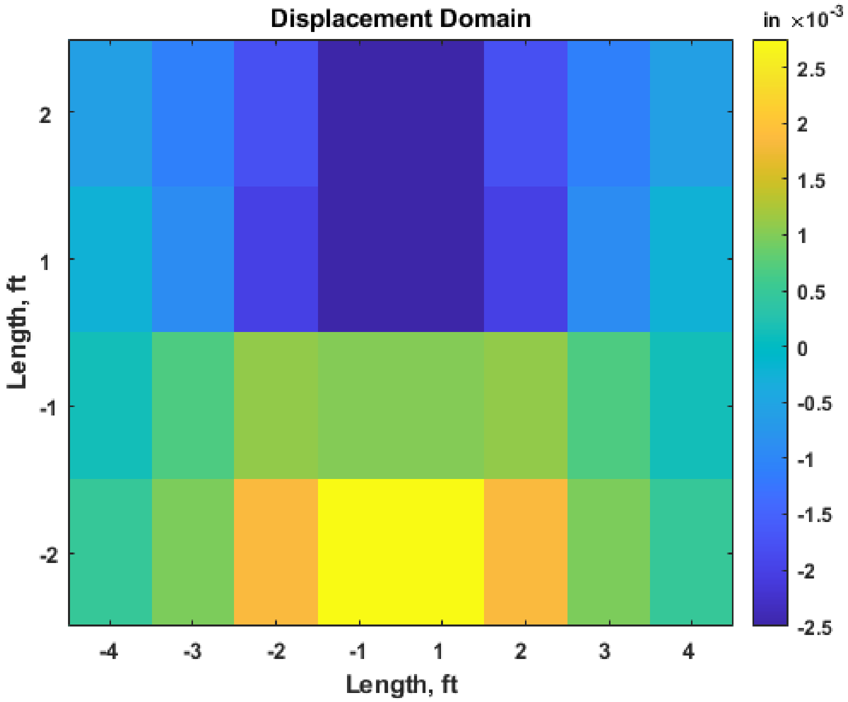

Fig. 3.4 Illustration of the displacement domain of the synthetic multiple fracture

A field-size example of multiple fracture scenario is shown in Fig. 3.5. Five synthetic fractures are located in the space domain. The dashed lines at 100 ft, 200 ft and 400 ft are the observation location lines. The 100 ft line locates behind all fracture tips. The 200 ft line locates on one fracture tip, beyond one fracture tip and behind three fracture tips. The 400 ft line locates beyond all the tips of the fractures. The stress and displacement details along these lines are further investigated for stress and displacement as we did the same to the single fracture case. The input data are listed in Table 3.2.

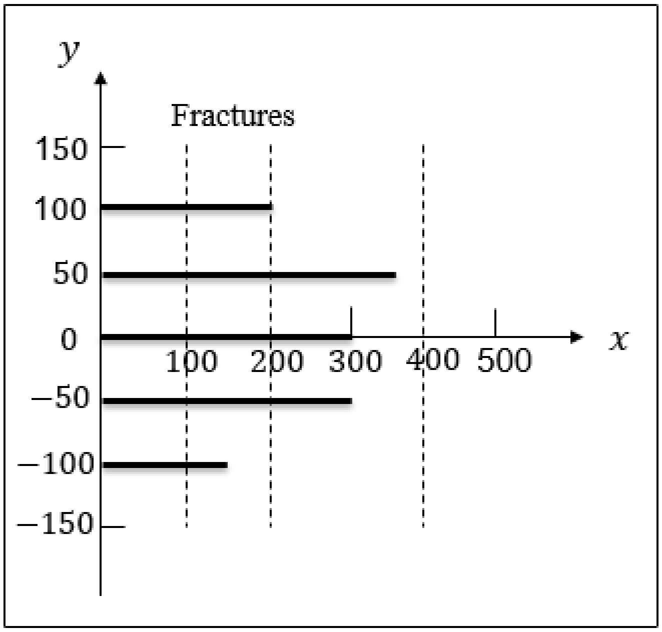

Fig. 3.5 Illustration of the multiple fracture in the space domain

Table 3.2 Input data for the multiple fracture space domain calculation

Parameter	Value
Fracture half-length @ +100 ft, ft	200
Fracture half-length @ +50 ft, ft	350
Fracture half-length @ 0 ft, ft	300
Fracture half-length @ -50 ft, ft	300
Fracture half-length @ -100 ft, ft	150
Fracture height, ft	100
Young’s modulus, psi	4350000
Poisson’s ratio, /	0.2
Net pressure, psi	145

Following the workflow of multiple fracture scenario, the stress domain can be generated. The stress domain calculation result is shown in Fig. 3.6. The stress along dashed lines at 100 ft, 200 ft, and 400 ft is calculated and shown in Fig. 3.7, Fig. 3.8, and Fig 3.9.

As we can see in Fig. 3.6, for each fracture, the stress at sides of the fracture shows compression (negative number). Meanwhile, the stress in front of the fracture shows extension (positive number). Each stress point in the domain is the total combination of the effects by five fractures. Because of the five fracture lengths are not equal, therefore, the stresses along the dashed lines are not symmetric.

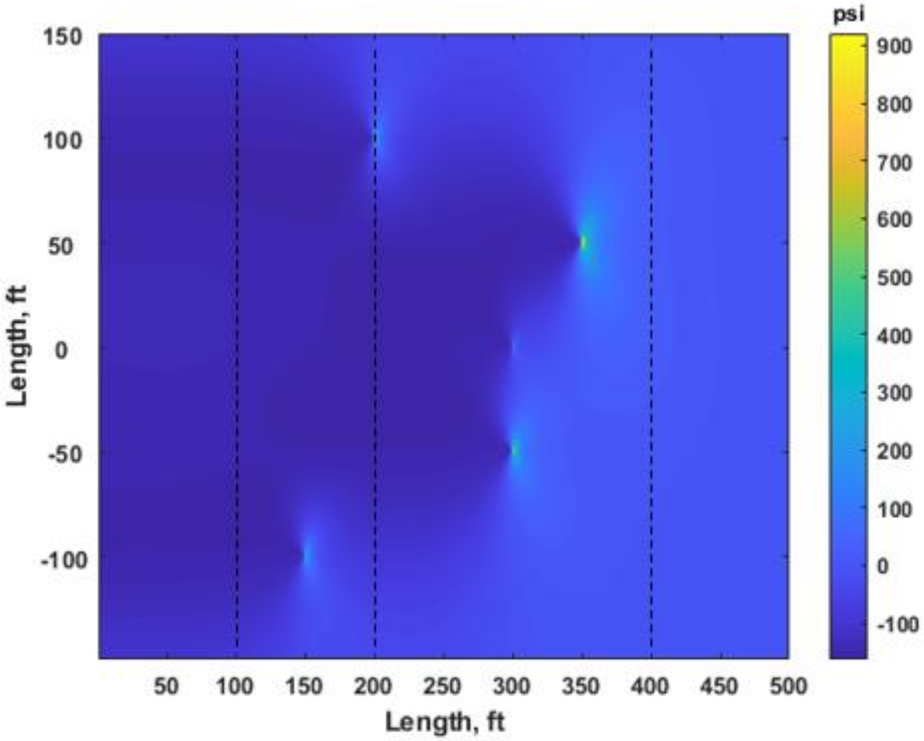

Fig. 3.6 Stress domain of the multiple fracture case

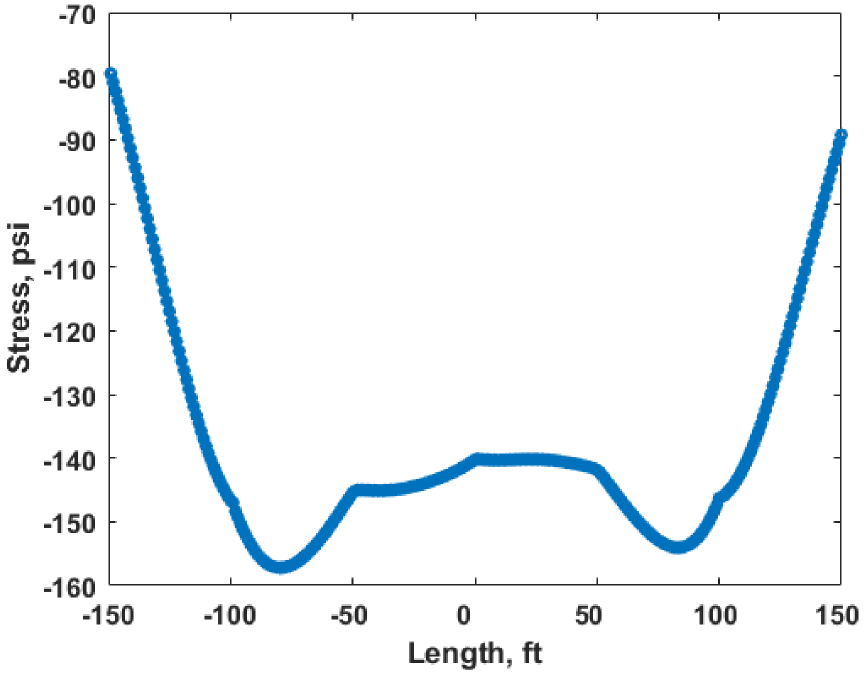

Fig. 3.7 Stress distribution along the 100 ft location of the multiple fracture case

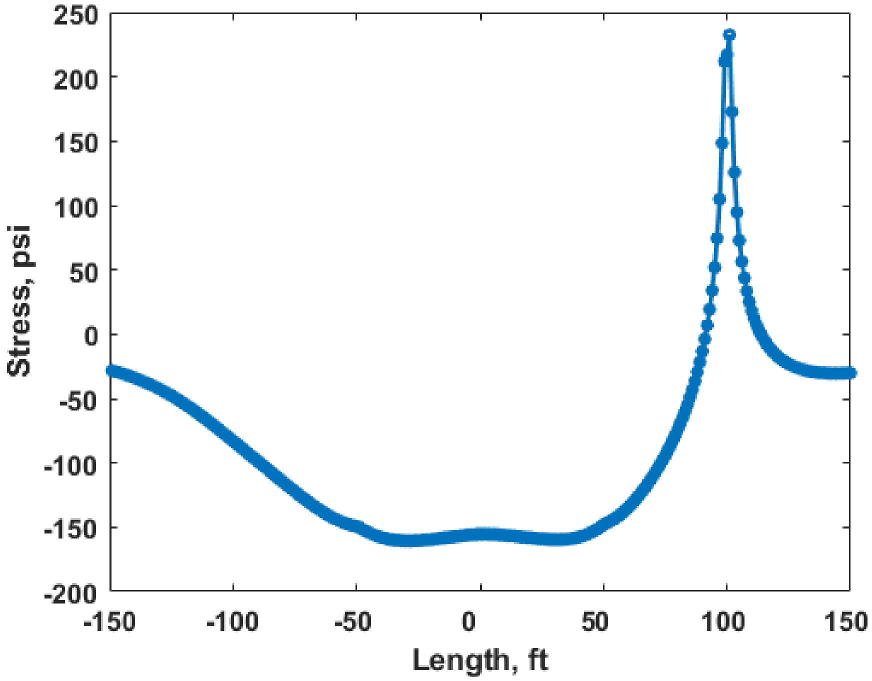

Fig. 3.8 Stress distribution along the 200 ft location of the multiple fracture case

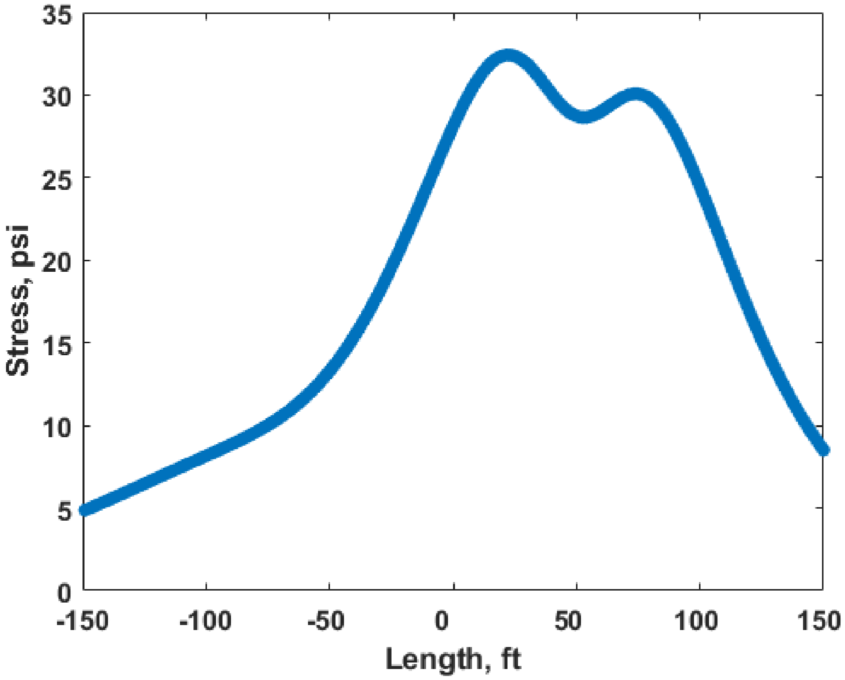

Fig. 3.9 Stress distribution along the 400 ft location of the multiple fracture case

After showing the simulation of the stress domain, the simulation of the displacement domain is performed. The displacement domain calculation result is shown in Fig. 3.10. The displacement along the three observation lines is shown in Fig. 3.11, Fig. 3.12, and Fig. 3.13.

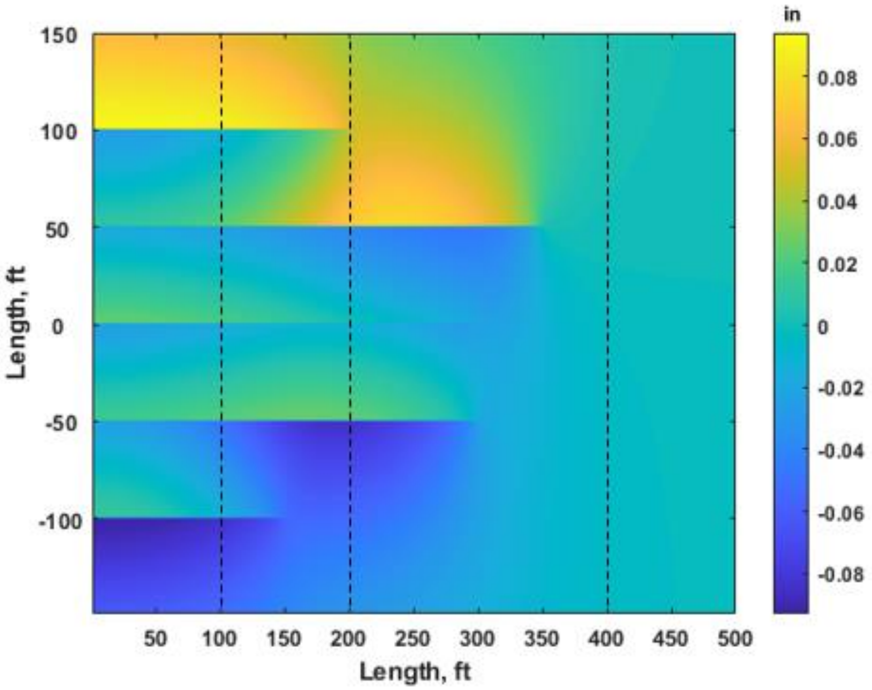

Fig. 3.10 Displacement domain of the multiple fracture case

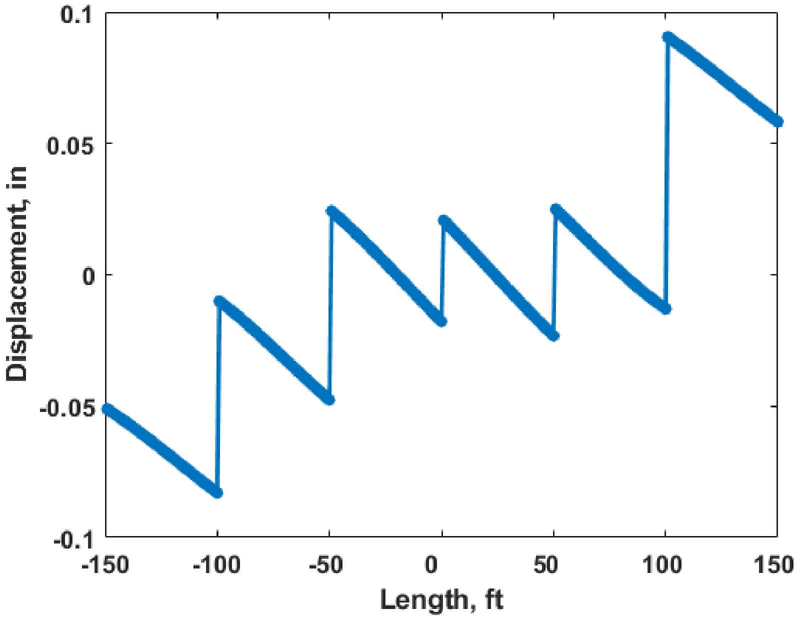

Fig. 3.11 Displacement distribution along the 100 ft location of the multiple fracture case

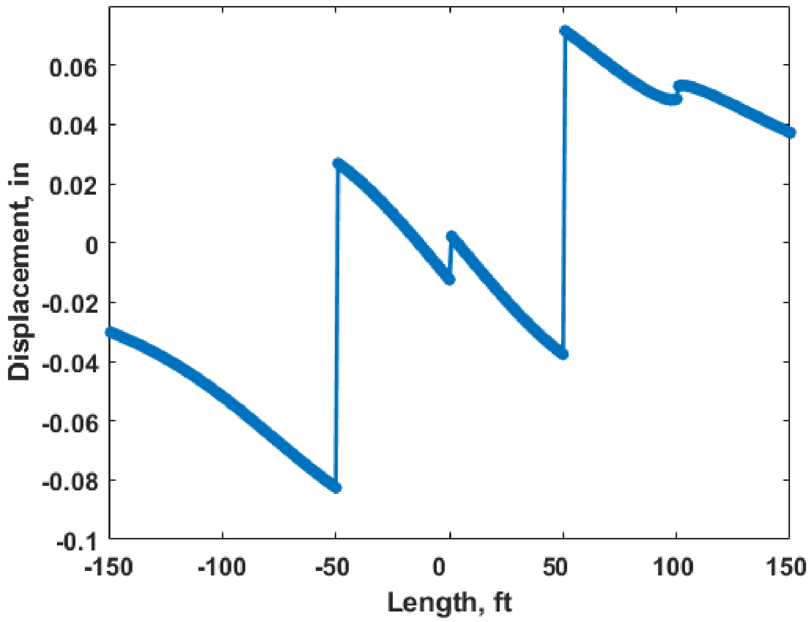

Fig. 3.12 Displacement distribution along the 200 ft location of the multiple fracture case

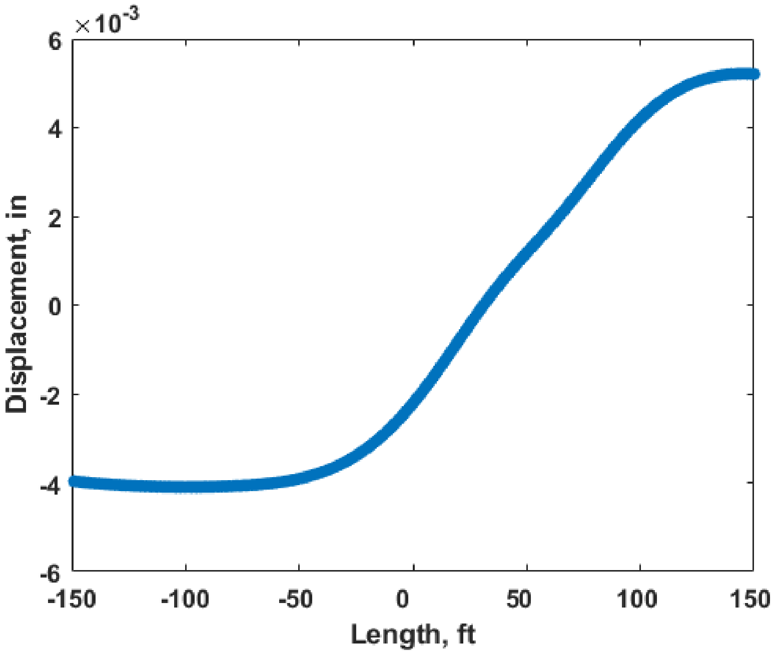

Fig. 3.13 Displacement distribution along the 400 ft location of the multiple fracture case

Fig. 3.10 shows the displacement domain of the five opened fractures. As discussed in single fracture scenario, the direction of the displacement at sides of each fracture is in the opposite direction against each other, and the magnitude of the displacement is symmetric. However, in the multiple fracture scenario, the displacement at each point in the domain is the combination of the influences of all fractures. Thus, in this case, we can see that the area near the middle fractures has less displacement than the area near the outside fractures, because the outside fractures squeeze the middle fractures so that some of the displacements are counteracted.

3.2.2 Strain Domain Calculation Based on Rock Deformation

After showing the simulation of stress domain, we illustrate the strain domain calculation based on rock deformation. As we did to single fracture scenario, the strain based on rock deformation can be calculated using Equation 2.50. The strain domain calculation result is shown in Fig. 3.14. The distribution of the strain will be investigated at 100 ft, 200 ft, and 400 ft locations as we did to stress domain. And the investigation results are shown in Fig. 3.15, Fig. 3.16, and Fig. 3.17.

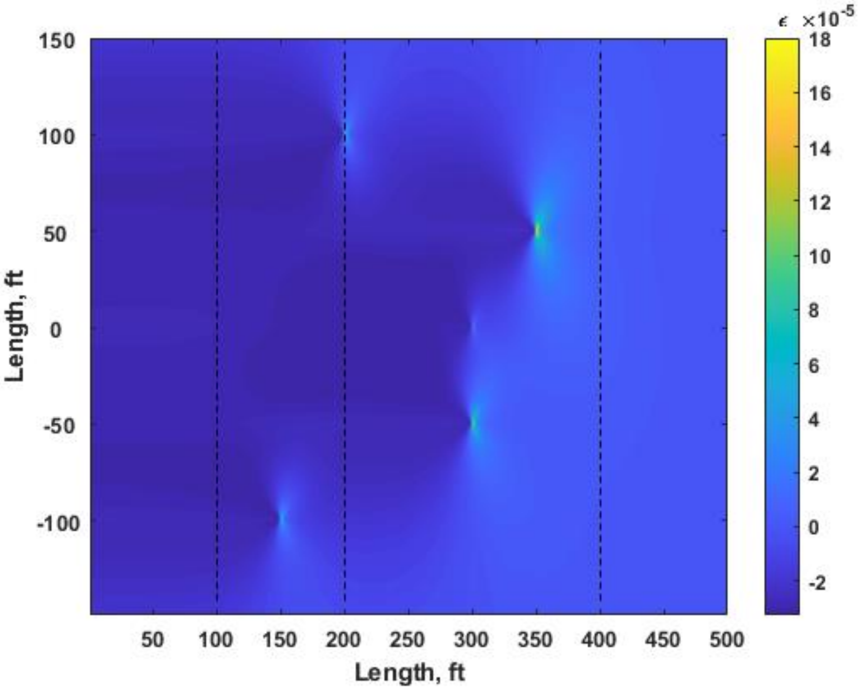

Fig. 3.14 Strain domain of the multiple fracture case based on rock deformation

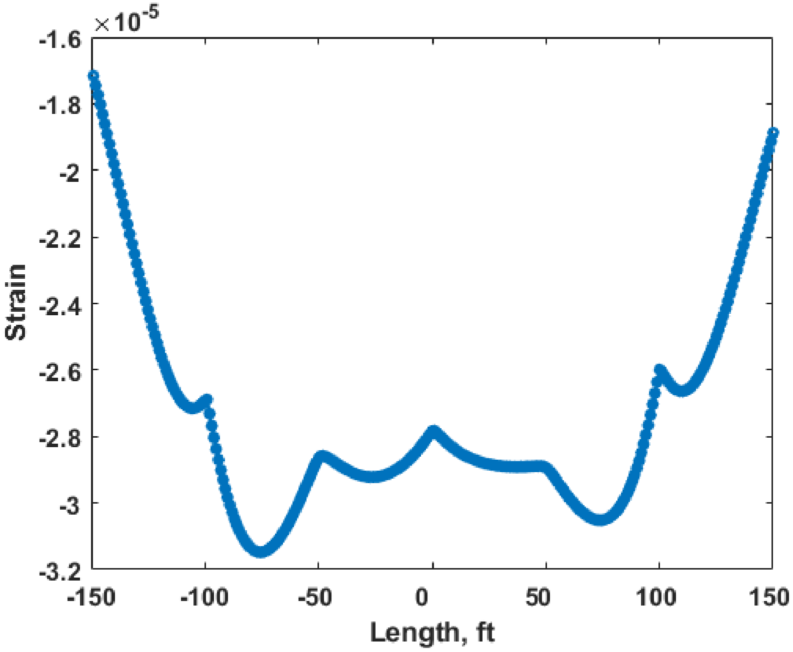

Fig. 3.15 Strain distribution based on rock deformation along the 100 ft location of the multiple fracture case

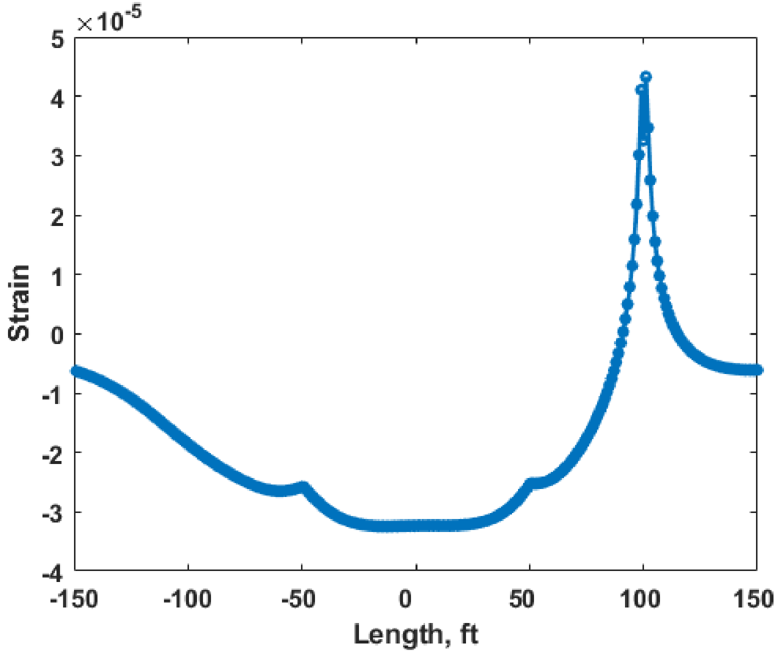

Fig. 3.16 Strain distribution based on rock deformation along the 200 ft location of the multiple fracture case

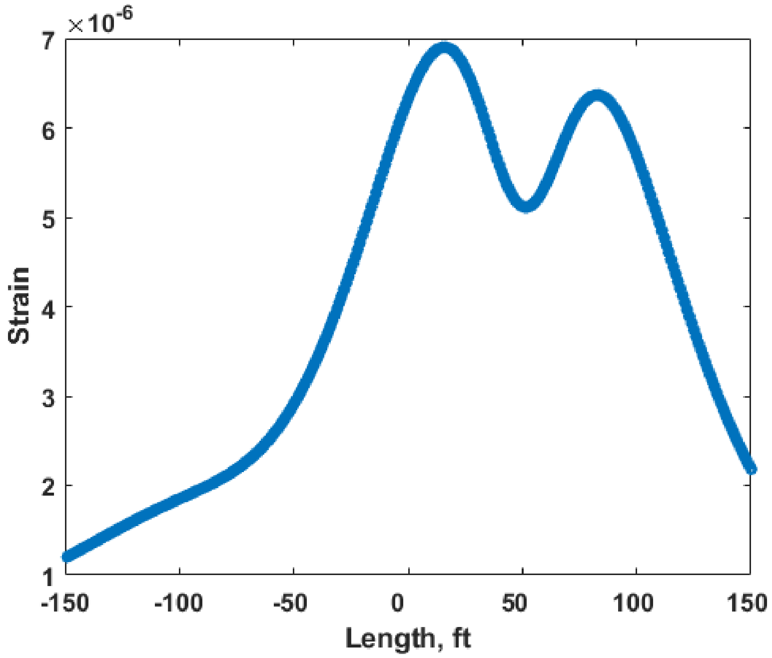

Fig. 3.17 Strain distribution based on rock deformation along the 400 ft location of the multiple fracture case

Similar as the stress domain, for each fracture, the strain at sides of the fracture shows compression (negative number), and the strain in front of the fracture shows extension (positive number). For each fracture, right at the fracture tip, there is the largest tensile strain. Each strain point in the domain is the total combination of the effects by five fractures. In this case, due to the lengths of the fractures are different, compressive strain on the sides of the longer fracture counteracts the tensile strain in front of the shorter fractures. Thus, the strain values along the dashed lines are not symmetric.

3.2.3 Strain Domain Calculation Based on Fiber-Optic Measurement

Same as we did to single fracture scenario, strain domain based on fiber-optic measurement simulation of multiple fracture can be simulated by applying Equation 2.51 to the multiple fracture displacement domain. The simulation result shows in Fig. 3.18. The distribution of the strain based on fiber-optic measurement will be investigated at the locates along the 100 ft, 200 ft, and 400 ft. The investigation results show in Fig. 3.19, Fig. 3.20, and Fig. 2.21.

The strain domain based on fiber-optic measurement of multiple fracture scenario has tensile zones (positive numbers) locate on the fractures, and in the front of tips of the fractures. And each tensile zone along the fractures appears a “strip” shape like the single fracture scenario. The compressive zone can hardly find in the strain domain based on fiber-optic measurement of multiple fracture scenario. The area between each of the fractures shows strain close to zero.

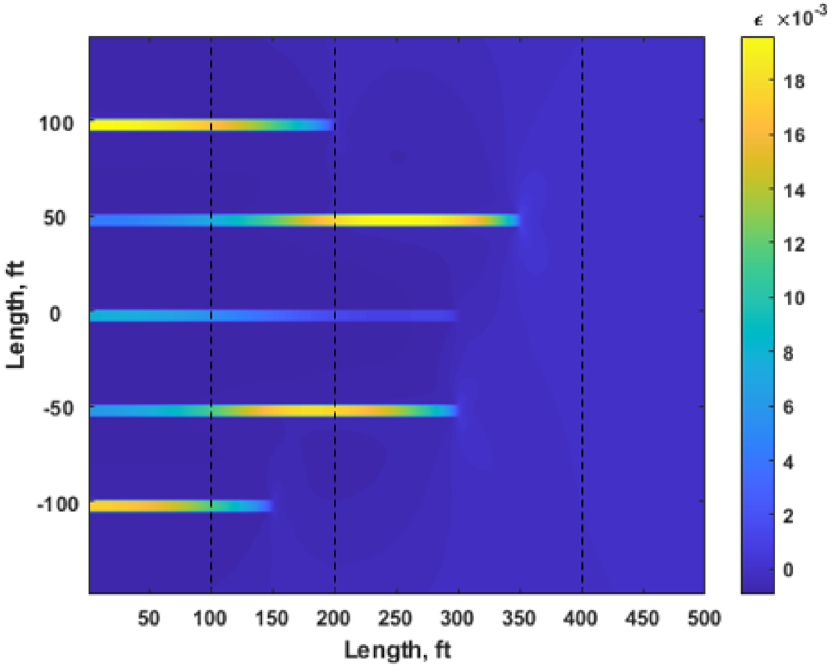

Fig. 3.18 Strain domain of the multiple fracture case based on fiber-optic measurement

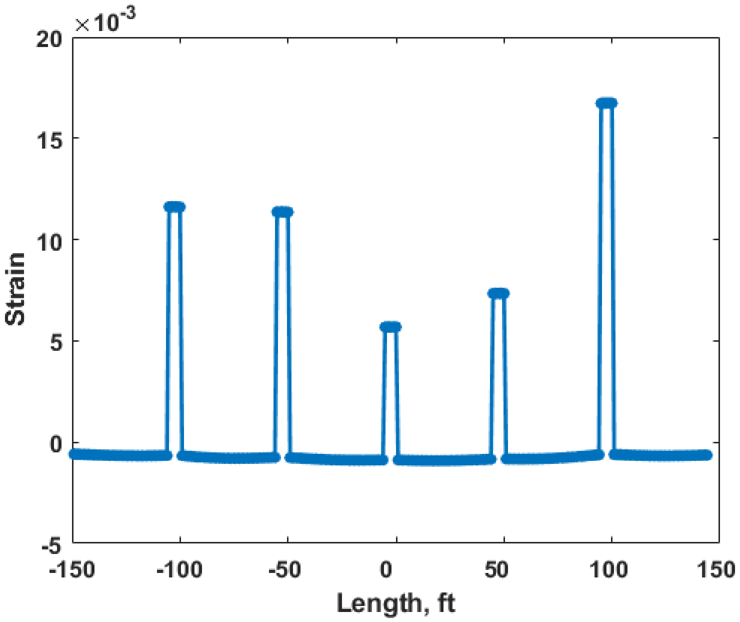

Fig. 3.19 Strain distribution based on fiber-optic measurement along the 100 ft location of the multiple fracture case

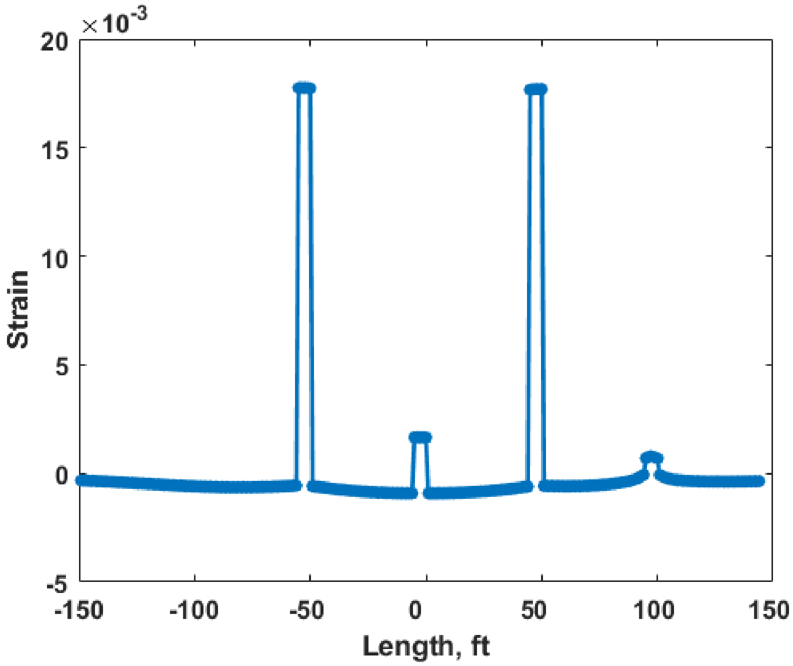

Fig. 3.20 Strain distribution based on fiber-optic measurement along the 200 ft location of the multiple fracture case

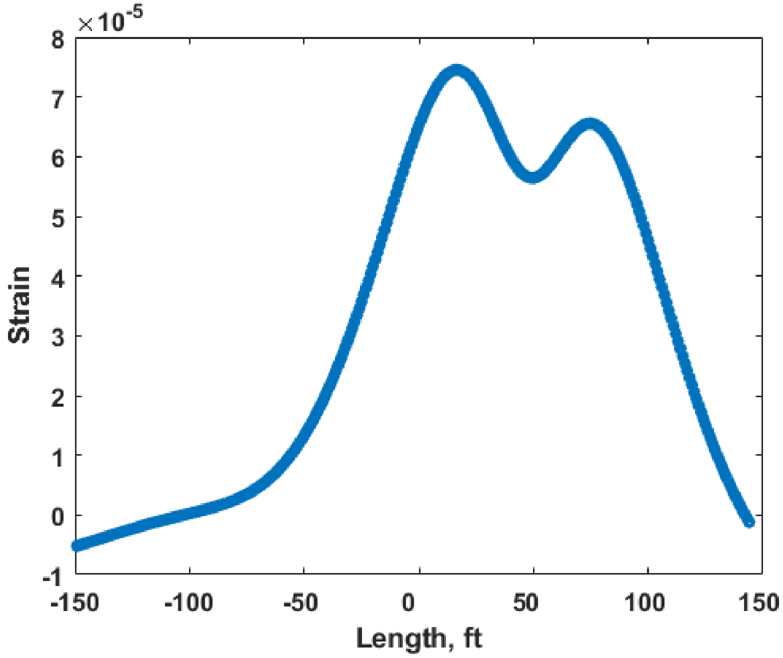

Fig. 3.21 Strain distribution based on fiber-optic measurement along the 400 ft location of the multiple fracture case

3.3 Strain Rate Calculation Model

The algorithm of the multiple-fracture strain rate calculation model has been introduced in the beginning of this chapter. An example of multiple fracture scenario will be shown below.

As shown in Fig. 3.22, five fractures propagate from the injection well (along *y* axial) to the imaginary offset well during hydraulic fracturing. The distance between the fractured well and imaginary well is 600 ft. The injection distribution is marked in the figure. The rest of the input used in simulation is listed in Table 3.3.

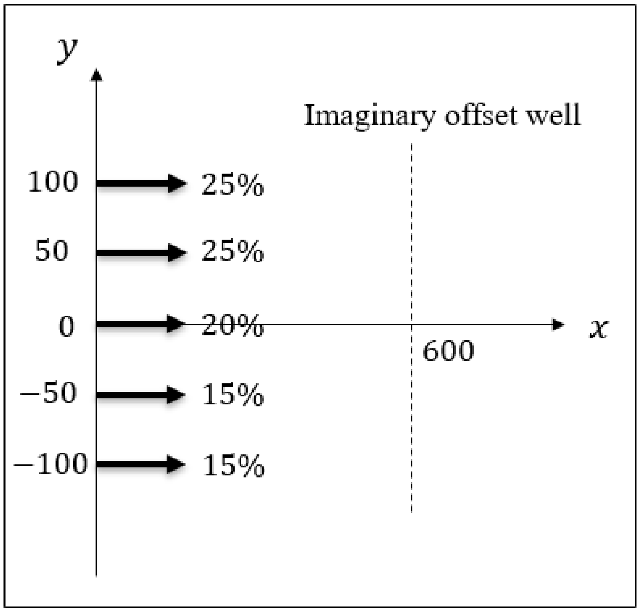

Fig. 3.22 Stimulation domain of the multiple fracture case

Table 3.3 Input data for strain rate simulation of the multiple fracture case

Parameter	Value
Young’s modulus, psi	4350000
Poisson’s ratio, /	0.2
Total injection rate per one side, bbl/min	45
Fluid viscosity, cp	5
Fracture height, ft	100
Injection time, min	60
Leak-off coefficient, $\mathrm{ft/min}^{0.5}$	0.001
Well spacing, ft	600
Gauge length, m	2

We calculate each fracture length over time and net pressure over time by using the KGD model separately. The simulation results show in Fig. 3.23 and Fig. 3.24. Then, at each time step, fracture width distribution will be calculated by using Equation 2.30. Afterward, follow the workflow of multiple fracture scenario, strain rate map based on rock deformation, and strain rate map based on displacement can be generated.

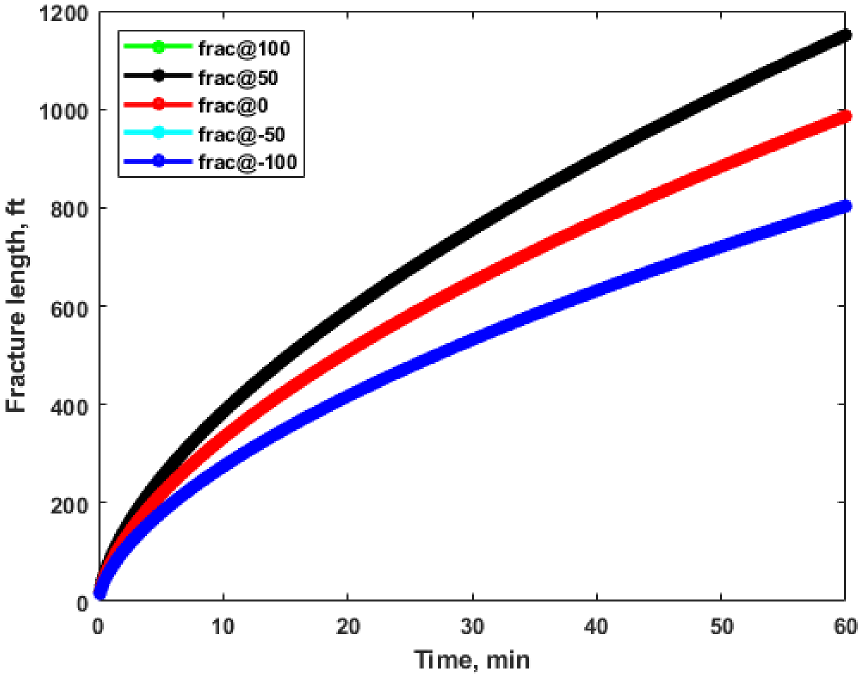

Fig. 3.23 Fracture half-length evolution over time of the multiple fracture case

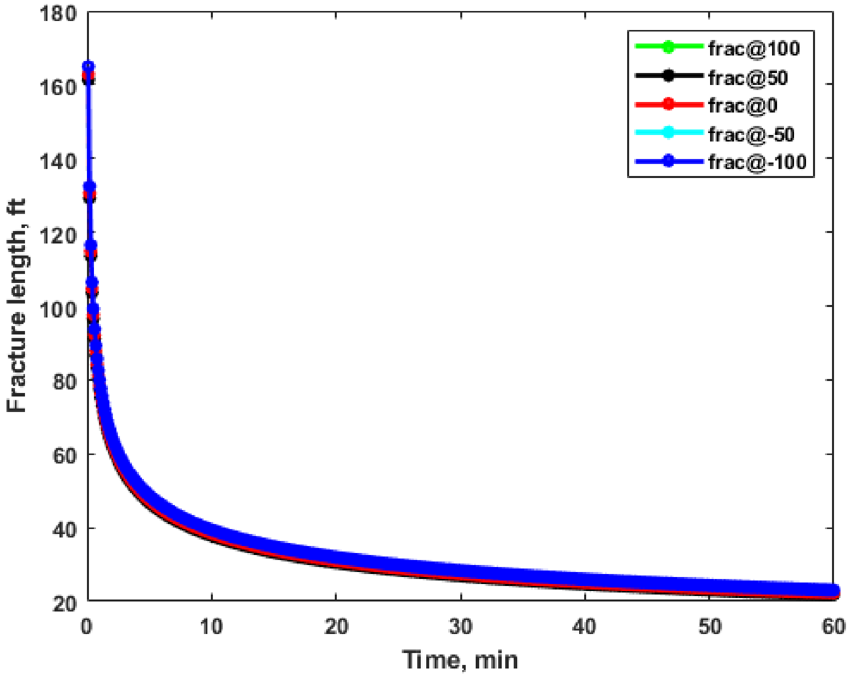

Fig. 3.24 Net pressure evolution over time of the multiple fracture case

3.3.1 Strain Rate Calculation Based on Rock Deformation

Follow the workflow of the multiple fracture scenario shown in Fig. 3.1, we first simulate far-field strain along the fiber based on rock deformation. The simulation result shows in Fig. 3.25.

As shown in the figure, five "yellow dots" can be easily recognized, that is when fractures hit the offset well, and the fiber shows extension. Before that, the strain at fiber is close to zero. After the fractures hit the offset well, the strain will become from extension (yellow) to compression (blue).

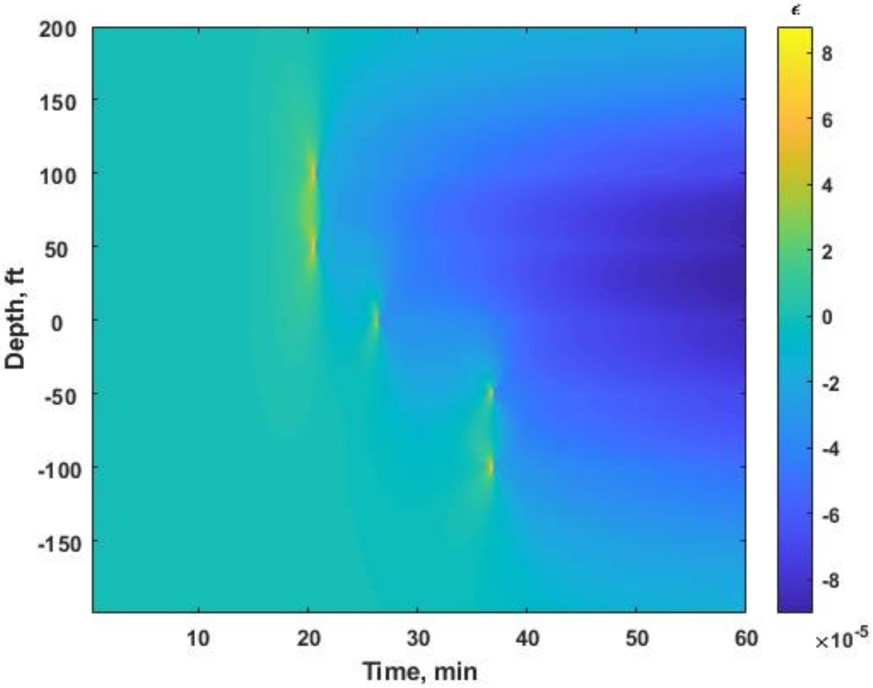

Fig. 3.25 Strain based on rock deformation at fiber location over time of the multiple fracture case

After getting the strain distribution based on rock deformation along the imaginary well over time, we can calculate strain rate over time by using Equation 2.52. The calculation result is shown in Fig. 3.26 based on Fig. 3.25.

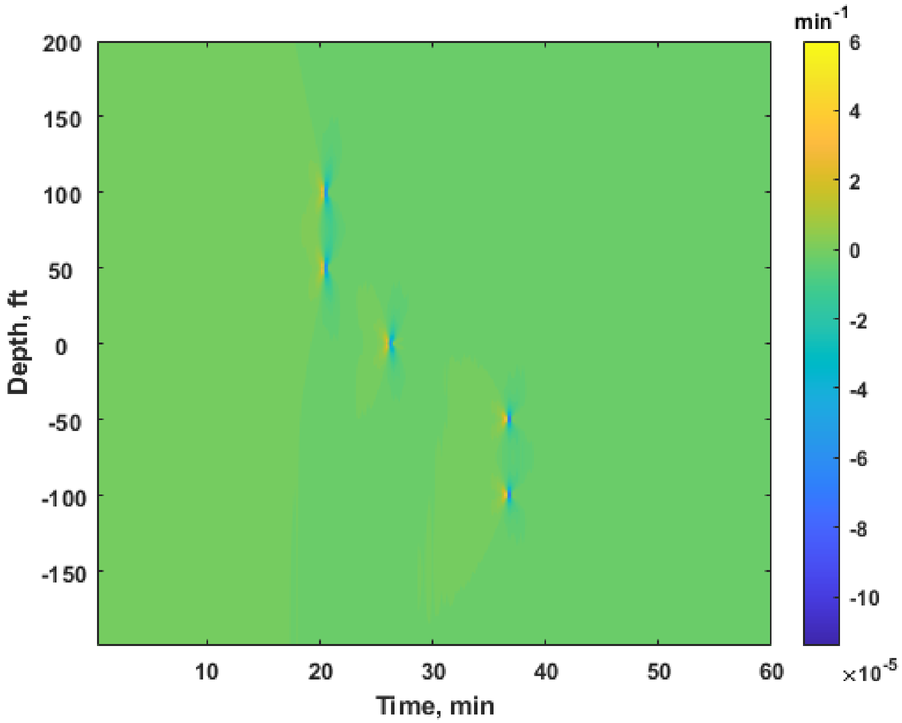

Fig. 3.26 Strain rate based on rock deformation at fiber location over time of the multiple fracture case

3.3.2 Strain Rate Calculation Based on Fiber-Optic Measurement

Follow the same workflow of multiple fracture scenario, we first simulate far-field strain along the fiber based on fiber-optic measurement. The result shows in Fig. 3.27. Five “yellow strips” can be observed in the figure. Besides that, the other parts show dark blue that the strain values are close to zero.

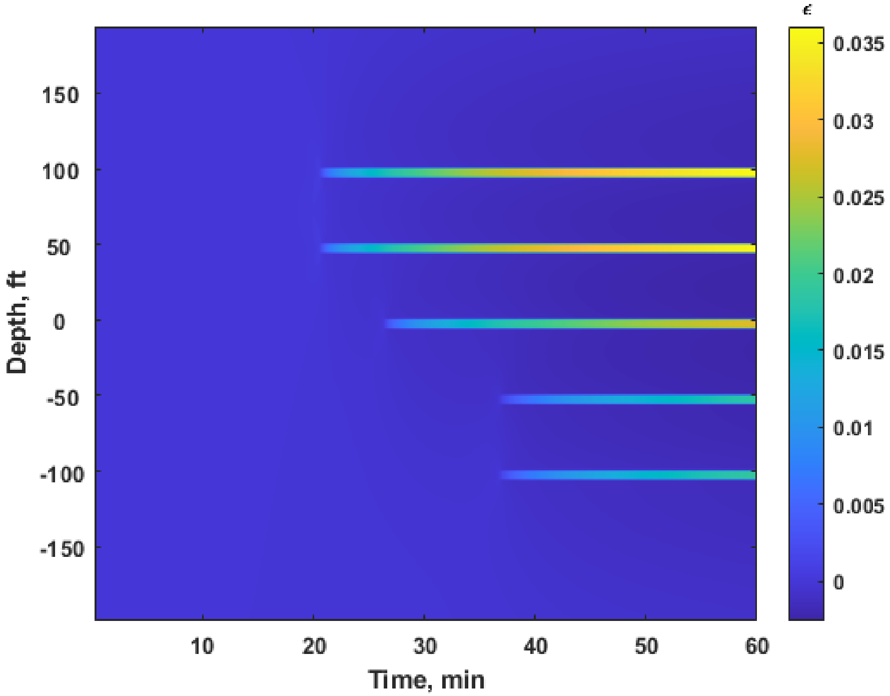

Fig. 3.27 Strain based on fiber-optic measurement at fiber location over time of the multiple fracture case

After calculating the strain based on fiber-optic measurement along the imaginary well over time, we can calculate strain rate over time by using Equation 2.52. The calculation result is shown in Fig. 3.28 based on Fig. 3.27. As we can see, five "yellow strips" are recognized in the figure, that is when fractures intercept the offset well. Besides the "yellow strips", the other part of the strain rate is hard to read, they are all very close to zero. That is why we need pattern generation to polarize the strain rate. This technique will be introduced in Chapter 4.

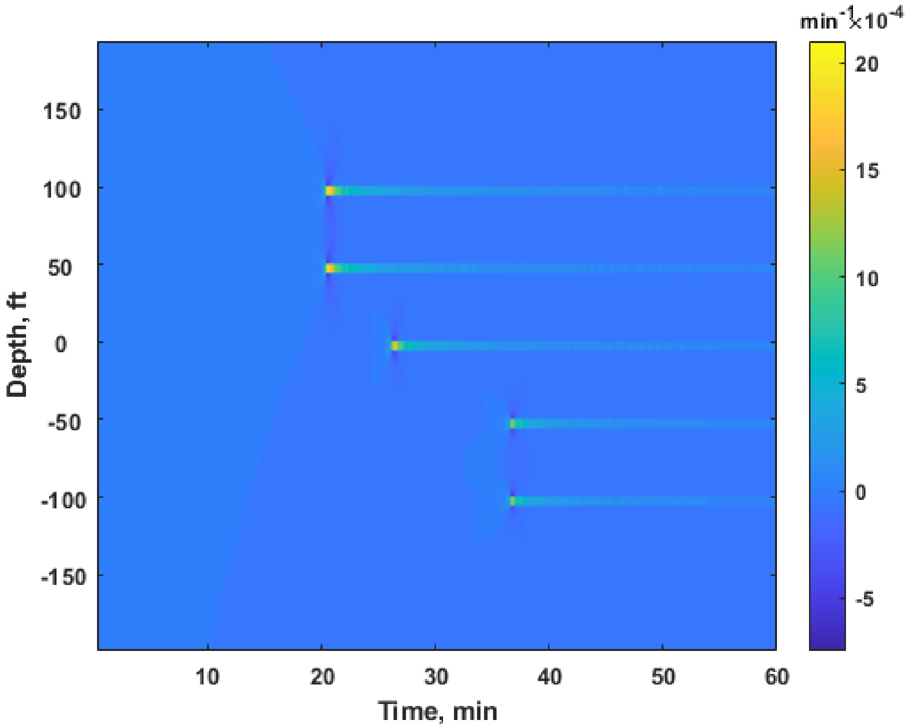

Fig. 3.28 Strain rate based on fiber-optic measurement at fiber location over time of the multiple fracture case

4 PATTERN GENERATION

4.1 Pattern Generation Methodology

To characterize strain rate pattern, special data processing needs to be performed on the strain rate data to get a more distinguishable pattern with polarity. We call this process pattern generation.

As shown in Chapter 2, the values of both strain rates based on rock deformation and fiber-optic measurement are widely distributed in a large range, which cannot be apparently featured in a waterfall plot. Therefore, based on many empirical attempts, we establish a workflow to process the simulated strain rate data and transform them into patterns that can be easily characterized. The following method is adopted for pattern generation.

We first magnify the raw strain rate data with a linear scale by multiplying a large number. In this dissertation, the strain rate $\dot{\varepsilon}$ is enlarged by 10^9. Afterward, the enlarged strain rate data, marked as $\ddot{\varepsilon}$, are transformed into a logarithmic scaling under the following rules,

$$\hat{\varepsilon} = \begin{cases} \log(\ddot{\varepsilon}), \ddot{\varepsilon} > 1 \\ 0, -1 \leq \ddot{\varepsilon} \leq 1 \\ -\log(-\ddot{\varepsilon}), \ddot{\varepsilon} < -1 \end{cases} \tag{4.1}$$

then, we can get the processed strain rate data, marked as $\hat{\varepsilon}$.

Generating waterfall plots from processed data $\hat{\varepsilon}$, the featured pattern can be investigated for the geo-mechanical information in the stimulation domain and mapped the fracture growth during hydraulic stimulation.

The workflow applied for both strain rates based on rock deformation and fiber-optic measurement. Pattern generation based on rock deformation and fiber-optic measurement is presented in this chapter. Examples of the single fracture scenario and multiple fracture scenario are shown by running synthetic inputs.

4.2 Pattern Generation for Rock Deformation

4.2.1 Single Fracture Scenario

A single fracture case study is conducted to illustrate how to transform raw strain rate data into featured pattern with polarity. The calculation of strain rate is based on rock deformation. Fig. 4.1 shows the stimulation domain of the single fracture case and the synthetic input data are listed in Table 4.1.

Initially, we calculate the raw strain rate based on rock deformation by following the procedures introduced in Chapter 2, and the calculation result is shown in Fig. 4.2. As we can see in the picture, there is not enough information that can be used to recognize a pattern because of the large range of magnitude of the strain rates.

Applying Equation 4.1, we generate Fig. 4.3 from Fig. 4.2, which shows more clear polarity. The positive values indicate rock extending and negative values indicate rock compressing in this plot.

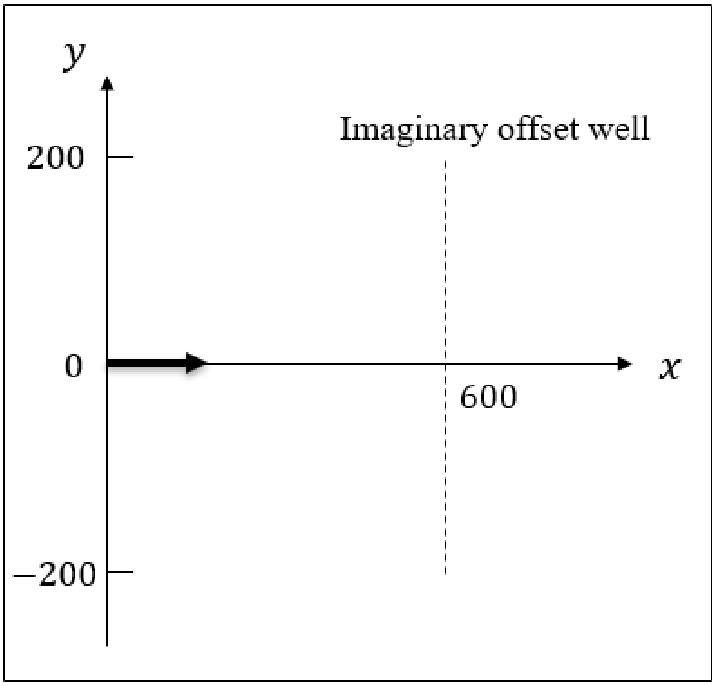

Fig. 4.1 Stimulation domain of the single fracture case for pattern generation study based on rock deformation

Table 4.1 Input data for strain rate simulation of the single fracture case for pattern generation study based on rock deformation

Parameter	Value
Young's modulus, psi	3625000
Poisson's ratio, /	0.22
Injection rate per one wing, bbl/min	25
Fluid viscosity, cp	5
Fracture height, ft	200
Injection time, min	60
Leak-off coefficient, $\mathrm{ft/min}^{0.5}$	0.001
Well spacing, ft	600

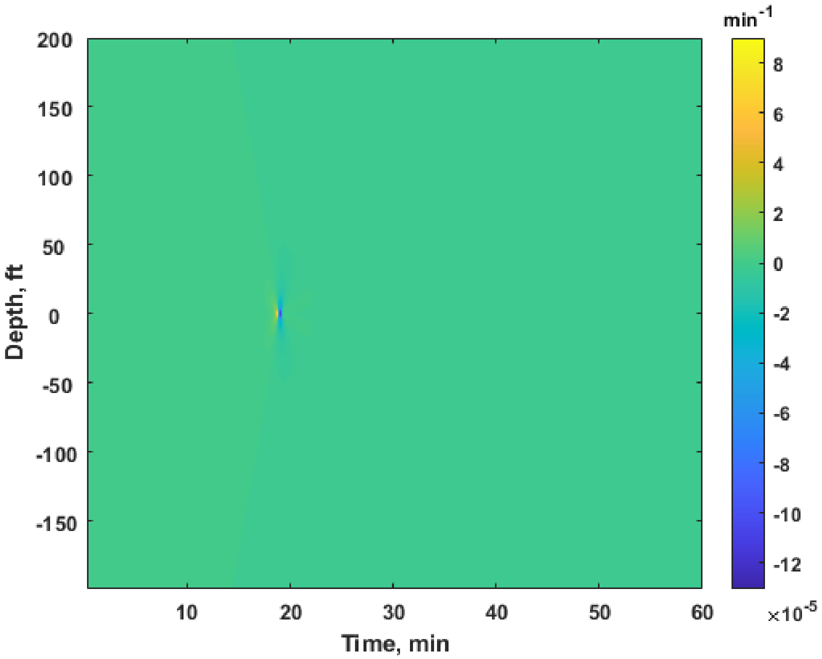

Fig. 4.2 Strain rate based on rock deformation at fiber location over time of the single fracture case for pattern generation study

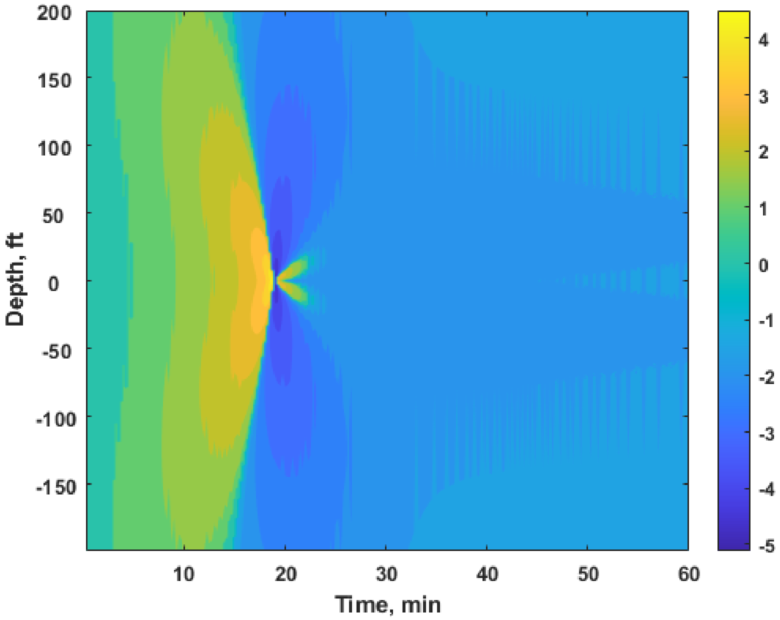

Fig. 4.3 Processed strain rate based on rock deformation at fiber location over time of the single fracture case for pattern generation study

4.2.2 Multiple Fracture Scenario

Multiple fracture case study is also conducted to illustrate the application of pattern generation. The calculation of the strain rate is based on rock deformation. Fig. 4.4 shows the stimulation domain of the multiple fracture case and the proportion of each fracture's fluid inflow relative to the total injection. The synthetic input data are listed in Table 4.2.

The input data give the total injection rate per one side of all fractures. Thus, the injection rate per one wing of each fracture can be calculated by distributing the total injection proportionally.

First, the fracture length over time and net pressure over time of each fracture are calculated separately. After that, the raw strain rate based on rock deformation is simulated by coupling the multiple fracture propagation model and the strain rate model that are all introduced in Chapter 3. The simulation result is shown in Fig. 4.5. Then, by applying Equation 4.1, we generate Fig. 4.6 from Fig. 4.5, in which much more geo-mechanical information is revealed from the pattern polarities.

In Fig. 4.6, the positive values indicate rock extending and negative values indicate rock compressing.

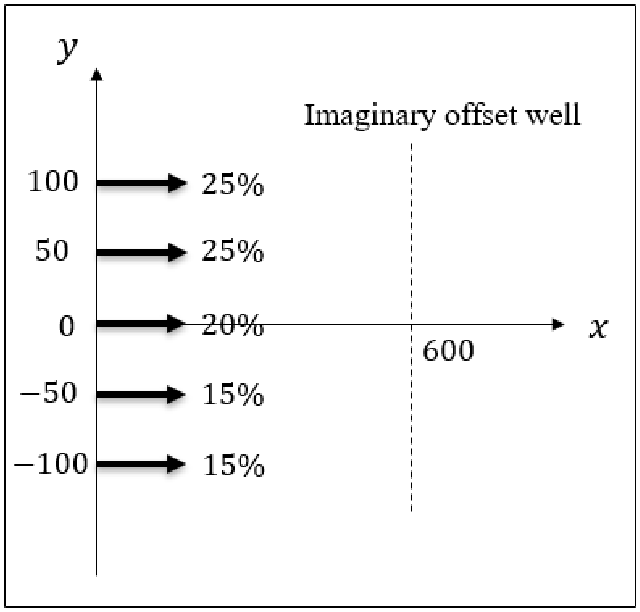

Fig. 4.4 Stimulation domain of the multiple fracture case for pattern generation study based on rock deformation

Table 4.2 Input data for strain rate simulation of the multiple fracture case for pattern generation study based on rock deformation

Parameter	Value
Young's modulus, psi	3625000
Poisson's ratio, /	0.22
Total injection rate per one side, bbl/min	90
Fluid viscosity, cp	5
Fracture height, ft	200
Injection time, min	60
Leak-off coefficient, ft/min$^{0.5}$	0.001
Well spacing, ft	600

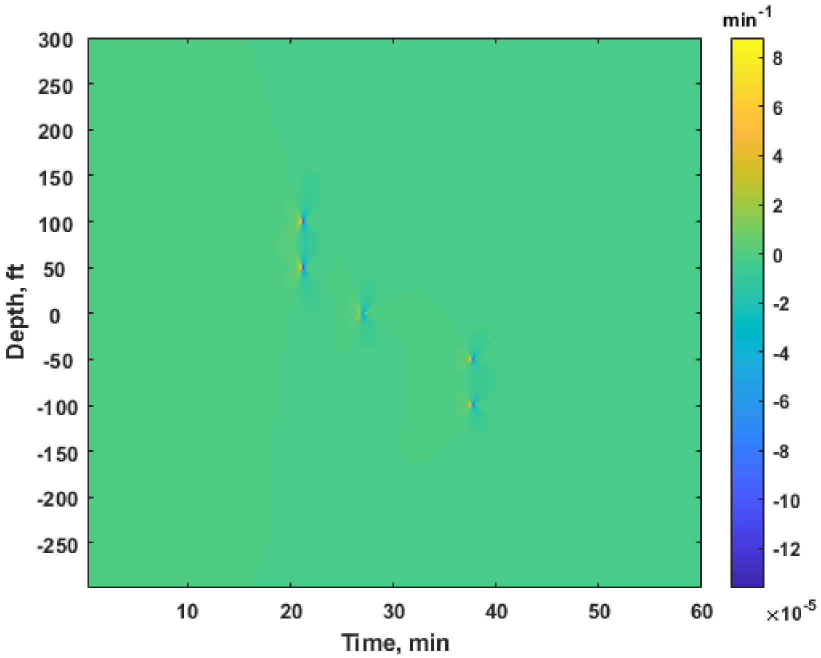

Fig. 4.5 Strain rate based on rock deformation at fiber location over time of the multiple fracture case for pattern generation study

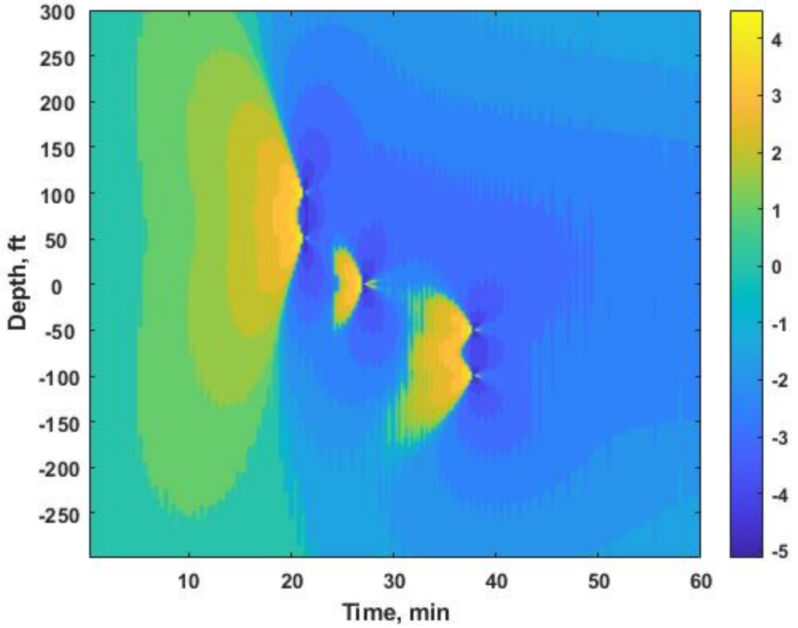

Fig. 4.6 Processed strain rate based on rock deformation at fiber location over time of the multiple fracture case for pattern generation study

4.3 Pattern Generation for Fiber-Optic Measurement

4.3.1 Single Fracture Scenario

A single fracture case study was performed to demonstrate how to use strain rates measured by fiber-optic sensors to generate patterns with polarities. The calculation of the strain rate is based on fiber-optic measurement. Fig. 4.7 shows the stimulation domain of the single fracture study and the synthetic input data listed in Table 4.3.

This case study is similar to the single fracture case of pattern generation by rock deformation. However, pattern generation for rock deformation does not consider the gauge length of fiber-optic sensors. This study illustrates the difference between the pattern generation by rock deformation and the pattern generation by fiber-optic measurement, which is realistic to the real low-frequency DAS data measured in the field. In this case, we use 10 m of the fiber gauge length.

Initially, we can get the strain rate based on fiber-optic measurement by the method discussed in Chapter 2. The calculation results are shown in Fig. 4.8. We then apply Equation 4.1 to rescale the strain rate, this step transforms Fig. 4.8 to Fig. 4.9, which has more clear characteristic geo-mechanical details.

In Fig. 4.9, the positive values indicate rock extending and the negative values indicate rock compressing. And from this figure, we can easily separate the entire fracturing process into two periods, as reflected from the pattern. Before the fracture arrives the offset well, the pattern shows a “cone shape” with extending. After the fracture intercepts with the offset well where the DAS sensor is installed, the pattern changes from the tip of the “cone shape” to a “strip”, as the fracture continues growing.

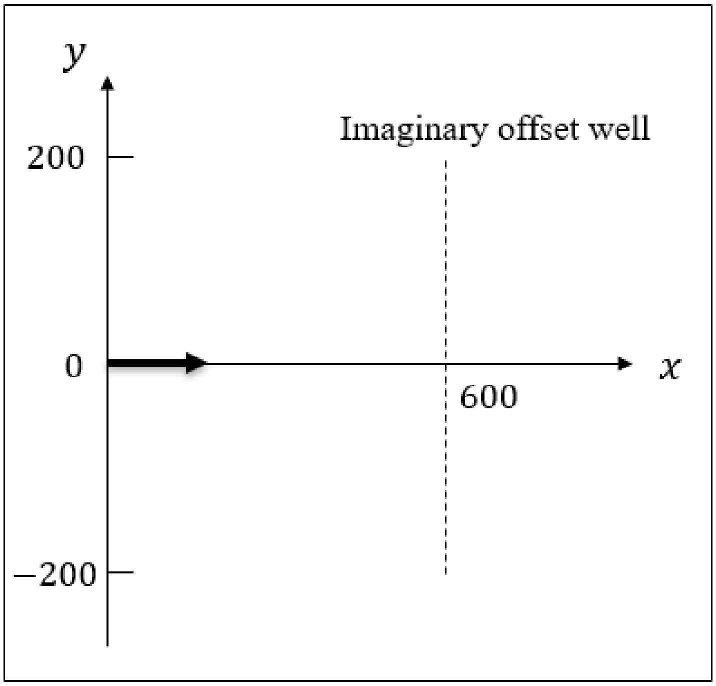

Fig. 4.7 Stimulation domain of the single fracture case for pattern generation study based on fiber-optic measurement

Table 4.3 Input data for strain rate simulation of the single fracture case for pattern generation study based on fiber-optic measurement

Parameter	Value
Young's modulus, psi	3625000
Poisson's ratio, /	0.22
Injection rate per one wing, bbl/min	25
Fluid viscosity, cp	5
Fracture height, ft	200
Injection time, min	60
Leak-off coefficient, $\mathrm{ft/min}^{0.5}$	0.001
Well spacing, ft	600
Gauge length, m	10

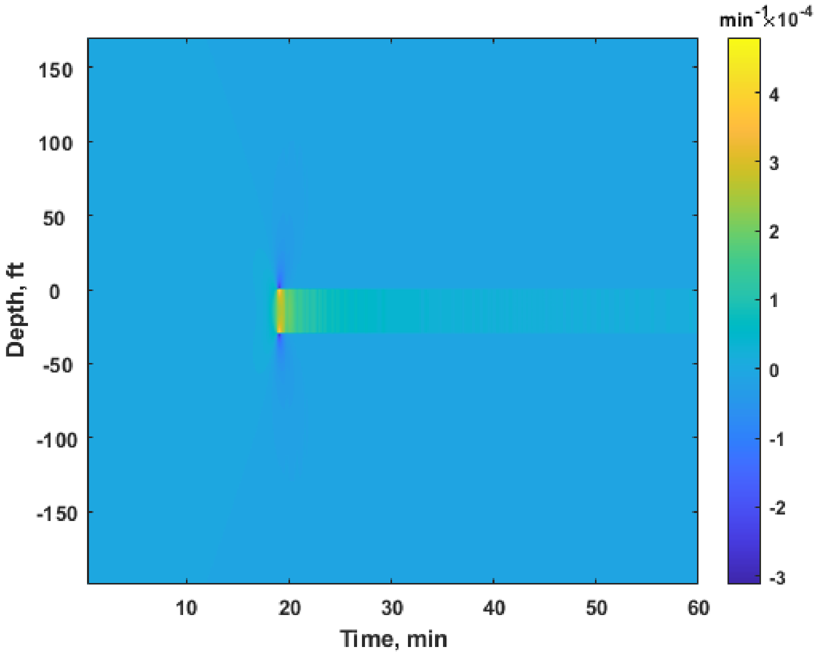

Fig. 4.8 Strain rate based on fiber-optic measurement over time of the single fracture case for pattern generation study

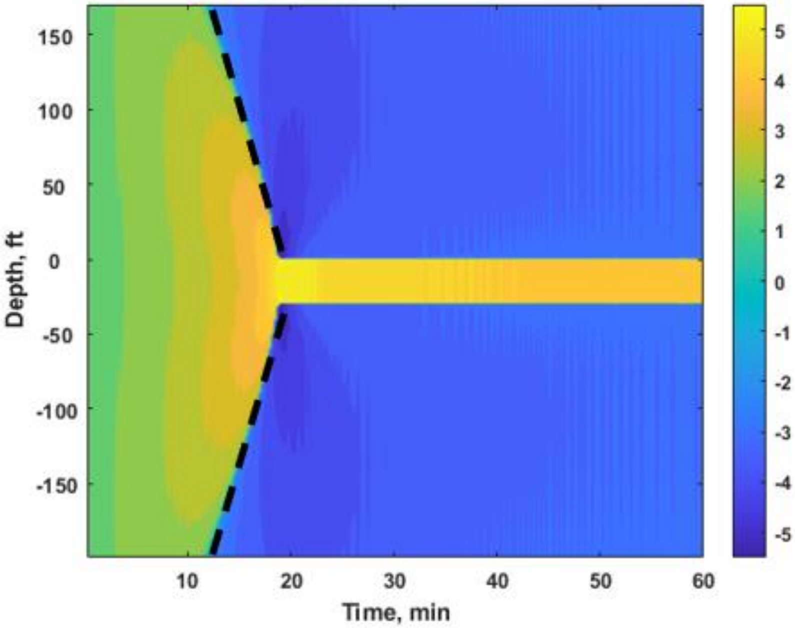

Fig. 4.9 Processed strain rate based on fiber-optic measurement over time of the single fracture case for pattern generation study

To simplify the problem, a dashed line as marked in Fig. 4.9 is defined as the slope of the "cone pattern" when assuming a linear boundary between the extending zone (yellow colored) and the compressing zone (blue colored). It is a linear curve fitting along the intersection of the extending zone and the compressing zone. Because the upper part and lower part of the "cone shape" are symmetric, therefore, the absolute value of either one can be used as the slope value of the cone shape. The magnitude of the slope is related to the propagation velocity or the injection rate of the fracture. This value will be used for an empirical equation in Chapter 5.

4.3.2 Multiple Fracture Scenario

Multiple fracture example is used here to show how to perform pattern generation for fiber-optic measurement. Fig. 4.10 shows the stimulation domain of the multiple fracture case and the synthetic input data are listed in Table 4.4.

The same as the multiple fracture case study of pattern generation for rock deformation, in this case study, the input data also give the total injection rate per one side. Therefore, we can proportionally distribute the total injection rate per one side to each of the fractures.

First, the fracture length over time and net pressure over time of each fracture are calculated individually. After that, the strain rate based on fiber-optic measurement is simulated by coupling the multiple fracture propagation model and the strain rate model that is introduced in Chapter 3. The simulation result is shown in Fig. 4.11. Then, by applying Equation 4.1, we make Fig. 4.12 from Fig. 4.11. Fig. 4.12 shows more pattern polarities for fracture diagnosis. In this plot, the positive values indicate rock extending and the negative values indicate rock compressing.

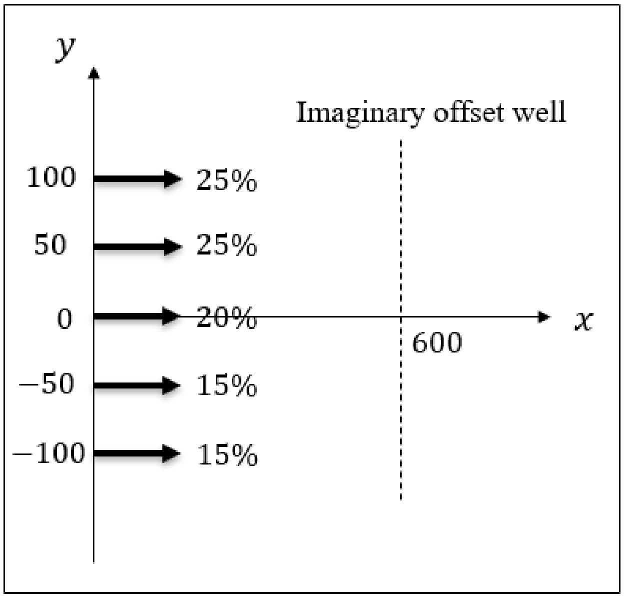

Fig. 4.10 Stimulation domain of the multiple fracture case for pattern generation study based on fiber-optic measurement

Table 4.4 Input data for strain rate simulation of the multiple fracture case for pattern generation study based on fiber-optic measurement

Parameter	Value
Young’s modulus, psi	3625000
Poisson’s ratio, /	0.22
Total injection rate per one side, bbl/min	45
Fluid viscosity, cp	5
Fracture height, ft	100
Injection time, min	60
Leak-off coefficient, $\mathrm{ft/min}^{0.5}$	0.001
Well spacing, ft	600
Gauge length, m	10

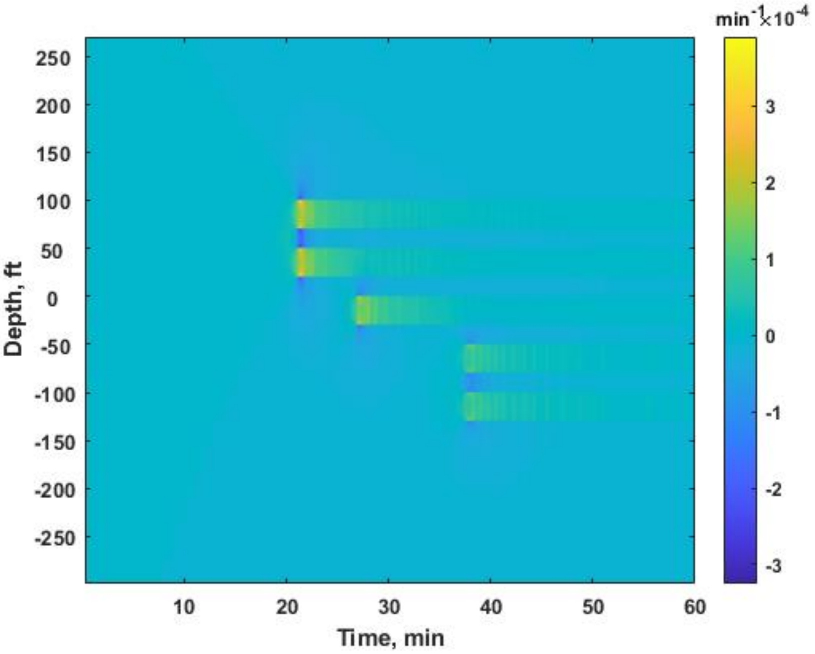

Fig. 4.11 Strain rate based on fiber-optic measurement at fiber location over time of the multiple fracture case for pattern generation study

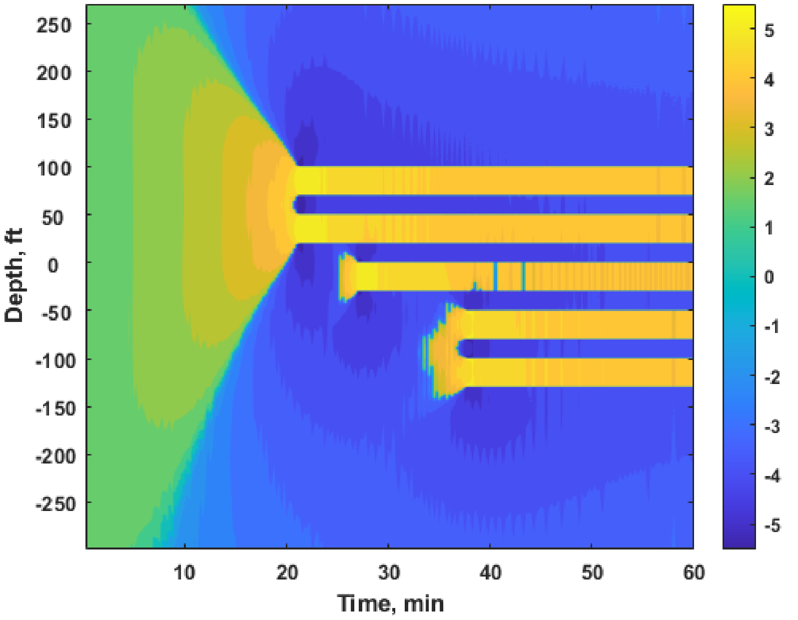

Fig. 4.12 Processed strain rate based on fiber-optic measurement over time of the multiple fracture case for pattern generation study

As we can see in Fig. 4.12, the process of multiple fracture hydraulic stimulation is reflected from the pattern features as following. A broad range of extending “cone shape” appears once the treatment started. However, the “cone shape” is not symmetric comparing to the single fracture case. The “cone shape” is biased to the “upper side” where the fractures propagate faster. After the fastest fractures intercepted the offset well, the “strip” occurs like the single fracture case. And for the fractures that are still developing but have not arrived the offset well, the extending cannot be appeared until the fractures get close enough to the fiber. Once they get close enough to the fiber, the relatively small “cone shape” will appear and then will transform to the “strip” very soon. The fiber location correlated to the fractures showed compressing. Once those slower-growing fractures are getting close enough to the fiber, a small “cone shape” will appear, and until they actually intercepted the offset well, then the “cone shape” turns to a “strip”.

5 PARAMETRIC STUDY

5.1 Introduction

To fully understand the determinations and sensitivities of far-field strain rate patterns, parametric study has been conducted. Based on the results of parametric study, an empirical correlation is developed.

In this dissertation, parametric study is only performed on the single fracture scenario. All investigations for parametric study are based on the same stimulation domain as shown in Fig. 5.1.

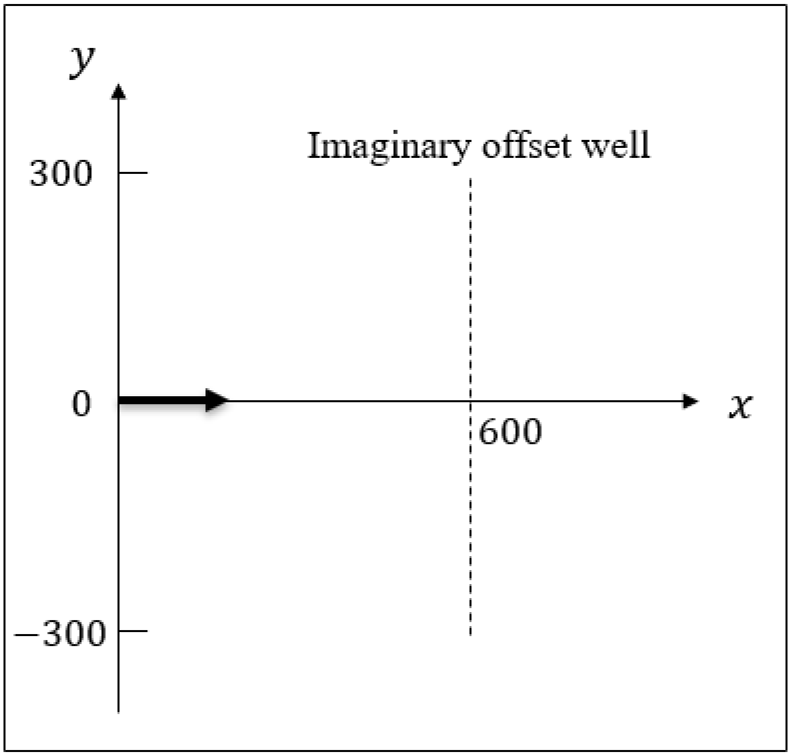

Fig. 5.1 Stimulation domain for the parametric study

In parametric study, we try to understand the effects of the parameters of fracture treatments on the far-field strain rate pattern. The studied parameters include treatment design, fluid property, reservoir property, and the property of the fiber-optic sensors. The parameters are changed one at a time while keeping the other parameters constant. This helps to identify the influential parameter to the far-field strain rate pattern.

To develop empirical correlation, multiple synthetic data were generated to build the relationship between the pattern against the injection rate of the hydraulic stimulation. This study provides useful insights for interpreting low-frequency DAS data on fracture propagation velocity.

5.2 Parametric Study

5.2.1 Injection Rate

The injection rate is always considered as one of the most important parameters in hydraulic fracturing design. Four different cases with different injection rates per one wing of the fracture are used: 10 bbl/min, 15 bbl/min, 20 bbl/min, 40 bbl/min. The other synthetic inputs are listed in Table 5.1.

The simulation is conducted by changing injection rates while keeping the other parameters constant. With the fracture growth continuing, the strain rate based on fiber-optic measurement is documented along with the offset well where the fiber sensor is assuming installed. Pattern generation is performed to the simulation results and analysis is also made on those patterns.

The pattern generations are shown in Fig. 5.2, Fig. 5.2(a) is the simulation result of the hydraulic stimulation with 10 bbl/min injection rate, Fig. 5.2(b) is with 15 bbl/min injection rate, Fig. 5.2(c) is for 20 bbl/min injection rate, and Fig. 5.2(d) is for 40 bbl/min injection rate.

Table 5.1 Input data for injection rate investigation

Parameter	Value
Young’s modulus, psi	4350000
Poisson’s ratio, /	0.22
Fluid viscosity, cp	5
Fracture height, ft	200
Injection time, min	60
Leak-off coefficient, $\mathrm{ft/min}^{0.5}$	0.001
Well spacing, ft	600
Gauge length, m	10

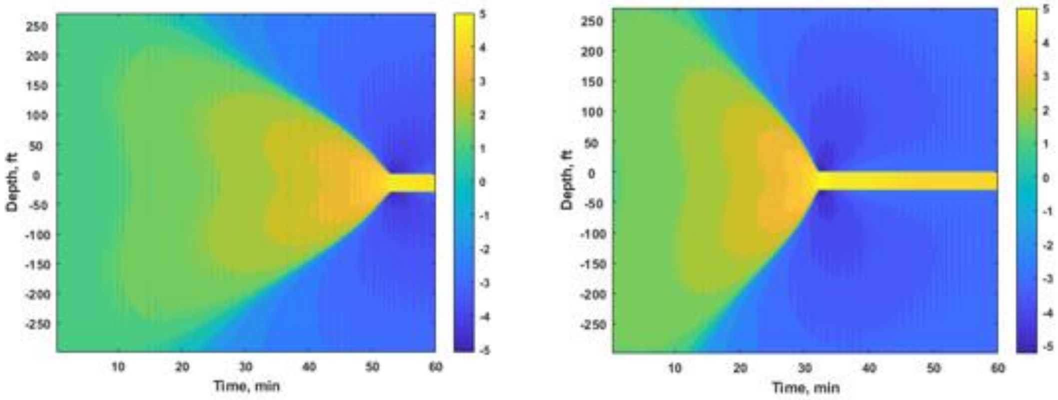

(a) $q = 10\ bbl/min$ (b) $q = 15\ bbl/min$

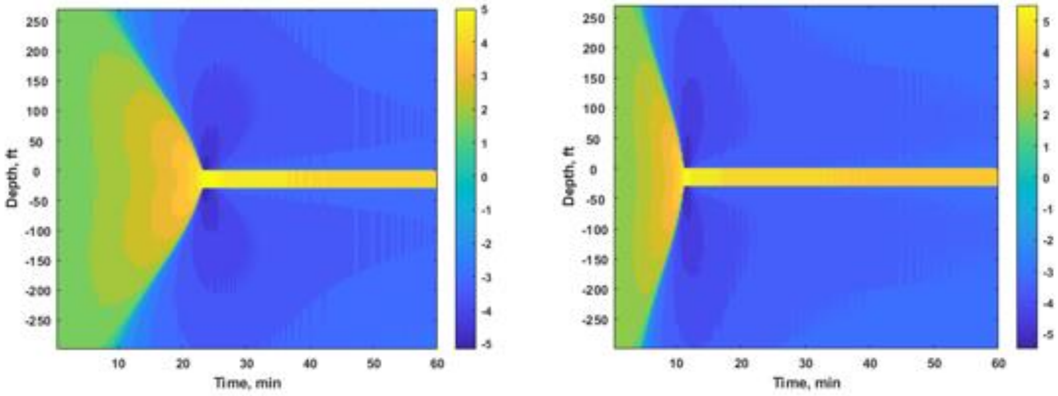

(c) $q = 20\ bbl/min$ (d) $q = 40\ bbl/min$

Fig. 5.2 Simulation results of different injection rates

As we can see clearly from Fig. 5.2, the increase in the injection rate will affect the shape of the pattern. The "slope of the core pattern" is sensitive to the injection rate. We can conclude from Fig. 5.2 that the higher the injection rate, the flatter the cone shape pattern.

5.2.2 Fluid Viscosity

To explore the impact of fluid viscosity on the pattern shape, four different cases are examined with different fluid viscosities: 5 cp, 35 cp, 65 cp, 100 cp, covering from low-viscosity slickwater to conventional high-viscosity fluid. The other inputs for the case are listed in Table 5.2.

The patterns generated are shown in Fig. 5.3. The pattern changes as fluid viscosity changes. Fig. 5.3(a) is for viscosity of 5 cp, Fig. 5.3(b) is for 35 cp, Fig. 5.3(c) is for 65 cp, and Fig. 5.3(d) is for 100 cp of fluid viscosity.

Table 5.2 Input data for fluid viscosity investigation

Parameter	Value
Young's modulus, psi	4350000
Poisson's ratio, /	0.22
Injection rate per one wing, bbl/min	15
Fracture height, ft	100
Injection time, min	60
Leak-off coefficient, $\mathrm{ft/min}^{0.5}$	0.001
Well spacing, ft	600
Gauge length, m	10

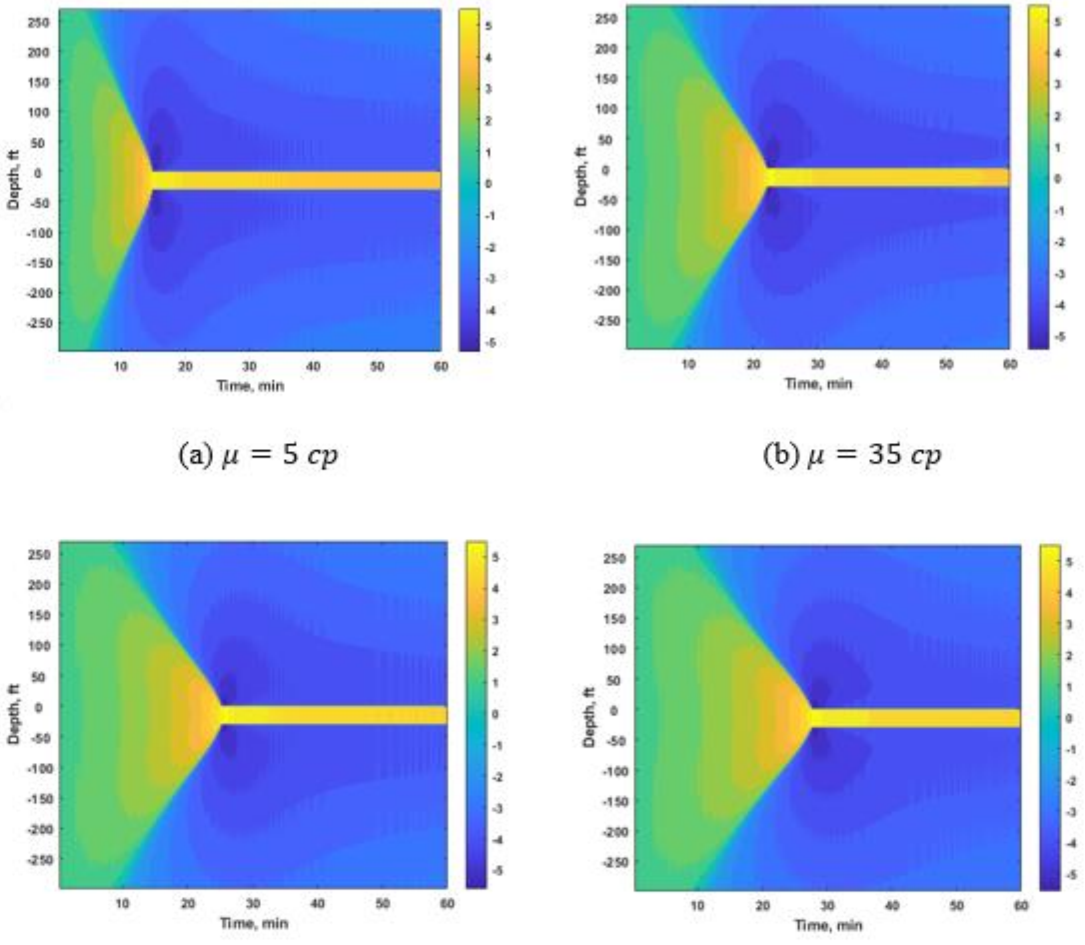

(a) $\mu = 5\ cp$ (b) $\mu = 35\ cp$

(c) $\mu = 65\ cp$ (d) $\mu = 100\ cp$

Fig. 5.3 Simulation results of different fluid viscosities

Fig. 5.3 shows that the increase of the fluid viscosity will not be a compelling effect on changing the slope of the pattern. But the region of the affected area of strain rate increases as fluid viscosity increases. The slope of the pattern almost keeps constant as the fluid viscosity increases. The intensity of strain rate change is also about the same. The viscosity increases only "enlarges" the cone shape.

5.2.3 Young's Modulus

Young’s modulus of different reservoir rocks can vary in a considerable range, and it is a crucial parameter for fracture treatment design. To better understand the relationship of Young’s modulus and the far-field strain rate pattern shape, we apply four different cases with different Young's moduli: 1.45E6 psi, 3.625E6 psi, 5.8E6 psi, 7.975E6 psi. The stimulation domain is shown in Fig. 5.1. The other input is listed in Table 5.3.

The simulation results are shown in Fig. 5.4, Fig. 5.4(a) is for Young’s modulus of 1.45E6 psi, Fig. 5.4(b) is for 3.625E6 psi, Fig. 5.4(c) is for 5.8E6 psi, Fig. 5.4(d) is for 7.975E6 psi of Young’s modulus.

Table 5.3 Input data for Young’s modulus investigation

Parameter	Value
Poisson’s ratio, /	0.22
Injection rate per one wing, bbl/min	15
Fluid viscosity, cp	5
Fracture height, ft	100
Injection time, min	60
Leak-off coefficient, ft/min$^{0.5}$	0.001
Well spacing, ft	600
Gauge length, m	10

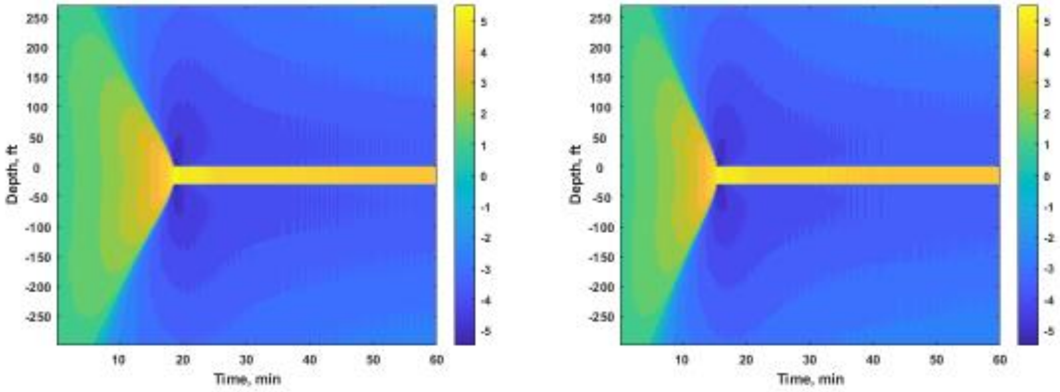

(a) $E = 1450000\,psi$ (b) $E = 3625000\,psi$

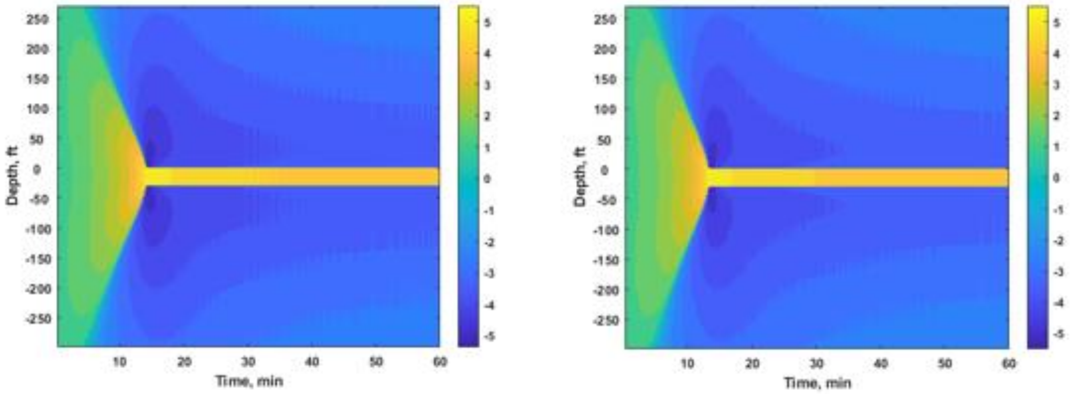

(c) $E = 5800000\,psi$ (d) $E = 7975000\,psi$

Fig. 5.4 Simulation results of different Young’s moduli

By analyzing Fig. 5.4, we observed that Young’s modulus has less impact on the shape of strain rate responses to fracture propagation compared with injection rate and fluid viscosity. As Young’s modulus increases, the slope of the core shape becomes flatter. In the range of examination (from 1.45E6 psi to 7.975E6 psi), the shape only changed slightly.

5.2.4 Poisson's Ratio

In general, Poisson's ratio for formation rocks only varies in a small range. In this study, we use the Poisson's ratio value from an extremely small number to an extremely large number to characterize the impact of Poisson's ratio on the pattern shape of far-field strain rates during hydraulic fracturing treatment.

We performed four different cases with different Poisson's ratios: 0.18, 0.22, 0.26, 0.3. The other input is listed in Table 5.4.

The simulation results are shown in Fig. 5.5, Fig. 5.5(a) is for the case with Poisson’s ratio of 0.18, Fig. 5.5(b) is for Poisson’s ratio of 0.22, Fig. 5.5(c) is for Poisson’s ratio of 0.26, and Fig. 5.5(d) is the case of Poisson’s ratio being 0.3.

Table 5.4 Input data for Poisson's ratio investigation

Parameter	Value
Young’s modulus, psi	3625000
Injection rate per one wing, bbl/min	15
Fluid viscosity, cp	5
Fracture height, ft	200
Injection time, min	60
Leak-off coefficient, $\mathrm{ft/min}^{0.5}$	0.001
Well spacing, ft	600
Gauge length, m	10

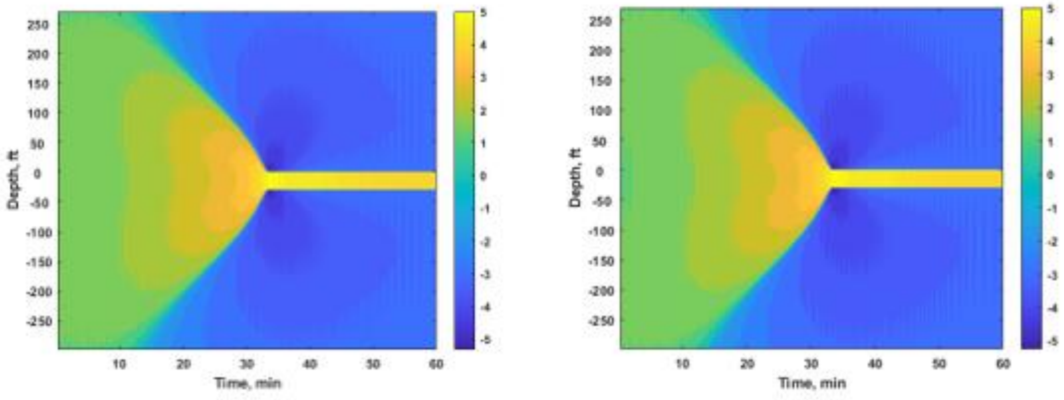

(a) $\nu = 0.18$

(b) $\nu = 0.22$

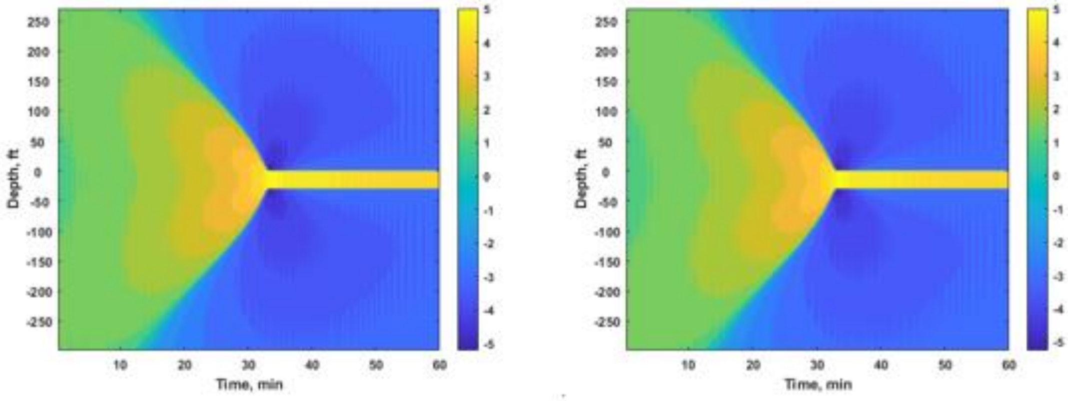

(c) $\nu = 0.26$

(d) $\nu = 0.3$

Fig. 5.5 Simulation results of different Poisson's ratios

From Fig. 5.5, we cannot distinguish the difference from the pattern slope changing by applying Poisson's ratio from an extremely small magnitude to an extremely large magnitude, and this concludes that Poisson's ratio of formation rock has little effect on strain rate pattern during fracturing.

5.2.5 Leak-Off Coefficient

During hydraulic fracturing treatments, fracture fluid can leak into permeable formations, changing fracture propagation from ideal condition. Investigating how the leak-off coefficient affects strain rate pattern shape change is necessary.

In this study, we applied four different cases with different leak-off coefficients being 0.001 $\mathrm{ft/min^{0.5}}$, 0.002 $\mathrm{ft/min^{0.5}}$, 0.003 $\mathrm{ft/min^{0.5}}$, and 0.004 $\mathrm{ft/min^{0.5}}$. The stimulation domain is the same as shown in Fig. 5.1. Other input is listed in Table 5.5.

The simulation results are shown in Fig. 5.6, Fig. 5.6(a) is the result for leak-off coefficient of 0.001 $\mathrm{ft/min^{0.5}}$, Fig. 5.6(b) is for 0.002 $\mathrm{ft/min^{0.5}}$, Fig. 5.6(c) is for 0.003 $\mathrm{ft/min^{0.5}}$, and Fig. 5.6(d) is the result of 0.004 $\mathrm{ft/min^{0.5}}$ leak-off coefficient.

Table 5.5 Input data for leak-off coefficient investigation

Parameter	Value
Young’s modulus, psi	3625000
Poisson’s ratio, /	0.22
Injection rate per one wing, bbl/min	20
Fluid viscosity, cp	5
Fracture height, ft	100
Injection time, min	60
Well spacing, ft	600
Gauge length, m	10

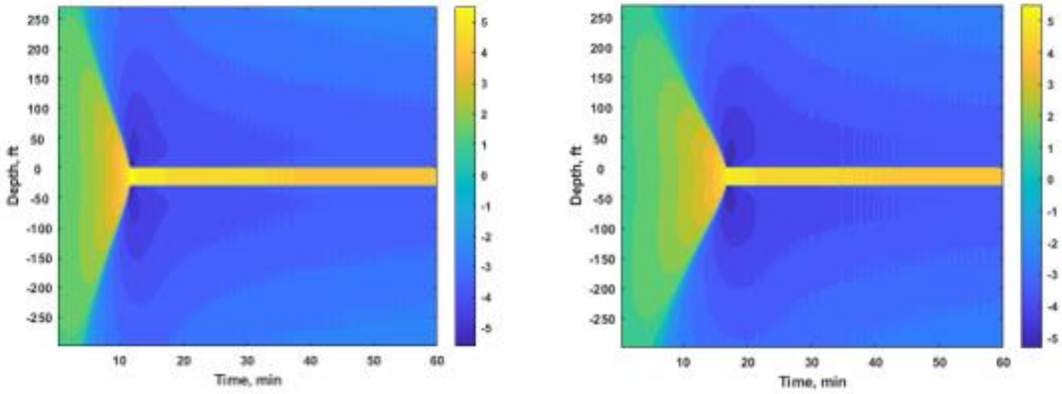

(a) $C_L = 0.001\ \mathrm{ft/min}^{0.5}$ (b) $C_L = 0.002\ \mathrm{ft/min}^{0.5}$

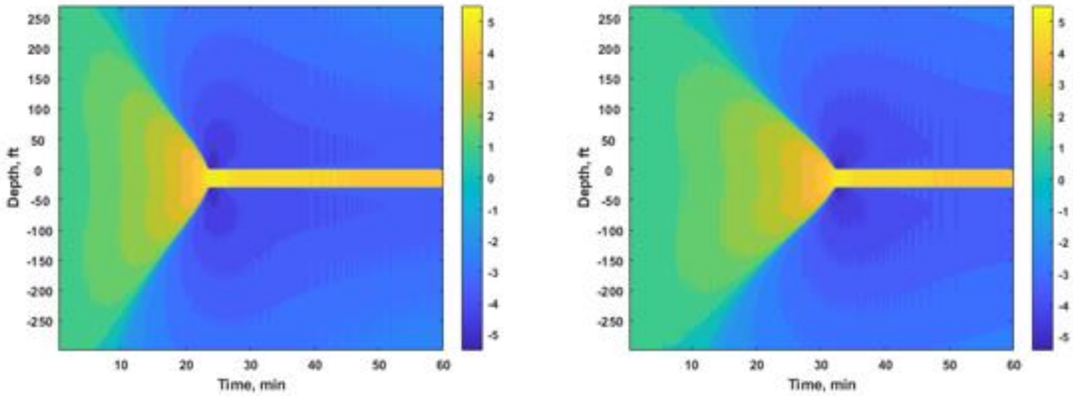

(c) $C_L = 0.003\ \mathrm{ft/min}^{0.5}$ (d) $C_L = 0.004\ \mathrm{ft/min}^{0.5}$

Fig. 5.6 Simulation results of different leak-off coefficients

Comparing the four plots in Fig. 5.6, it is clear that the pattern shape change is very sensitive to the leak-off coefficients. As leak-off coefficient increases, the cone shape becomes narrower but longer, and the slope of the cone is steeper.

5.2.6 Fracture Height

In the single fracture propagation model, the fracture height is constant along the fracture. To investigate the effect of fracture height on the pattern shape of strain rate, we use four different case studies with different fracture heights of 50 ft, 100 ft, 200 ft, and 300 ft. The stimulation domain is shown in Fig. 5.1. Other input for this case is listed in Table 5.6.

The simulation results are shown in Fig. 5.7. Fig. 5.7(a), (b), (c), (d) are for fracture height equals 50 ft, 100 ft, 200 ft, and 300 ft, respectively.

Table 5.6 Input data for fracture height investigation

Parameter	Value
Young's modulus, psi	3625000
Poisson's ratio, /	0.22
Injection rate per one wing, bbl/min	25
Fluid viscosity, cp	5
Injection time, min	60
Leak-off coefficient, $\mathrm{ft/min^{0.5}}$	0.001
Well spacing, ft	600
Gauge length, m	10

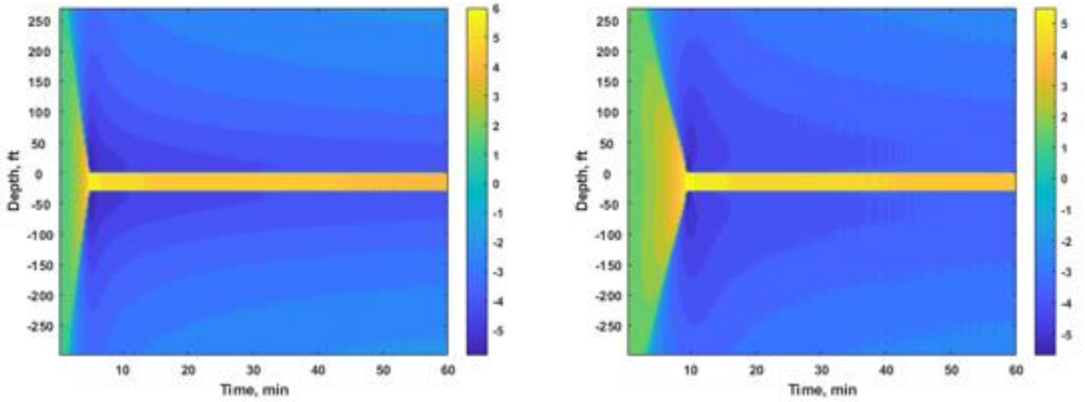

(a) $h_f = 50\ ft$ (b) $h_f = 100\ ft$

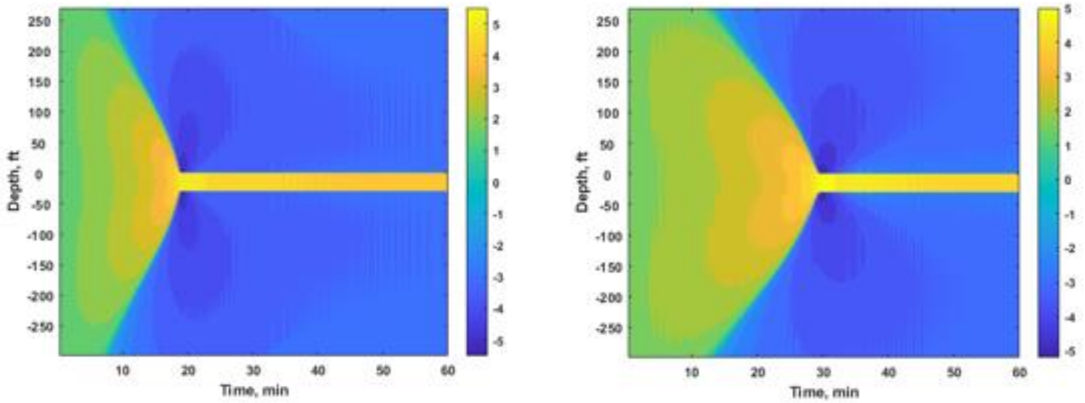

(c) $h_f = 200\ ft$ (d) $h_f = 300\ ft$

Fig. 5.7 Simulation results of different fracture heights

For a fixed injection rate (same injection rate and time for all cases), larger fracture height changes the strain rate with larger measured depth (comparing Fig. 5.7(d) with Fig. 5.7(a)). It takes much shorter time for fracture front to reach the observation location for small height case. Because the fracture volume is smaller, the area of cone shape is also smaller.

5.2.7 Gauge Length

As introduced before, DAS measures strain changes over a spatial distance. This distance is called gauge length. In our strain rate based on fiber-optic measurement simulation, the gauge length of fiber-optic sensor is given as an input. To investigate the impact of gauge length on the pattern shape of strain rate, we use four different gauge lengths: 2 m, 10 m, 20 m, and 40 m for the study. The stimulation domain is shown in Fig. 5.1. The other input is listed in Table 5.7.

Table 5.7 Input data for gauge length investigation

Parameter	Value
Young's modulus, psi	3625000
Poisson's ratio, /	0.22
Injection rate per one wing, bbl/min	25
Fluid viscosity, cp	5
Injection time, min	60
Leak-off coefficient, $\mathrm{ft/min^{0.5}}$	0.001
Well spacing, ft	600
Fracture height, ft	200

The simulation results are shown in Fig. 5.8. Fig. 5.8(a) is for the gauge length of the fiber being 2 m, Fig. 5.8(b) is for 10 m, Fig. 5.8(c) is for 20 m, Fig. 5.8(d) is with 40 m gauge length of the fiber.

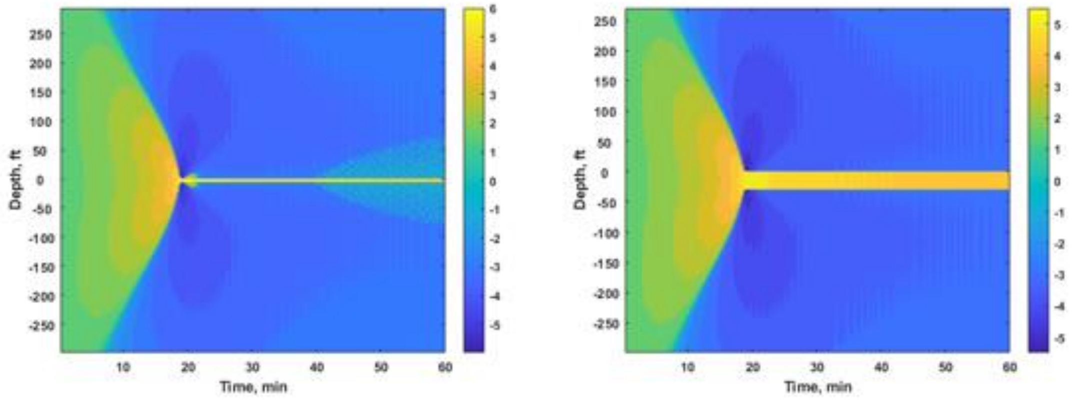

(a) $GL = 2\ m$ (b) $GL = 10\ m$

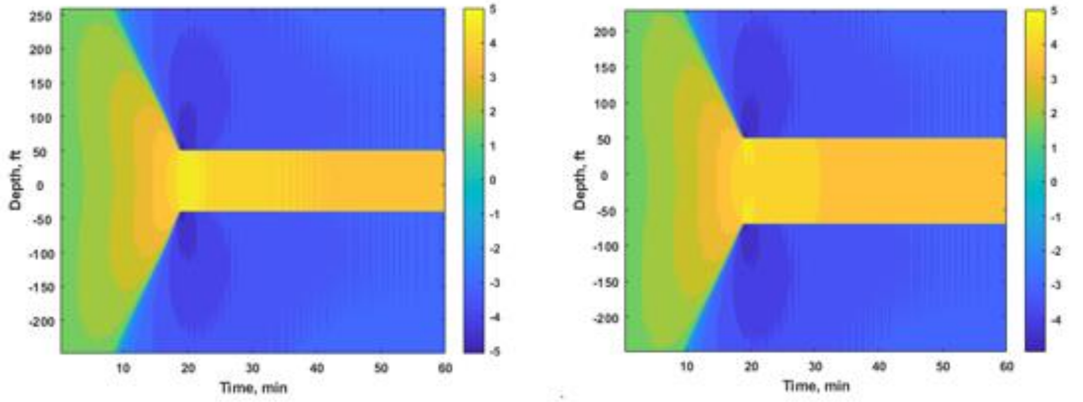

(c) $GL = 20\ m$ (d) $GL = 40\ m$

Fig. 5.8 Simulation results of different gauge lengths

As we can see in Fig. 5.8, the gauge length does not affect the “cone shape” pattern before the fracture arrives at the imaginary offset well. However, it affects the width of the “strip” pattern after fracture intercepts the imaginary offset well and passing through it. We can conclude from Fig. 5.8 that with enlarging the gauge length of the fiber, the width of “strip” pattern increases.

5.2.8 Section Summary

From the results presented in this section, it is observed in all cases that a cone shape pattern exists for strain rate recorded by DAS when fracture intercepts the sensor.

Of the parameters studies, injection rate is the most influential parameter, and an increased injection rate makes the slope of the cone flatter. Fluid viscosity and rock mechanical properties (Young's modulus and Poisson's ratio) have insignificant effects on strain pattern, either shape or intensity. Leak-off coefficient and fracture height change shape of cone pattern, but not on the slope. These observations can be helpful when interpreting low-frequency DAS measurements.

5.3 Empirical Correlation Based on Simulation Results

In the previous section, several parameters are examined to identify the factors that are important in pattern shape study. Injection rate is one of the important parameters for hydraulic fracturing design. From the parametric study, we also realize that injection rate is one of the most sensitive parameters that impact the pattern shape of strain rate recorded by DAS.

In this section, a quantitative correlation between the slope of the cone pattern and the injection rate will be developed, aiming to help interpret low-frequency DAS data. The correlation is built based on simulation results. Note that only one parameter, injection rate, is examined here.

Four different injection rates of 10 bbl/min, 15 bbl/min, 20 bbl/min, 25 bbl/min, are used to generate waterfall plot for strain rate and build the correlation. The stimulation domain is shown in Fig. 5.1. The other input is listed in Table 5.8.

Table 5.8 Input data for empirical correlation study

Parameter	Value
Young's modulus, psi	4350000
Poisson's ratio, /	0.26
Fluid viscosity, cp	5
Fracture height, ft	200
Injection time, min	60
Leak-off coefficient, $\mathrm{ft/min}^{0.5}$	0.001
Well spacing, ft	600
Gauge length, m	10

Fig. 5.9 shows the pattern generation results based on different injection rates. As introduced before, assuming a linear boundary front between the extending zone (yellow colored) and the compressing zone (blue colored), the black dashed line is defined as the slope of the cone shape pattern. The slope of the cone shape can be expressed as,

$$k = \frac{\Delta d}{\Delta t} \tag{5.1}$$

where *d* is the depth of the linear boundary front, and *t* is the time. And Table 5.9 lists the slopes for all four cases.

Table 5.9 Slopes of cone shape pattern with different injection rates

Case	Injection rate, bbl/min	Slope, /
a	10	0.4211
b	15	0.3073
c	20	0.2182
d	25	0.1546

Once we put the injection rates and slopes together, a linear relationship was found out by the curve fitting of the data. The curve fitting result is shown in Fig. 5.10. An empirical equation can be simply expressed as,

$$q = A \times k + B \tag{5.2}$$

where q is injection rate, terms A and B are constants that are to be determined.

In this case, term A equals -55.4, and term B equals 32.7. From numerical exercises, we find that a limitation of this linear empirical equation is when the injection rate cannot be too high or too low. Otherwise, the correlation between the injection rate and the slope will not be linear anymore. For this specific case, the linear correlation stands only when injection rate higher than 10 bbl/min and lower than 25 bbl/min.

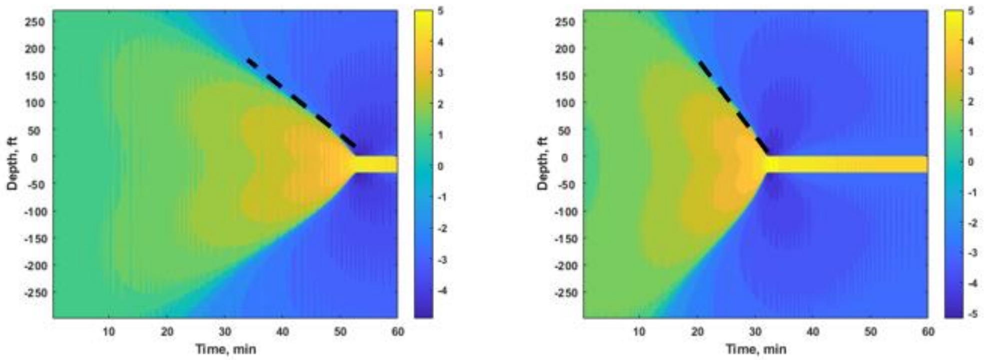

$(a)\ q = 10\ bbl/min$ $(b)\ q = 15\ bbl/min$

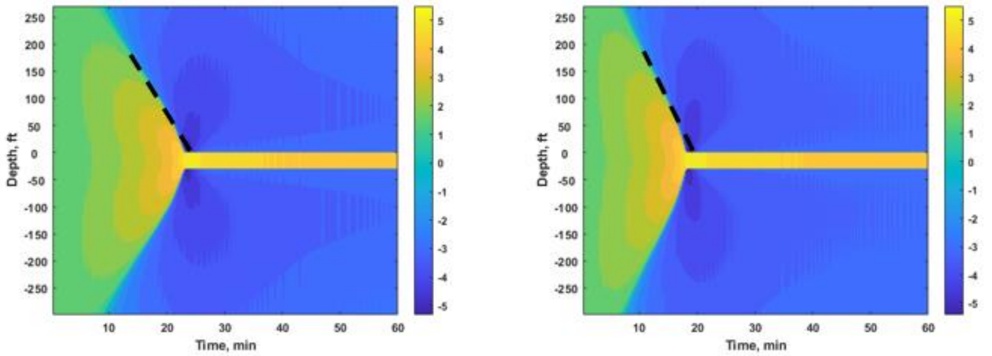

$(c)\ q = 20\ bbl/min$ $(d)\ q = 25\ bbl/min$

Fig. 5.9 Different pattern slopes based on different injection rates

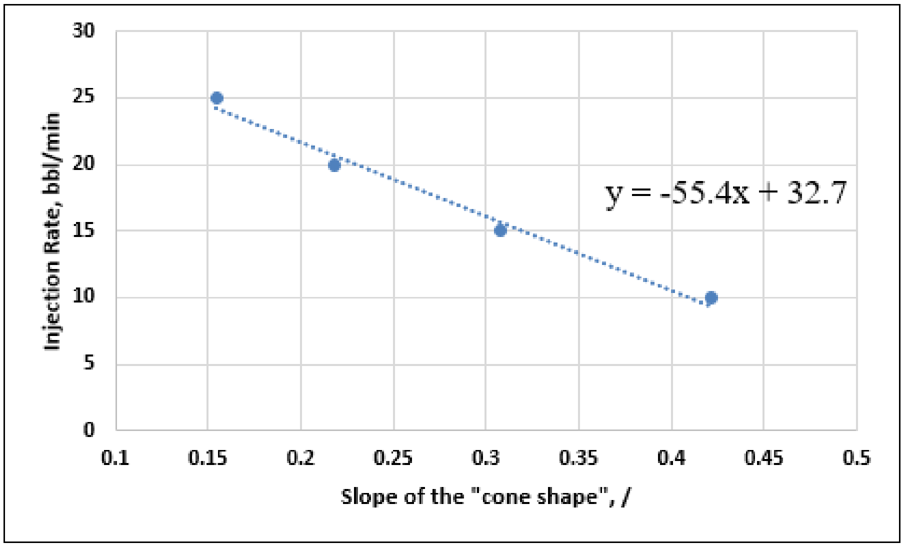

Fig. 5.10 Linear correlation of different pattern slopes and different injection rates

6 PATTERN EXAMINATION FOR MULTIPLE FRACTURES

6.1 Introduction

As we have a basic understanding of the relationship between pattern shape and fracturing parameters, we can discuss the potential applications of the pattern generation of the far-field strain rate simulation for field applications.

The single-fracture study is extended to multiple fractures, and the patterns of strain rate are evaluated for trend recognition.

6.2 Ideal Case Pattern System

To build pattern system, different fracture scenarios are used. A multi-fracture system is used in this study. In the study domain, we use 5 fractures, equally distanced along a horizontal well. Fig. 6.1 shows the placement of the fractures. With all other parameters kept constant, injection rate distribution into each fracture is changed. Four cases, uniformed case, side-biased case (toe or heel), center-dominant case, and “U” shape case, are studied.

Fig. 6.1 shows that the fractures are located at 100, 50, 0, -50, -100 positions along the *y* axial. The multiple fracture propagation model that introduced before is used to simulate multi-fracture development. The input data for simulation models are listed in Table 6.1. The total injection rate per one side is fixed, then the injection rate of each cluster can be calculated by distributing the total injection rate proportionally.

Table 6.1 Input data for ideal case pattern system study

Parameter	Value
Young's modulus, psi	4350000
Poisson's ratio, /	0.22
Total injection rate per one side, bbl/min	45
Fluid viscosity, cp	5
Fracture height, ft	100
Injection time, min	60
Leak-off coefficient, $\mathrm{ft/min}^{0.5}$	0.001
Well spacing, ft	600
Gauge length, m	2

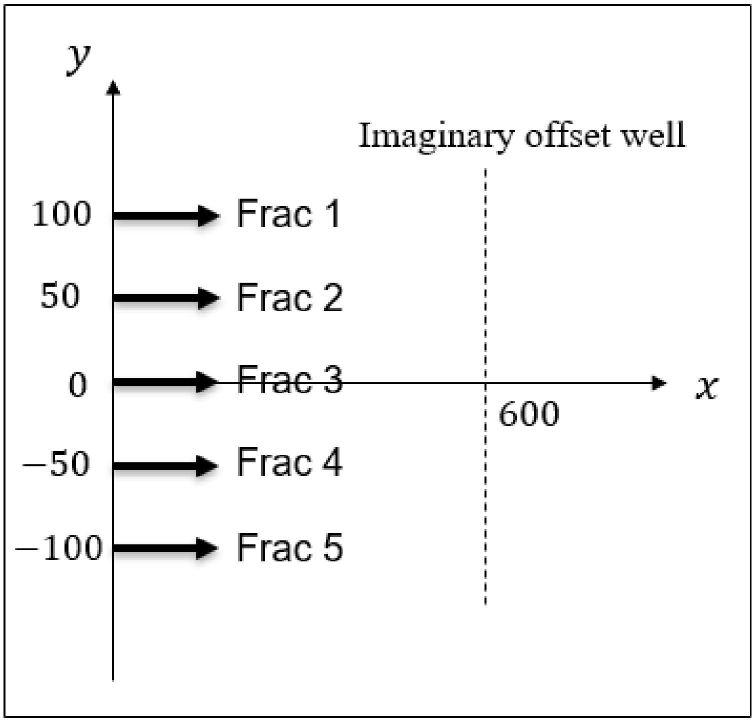

Fig. 6.1 Stimulation domain for ideal case pattern system study

6.2.1 Uniformed Case

The uniformed case is defined as the injection fluid is evenly distributed among the clusters during fracturing. As shown in Fig. 6.2, five clusters took the same 20% of the total injection rate. The far-field strain rate data will be calculated followed the multiple fracture propagation model introduced before.

As the fractures propagating during injection, the strain rate based on fiber-optic measurement at the imaginary well is documented over time. The waterfall plot of strain rate for the uniformed case is shown in Fig. 6.3. From Fig. 6.3, it shows an evenly distributed pattern for strain rate. Each fracture generates a cone shape pattern, all cone shapes have exactly same shape and intensity.

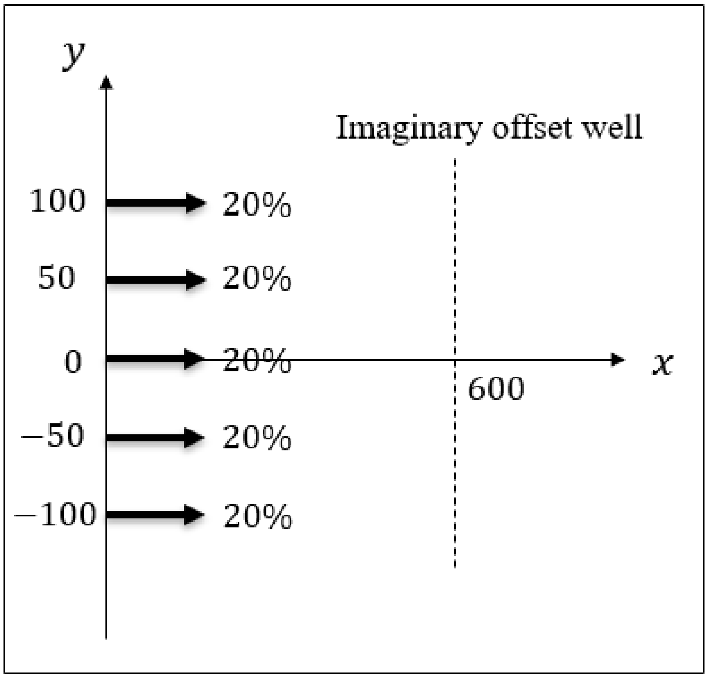

Fig. 6.2 Stimulation domain for the uniformed case

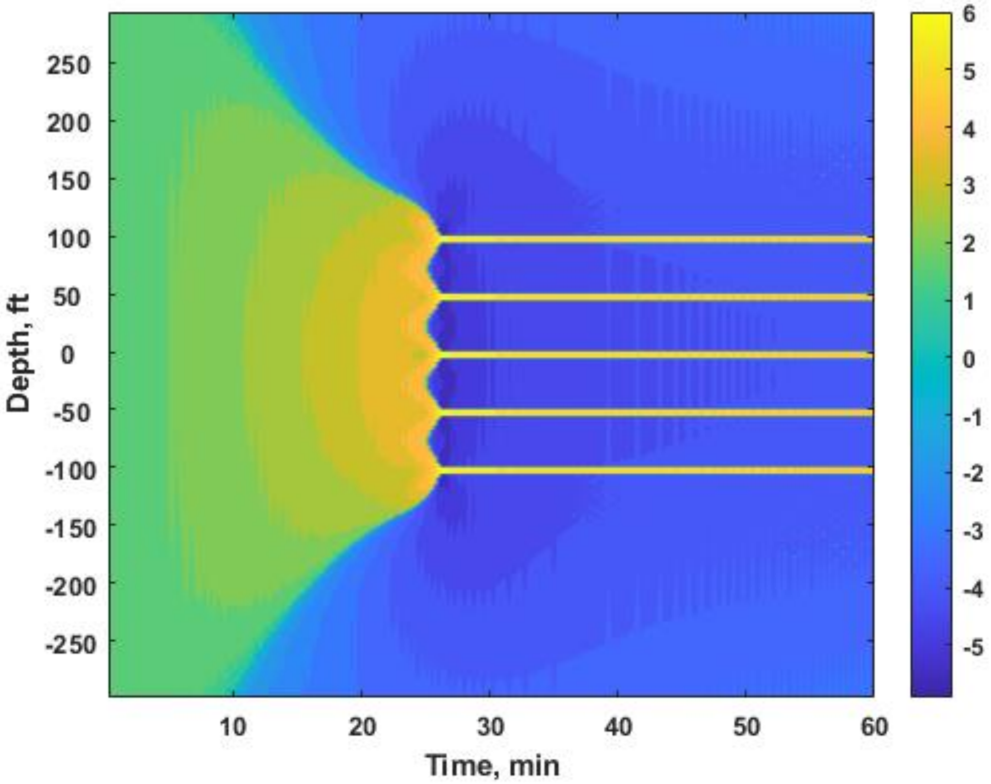

Fig. 6.3 Pattern generation for the uniformed case

6.2.2 Side-Biased Case

The side-biased case is defined as when the injection fluid is higher on one end of the horizontal well and decreasing towards the other end.

This can be either toe-biased or heel-biased. Because toe-biased and heel-biased scenarios are symmetric to each other, therefore, we only illustrate one case here. As shown in Fig. 6.4, the different injection distribution from the total injection rate is marked at each fracture location. The toe side (lower side) fracture takes the dominant of the injection rate.

As the fractures propagating during injection, the fractures are not propagating at the same velocity, because of the injection rate difference. The toe-side fractures propagate faster than the others because the higher inflow enters the fractures. The strain rate, based on fiber-optic measurement along the imaginary well, is recorded during the process. The pattern generation result of the toe-biased case is shown in Fig. 6.5.

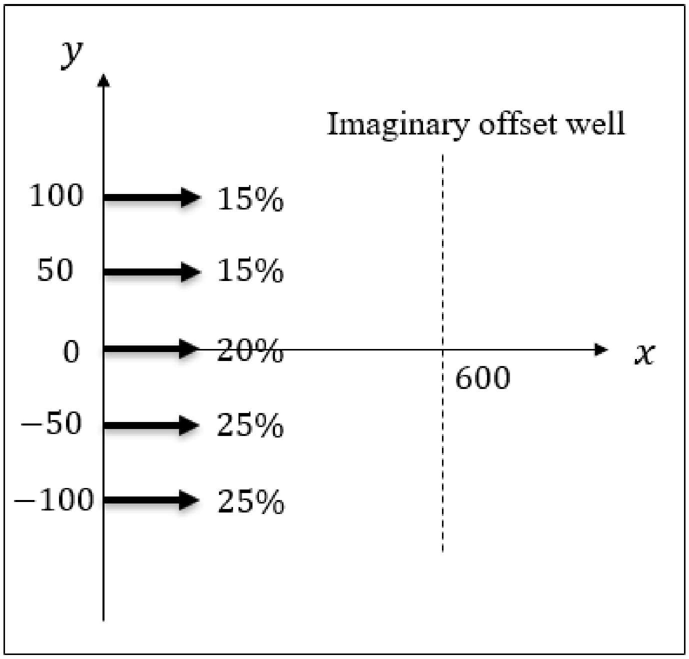

Fig. 6.4 Stimulation domain for the toe-biased case

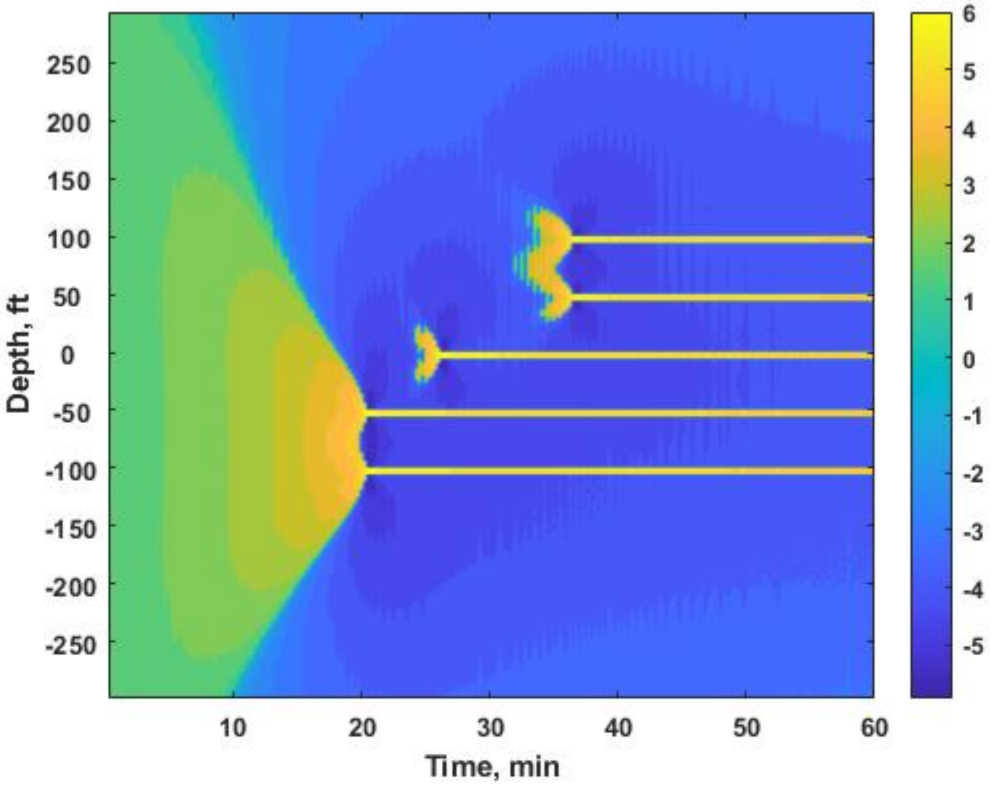

Fig. 6.5 Pattern generation for the toe-biased case

From Fig. 6.5, we can see that the fractures taking more fluid propagate faster (reach the imaginary well quicker), and the middle 20% of injection rate generates smaller area of cone shape pattern than the two sides of 25% and 15% of injection rate.

6.2.3 Center-Dominant Case

The center-dominant case is defined as when the injection fluid is taken the most by the center fracture. As shown in Fig. 6.6, the different injection percentages from the total injection rate are marked at the fracture locations. The center fracture takes double the fluid compared with the end-side fractures.

The waterfall plot of the center-dominated case is shown in Fig. 6.7. Higher injection rate results in faster fracture propagation and large impacted area (center fracture).

In addition, as the distance between the fractures increases and the injection rate decreases, the cone shapes do not connect to each other. The cone-shape pattern for 15% of the injection rate is very close to 20% of the injection rate.

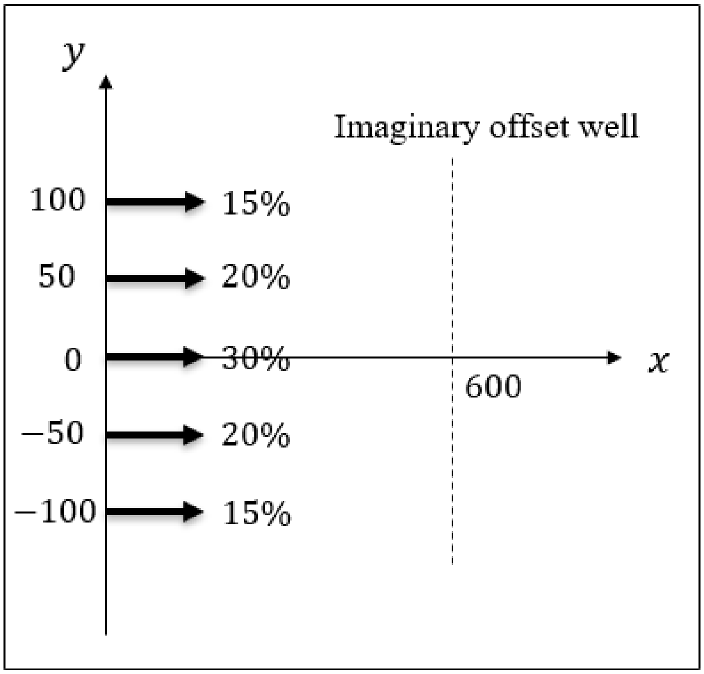

Fig. 6.6 Stimulation domain for the center-dominant case

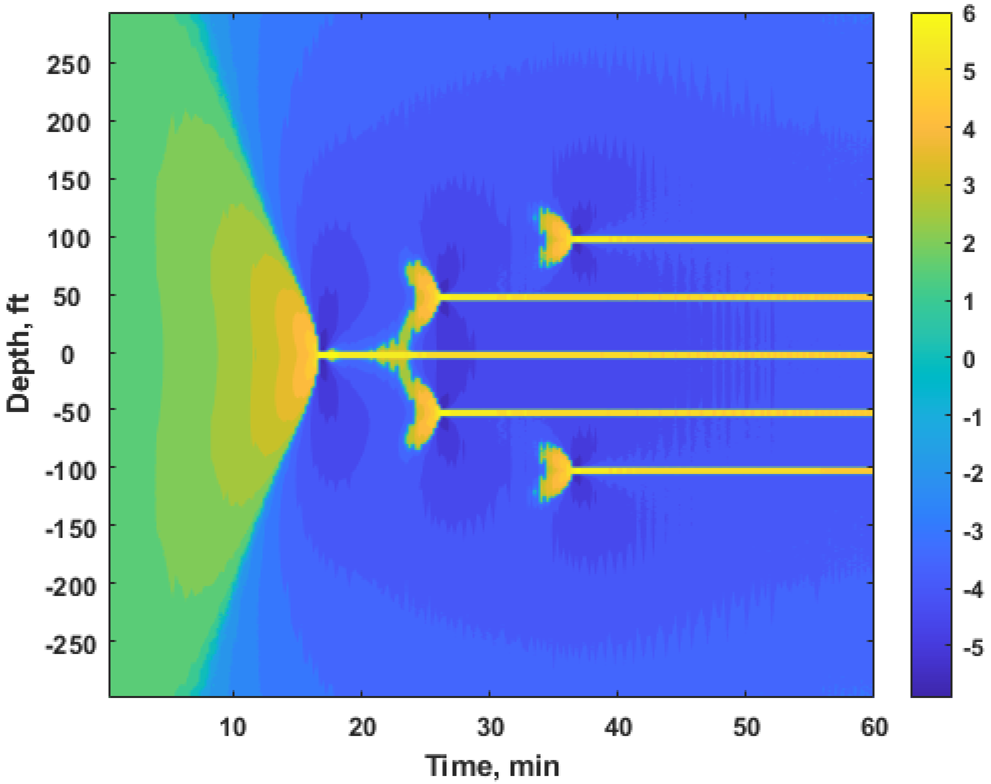

Fig. 6.7 Pattern generation for the center-dominant case

6.2.4 "U" Shape Case

The "U" shape case is defined as when the injection rate is higher at both sides of the horizontal well and decreasing towards the center part. As shown in Fig. 6.8, both sides of the fractures take most of the injection rate, and the percentage of injection rate gradually decreases to the center fracture.

Fig. 6.9 shows the pattern generation of the "U" shape case. The sides of the fractures propagate faster because they take more injection distribution. The center fracture, which takes the least injection fluid, propagates the slowest (last one to reach the offset well). The fractures that take more injection fluid generate a bigger area of the cone shape pattern than those that take less injection fluid.

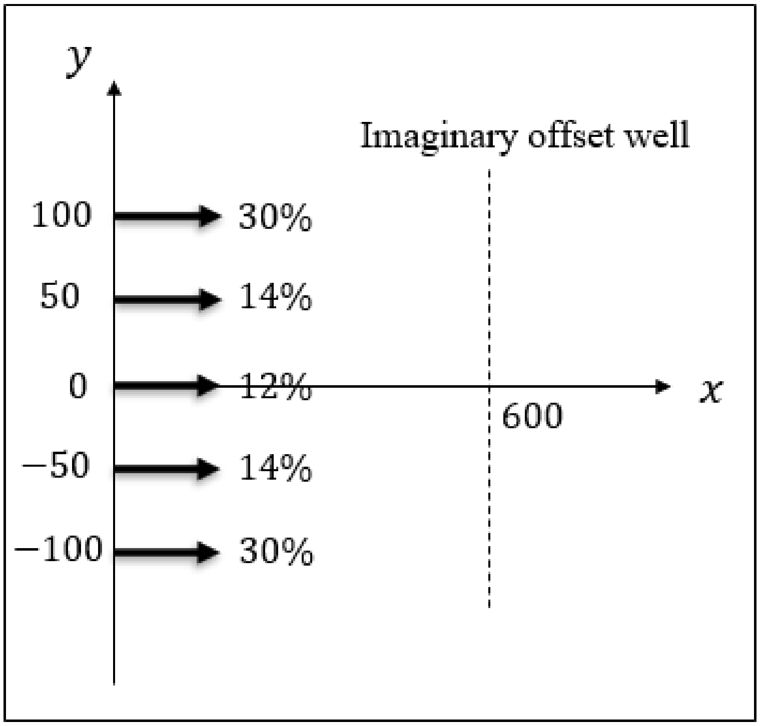

Fig. 6.8 Stimulation domain for the “U” shape case

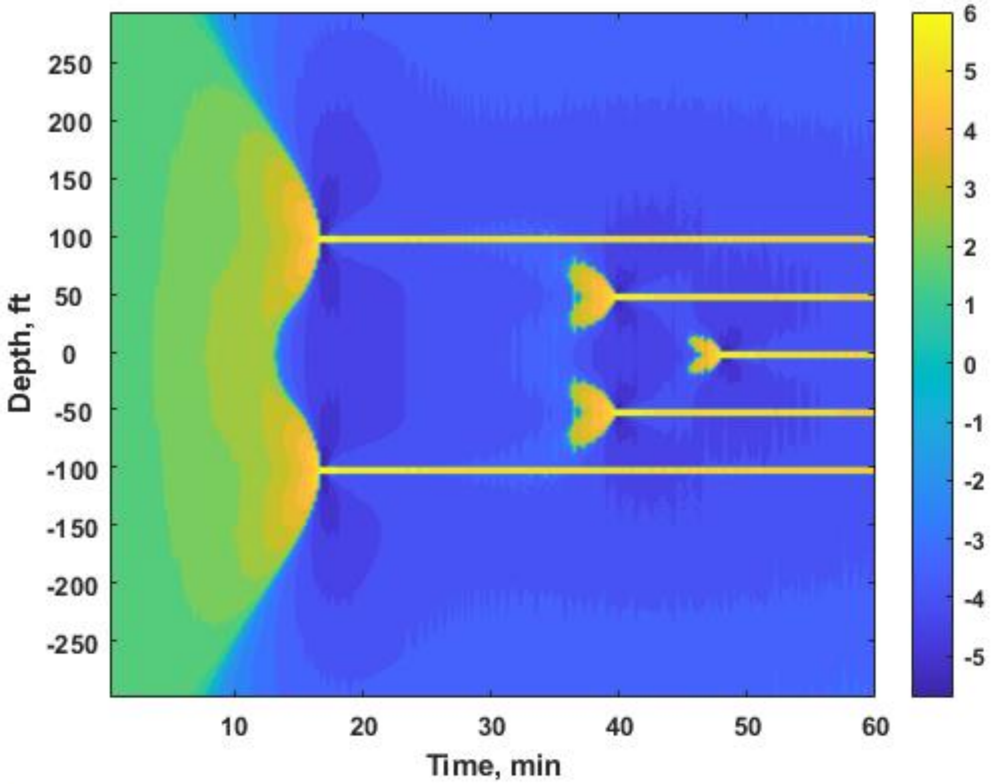

Fig. 6.9 Pattern generation for the "U" shape case

6.3 Completion Efficiency Characterization of the Field Case

After the pattern analysis, we use the observations to diagnose the multi-fracture completion efficiency. The field patterns are usually much more complex than the ideal case patterns (the examples in the previous section). The ideal case pattern is used as a benchmark. We explain the deviations of the field case comparing with the ideal cases.

Knowing that the "strip" width is related to the gauge length of the fiber that has been discussed in Chapter 5, the "strip" width in ideal case pattern can be modified. Many fiber vendors set up a large gauge length for fiber monitoring in the field. Thus, we enlarged the gauge length from 2 m to 8 m to compare with a field case.

In this case, we apply a tighter fracture/cluster spacing, 25 ft, to generate the ideal pattern. The simulation domain is shown in Fig. 6.10. This is a toe-biased completion, and the fluid injection distribution is marked in the picture. The input data for the simulation are listed in Table 6.2.

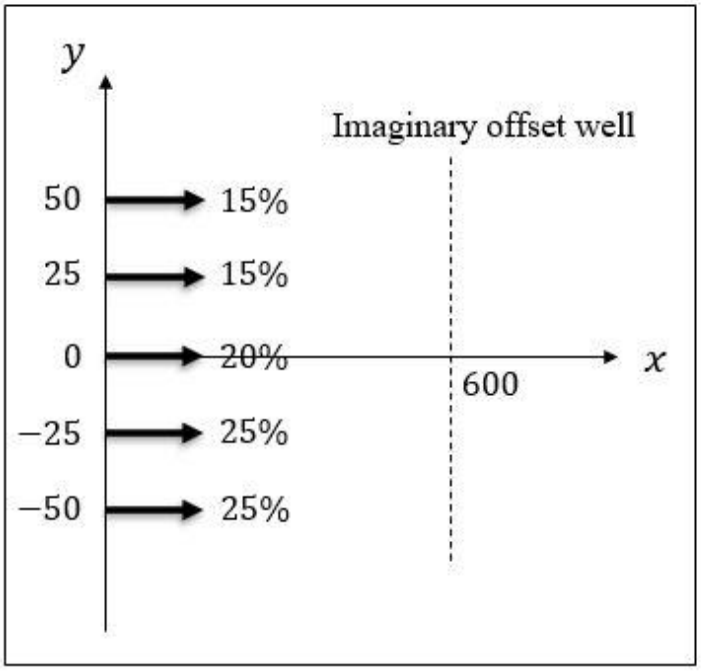

Fig. 6.10 Stimulation domain for the completion efficiency characterization study

Table 6.2 Input data for the completion efficiency characterization study

Parameter	Value
Young's modulus, psi	2900000
Poisson's ratio, /	0.15
Total injection rate per one side, bbl/min	45
Fluid viscosity, cp	10
Fracture height, ft	100
Injection time, min	60
Leak-off coefficient, $\mathrm{ft/min}^{0.5}$	0.001
Well spacing, ft	600

Fig. 6.11 and Fig. 6.12 show the pattern generation for the toe-biased case with different gauge lengths of 2 m and 8 m, respectively. As we can see, enlarging the gauge length makes wider "strips", and eventually "strips" from different fractures get overlapped with each other. In addition, because of the strong compressing zone on the sides of the cross point of "cone shapes" and "strips", once the gauge length has enlarged big enough, the "strips" will be affected that part of the extending on the "strips" will be transformed to compressing.

To quantitatively understand the transformation, a small domain is selected to demonstrate the processed strain rate value. As shown in Fig. 6.12, the targeted domain is marked within the dashed rectangle. The four vertex coordinates of the rectangle are (63,300), (66,300), (63,307), and (66,307). The processed strain rate value in the rectangular domain is shown in Equation 6.1.

$$\hat{\varepsilon} = \begin{bmatrix} 5.0495 & 5.8247 & 5.7093 & 5.5352 \\ 4.9739 & -5.6051 & -5.3181 & -4.9213 \\ 5.4078 & -5.1889 & -4.0969 & 4.8775 \\ 5.3654 & -5.0521 & -4.2075 & 4.8583 \\ 5.3220 & -4.8748 & -4.1996 & 4.8396 \\ 5.2787 & -4.6271 & -4.0762 & 4.8225 \\ 5.2410 & -4.2019 & -3.7469 & 4.8093 \\ 5.2077 & 3.7501 & 3.4649 & 4.7979 \end{bmatrix} \quad (6.1)$$

Fig. 6.13 is a field data set during is a single stage hydraulic fracturing. The patterns are generated from the cross-well DAS data in low-frequency band. Comparing Fig. 6.12 and Fig. 6.13, we can recognize that Fig. 6.13 mainly matches the pattern of Fig. 6.12. We notice that a large range of extending zone shrinks to a “strip” on the toe-side. This means the toe-side fractures propagate faster and first intercept the offset well. Then, the center fractures reach the offset well. In the end, the heel-side fractures reach the offset well. Therefore, Fig. 6.13 can be diagnosed as a toe-biased case.

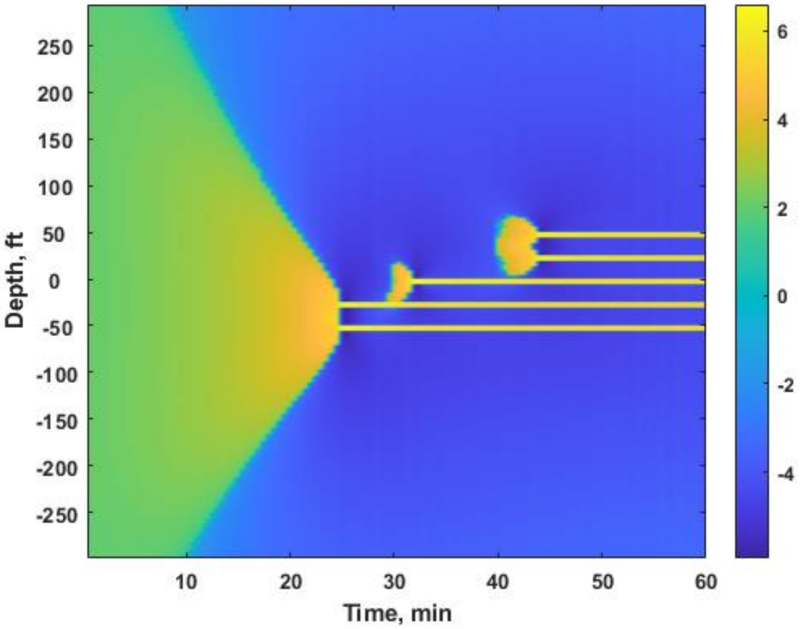

Fig. 6.11 Pattern generation for the toe-biased case with gauge length of 2 m

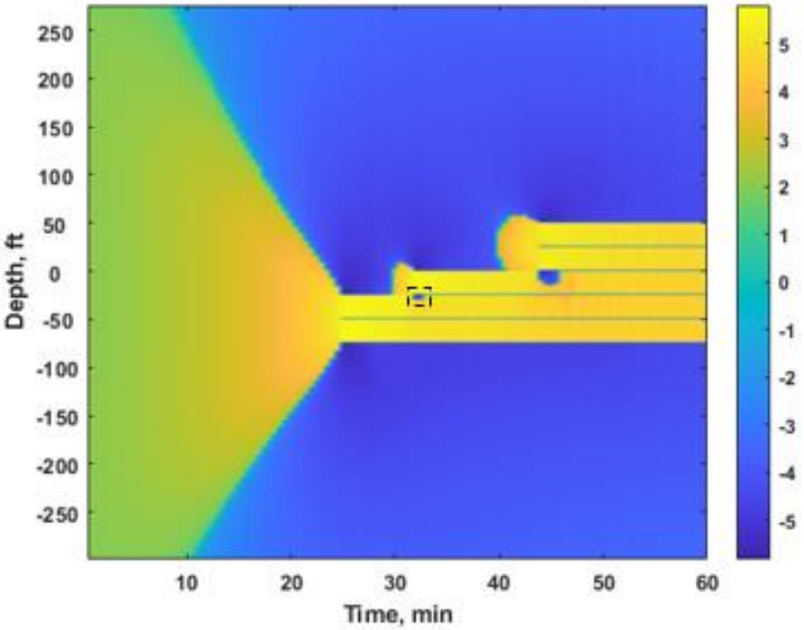

Fig. 6.12 Pattern generation for the toe-biased case with gauge length of 8 m

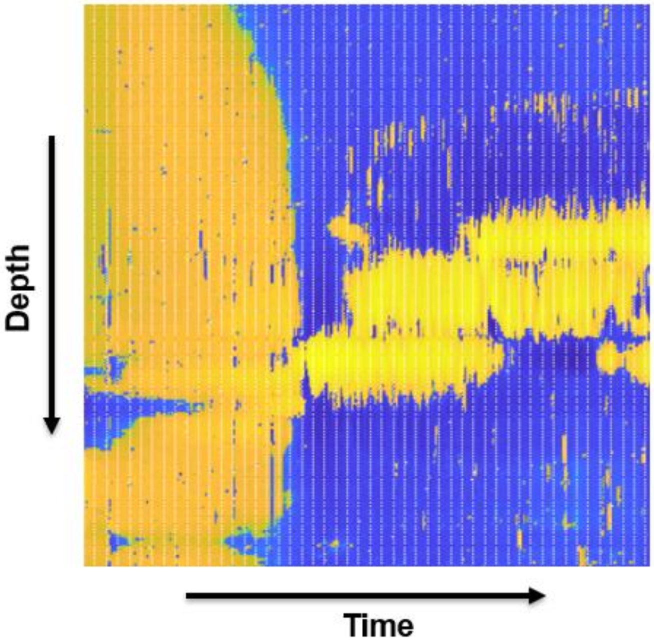

Fig. 6.13 Low-frequency DAS data at an offset well during fracturing

7 CONCLUSION AND FUTURE WORK

7.1 Conclusions of the Completed Work

Throughout this dissertation, pattern generation of far-field strain rate simulation is systematically studied in detail. The primary purpose of this research is to better understand the fracture growth and completion efficiency during multistage hydraulic fracturing from far-field strain rate patterns.

An integrated model has been developed to simulate both strain rate based on rock deformation and strain rate based on fiber-optic measurement during hydraulic fracturing. A workflow of pattern generation, applying special data processing method, has also been built to transform the simulated strain rate data into distinct patterns with polarity. By comparing of the simulation results, we find that the strain rate based on rock deformation differs from the strain rate based on fiber-optic measurement. Strain rate based on fiber-optic measurement can only reflect the trend of strain rate based on rock deformation, however, strain rate based on fiber-optic measurement cannot match of strain rate based on rock deformation numerically. Therefore, the low-frequency DAS measured strain rate can only be interpreted to describe the trend of the rock deformation, not the real value of the rock deformation.

Using the developed model with pattern generation methodology, parametric studies are performed for single fracture synthetic cases to test the sensitivity of each completion parameter to the pattern shape change. The injection rate is found as a sensitive parameter to the pattern shape. By increasing the injection rate, the fracture will propagate faster (reach the offset well quicker). The slope of the core shape pattern will be smaller.

In a certain range of the injection rate, a linear empirical correlation of the pattern slope and the injection rate can be built, which can contribute to the further study of interpreting fracture propagation velocity from low-frequency DAS data.

An ideal case pattern system has been developed to illustrate the ideal patterns of different multi-fracture completion scenarios. By comparing the low-frequency DAS data to the ideal case pattern system, completion efficiency can be detected.

7.2 Future Work

Further studies should be conducted to extend the scope of this dissertation. The future work is listed below:

(1) A more advanced fracture model (Chen et al., 2020) should be used to better describe fracture propagation and inter-fractures.

(2) All the work in this dissertation is completed by applying two-dimensional DDM. The computational efficiency is significantly higher than three-dimensional DDM. However, the accuracy comparison of two-dimensional DDM against three-dimensional DDM is not discussed in this dissertation. Future work is needed to compare the difference between the two-dimensional and three-dimensional DDM calculation results.

REFERENCES

Abou-Sayed, A. S., Sinha, K. P., & Clifton, R. J. (1984, January 1). Evaluation of the Influence of In-Situ Reservoir Conditions on the Geometry of Hydraulic Fractures Using a 3-D Simulator: Part 1-Technical Approach. Society of Petroleum Engineers. doi:10.2118/12877-MS.

Al Jawad, Murtada Saleh H (2018). Development of a Fully Integrated Acid Fracture Model. Doctoral dissertation, Texas A & M University. Available electronically from https : / /hdl .handle .net /1969 .1 /173663.

Bukhamsin, A. and Horne, R. 2014. Using Distributed Acoustic Sensors to Optimize Production in Intelligent Wells. Presented at the SPE Annual Techni- cal Conference and Exhibition, Amsterdam, 27–29 October. SPE-170679-MS. https://doi.org/10.2118/170679-MS.

Carter, R. D. 1957. Appendix to Optimum fluid characteristics for fracture extension. By G.C. Howard and C.R. Fast. Drill. And Prod. Prac, API 267.

Chen, M., Zhang, S., Li, S., Ma, X., Zhang, X., Zou, Y. 2020. An explicit algorithm for modeling planar 3D hydraulic fracture growth based on a super-time-stepping method. International Journal of Solids and Structures Volumes 191–192, 15 May 2020, Pages 370-389.

Cheung, P.S-Y., and Heliot, D.: "Workstation-Based Fracture Evaluation Using Borehole Images and Wireline Logs." Paper presented at the SPE Annual Technical Conference and Exhibition, New Orleans, Louisiana, September 1990. doi: https://doi.org/10.2118/20573-MS.

Cipolla, C. L., Lolon, E., Mayerhofer, M. J., & Warpinski, N. R. (2009, January 1). Fracture Design Considerations in Horizontal Wells Drilled in Unconventional Gas Reservoirs. Society of Petroleum Engineers. doi:10.2118/119366-MS.

Cipolla, C. L., & Wright, C. A. (2000, January 1). State-of-the-Art in Hydraulic Fracture Diagnostics. Society of Petroleum Engineers. doi:10.2118/64434-MS.

Clifton, R. J., & Abou-Sayed, A. S. (1981, January 1). A Variational Approach To The Prediction Of The Three-Dimensional Geometry Of Hydraulic Fractures. Society of Petroleum Engineers. doi:10.2118/9879-MS.

Cramer, D., Friehauf, K., Roberts, G., & Whittaker, J. (2019, January 29). Integrating DAS, Treatment Pressure Analysis and Video-Based Perforation Imaging to

Evaluate Limited Entry Treatment Effectiveness. Society of Petroleum Engineers. doi:10.2118/194334-MS.

Crouch, S. L. 1976. Solution of Plane Elasticity Problems by the Displacement Discontinuity Method. International Journal for Numerical Methods in Engineering 10(2): 301-343.

Crouch, S. L. and Starfield, A. M. 1983. Boundary element methods in solid mechanics. London: George Allen & Unwin.

Daneshy, A. A. (2011, January 1). Hydraulic Fracturing of Horizontal Wells: Issues and Insights. Society of Petroleum Engineers. doi:10.2118/140134-MS.

Dontsov, E.V., Peirce, A.P., 2015. An enhanced pseudo-3D model for hydraulic fracturing accounting for viscous height growth, non-local elasticity, and lat- eral toughness. Eng. Fract. Mech. 142, 116–139. http://dx.doi.org/10.1016/j. engfracmech.2015.05.043.

Dou, S., Lindsey, N., Wagner, A.M. et al. Distributed Acoustic Sensing for Seismic Monitoring of The Near Surface: A Traffic-Noise Interferometry Case Study. Sci Rep 7, 11620 (2017). https://doi.org/10.1038/s41598-017-11986-4.

EIA. https://www.eia.gov/maps/images/shale_gas_lower48.pdf. Accessed January 2021.

ESG Solutions. https://www.esgsolutions.com/oil-and-gas/long-term-reservoir-monitoring. Accessed January 2021.

Fisher, M.K., Heinze, J.R., Harris, C.D., McDavidson, B.M., Wright, C.A., Dunn, K.P.: “Optimizing Horizontal Completion Techniques in the Barnett Shale Using Microseismic Fracture Mapping,” Paper SPE 90051, presented at the 2004 SPE Annual Technical Conference and Exhibition, Houston, TX, 26-29 September.

Frings, J., and Walk, T., 2010. Pipeline Leak Detection Using Distributed Fiber Optic Sensing. Pipeline Inspection and Control, pp. 57-61.

Fung, R. L., Vilayakumar, S., & Cormack, D. E. (1987, December 1). Calculation of Vertical Fracture Containment in Layered Formations. Society of Petroleum Engineers. doi:10.2118/14707-PA.

Geertsma, J., & De Klerk, F. (1969, December 1). A Rapid Method of Predicting Width and Extent of Hydraulically Induced Fractures. Society of Petroleum Engineers. doi:10.2118/2458-PA.

Hill, A.D. 1990. Production Logging: Theoretical and Interpretive Elements. Richardson, TX USA: Society of Petroleum Engineers. Original edition. ISBN 1555630308.

Howard, G. C., & Fast, C. R. (1957, January 1). Optimum Fluid Characteristics for Fracture Extension. American Petroleum Institute.

Jin, G., and Roy, B., 2017, Hydraulic-fracture geometry characterization using low-frequency DAS signal: The LeadingEdge, 36, 975–980, https://doi.org/10.1190/tle36120975.1.

Johannessen, K., Drakeley, B., and Farhadiroushan, M.: "Distributed Acoustic Sensing - A New Way of Listening to Your Well/Reservoir." Paper presented at the SPE Intelligent Energy International, Utrecht, The Netherlands, March 2012. doi: https://doi.org/10.2118/149602-MS.

Khristianovitch, S.A. and Zheltov, Y.P. 1955. Formation of Vertical Fractures by Means of Highly Viscous Fluids. Proc., 4th World Petroleum Congress, Rome, 2:579-586.

Krohn, D. A., MacDougall, T. W., Mendez, A. 2015. Fiber Optic Sensors: Fundamentals and Applications, Fourth Edition. https://doi.org/10.1117/3.1002910.

Li, X., Zhang, J., Grubert, M., Laing, C., Chavarria, A., Cole, S., & Oukaci, Y. (2020, January 28). Distributed Acoustic and Temperature Sensing Applications for Hydraulic Fracture Diagnostics. Society of Petroleum Engineers. doi:10.2118/199759-MS.

Marongiu-Porcu, M., Lee, D., Shan, D., & Morales, A. (2015, September 28). Advanced Modeling of Interwell Fracturing Interference: an Eagle Ford Shale Oil Study. Society of Petroleum Engineers. doi:10.2118/174902-MS.

Nordgren, R. P. (1972, August 1). Propagation of a Vertical Hydraulic Fracture. Society of Petroleum Engineers. doi:10.2118/3009-PA.

Olson, J. E. 2004. Predicting fracture swarms- the influence of subcritical crack growth and the crack-tip process zone on joint spacing in rock. Geological society, London, Special Publications 231(1): 73-88.

Pakhotina, I., Sakaida, S., Zhu, D., & Hill, A. D.: "Diagnosing Multistage Fracture Treatments with Distributed Fiber-Optic Sensors." Paper presented at the SPE Hydraulic Fracturing Technology Conference and Exhibition, The Woodlands, Texas, USA, February 2020. doi: https://doi.org/10.2118/199723-MS.

Pakhotina, J., Zhu, D., & Hill, A. D. (2020b, October 21). Evaluating Perforation Erosion and its Effect on Limited Entry by Distributed Acoustic Sensor DAS Monitoring. Society of Petroleum Engineers. doi:10.2118/201538-MS.

Perkins, T. K., & Kern, L. R. (1961, September 1). Widths of Hydraulic Fractures. Society of Petroleum Engineers. doi:10.2118/89-PA.

Roberts, G., Whittaker, J. L., & McDonald, J. (2018, October 16). A Novel Hydraulic Fracture Evaluation Method Using Downhole Video Images to Analyse Perforation Erosion. Society of Petroleum Engineers. doi:10.2118/191466-18IHFT-MS.

Safari, R., Lewis, R., Ma, X., Mutlu, U., & Ghassemi, A. (2017, April 1). Infill-Well Fracturing Optimization in Tightly Spaced Horizontal Wells. Society of Petroleum Engineers. doi:10.2118/178513-PA.

Santos, Rodolfo Alfonso (2018). Experimental Study of the Effect of Permeability on the Generation of Noise. Master's thesis, Texas A & M University. Available electronically from http : / /hdl .handle .net /1969 .1 /174369.

Settari, A., & Cleary, M. P. (1984, July 1). Three-Dimensional Simulation of Hydraulic Fracturing. Society of Petroleum Engineers. doi:10.2118/10504-PA.

Simonson, E. R., Abou-Sayed, A. S., & Clifton, R. J. (1978, February 1). Containment of Massive Hydraulic Fractures. Society of Petroleum Engineers. doi:10.2118/6089-PA.

Sneddon, I. N., Elliott, H. A. 1946. The opening of a Griffith crack under internal pressure. Quart. Appl. Math. IV, No.3, 262-267.

Sneddon, I. N.: "The Distribution of Stress in the Neighbourhood of a Crack irt an Elastic Solid," Proc., Royal Society of London, Series A (1946) 187, 229-60.

Sneddon, I. N. 1951. Fourier transforms. New York: McGraw-Hill.

Ugueto C., G. A., Huckabee, P. T., Molenaar, M. M., Wyker, B., & Somanchi, K.: "Perforation Cluster Efficiency of Cemented Plug and Perf Limited Entry Completions; Insights from Fiber Optics Diagnostics." Paper presented at the SPE Hydraulic Fracturing Technology Conference, The Woodlands, Texas, USA, February 2016. doi: https://doi.org/10.2118/179124-MS.

Ugueto, G. A., Todea, F., Daredia, T., Wojtaszek, M., Huckabee, P. T., Reynolds, A., … Chavarria, J. A. (2019, September 23). Can You Feel the Strain? DAS Strain

Fronts for Fracture Geometry in the BC Montney, Groundbirch. Society of Petroleum Engineers. doi:10.2118/195943-MS.

Valko, P., Economides, M. J. 1995. Hydraulic fracture mechanics. John Wiley & Sons Ltd, Baffins Lane, Chichester, West Sussex PO19 IUD, England.

Warpinski, N.R., Branagan, P.T., Engler, B.P., Wilmer, R., Wolhart, S.L., Evaluation of a downhole tiltmeter array for monitoring hydraulic fractures, International Journal of Rock Mechanics and Mining Sciences, Volume 34, Issues 3–4, 1997, Pages 329.e1-329.

Weng, X., 1992. Incorporation of 2D fluid flow into a pseudo-3D hydraulic fracturing simulator. SPE Prod. Eng. (4) 331–337. doi: 10.2118/21849-PA.

Wolhart, S. L., McIntosh, G. E., Zoll, M. B., & Weijers, L. (2007, January 1). Surface Tiltmeter Mapping Shows Hydraulic Fracture Reorientation in the Codell Formation, Wattenberg Field, Colorado. Society of Petroleum Engineers. doi:10.2118/110034-MS.

Woodroof, R.A., Asadi, M., Leonard, R.S., Rainbolt, M.: “Monitoring Fracturing Fluid Flowback and Optimizing Fracturing Fluids Cleanup in the Bossier Sand Using Chemical Frac Tracers,” Paper SPE 84486, presented at 2003 SPE Annual Technical Conference and Exhibition, Denver, CO, USA, 5-8 October 2003.

Wright, C. A., Davis, E. J., Minner, W. A., Ward, J. F., Weijers, L., Schell, E. J., & Hunter, S. P. (1998, January 1). Surface Tiltmeter Fracture Mapping Reaches New Depths - 10,000 Feet and Beyond? Society of Petroleum Engineers. doi:10.2118/39919-MS.

Wright, C. A., Davis, E. J., Wang, G., & Weijers, L. (1999, January 1). Downhole tiltmeter fracture mapping: A new tool for direct measurement of hydraulic fracture growth. American Rock Mechanics Association.

Wu, K. 2014. Numerical Modeling of Complex Hydraulic Fracture Development in Unconventional Reservoirs. Ph.D. Dissertation. The University of Texas at Austin.

Zhang, Shuang (2019). Interpretation of Downhole Temperature Measurements for Multistage Fracture Stimulation in Horizontal Wells. Doctoral dissertation, Texas A&M University. Available electronically from http : / /hdl .handle .net /1969 .1 /186165.